

**SYNTHESIS AND CHARACTERIZATION OF  
CRYSTALLINE MONODISPERSED  
 $\gamma$ -Fe<sub>2</sub>O<sub>3</sub> NANOPARTICLES**

**Kimberly Edwards**

**A thesis presented to the faculty of Mount Holyoke College in partial  
fulfillment of the requirements for the degree of  
Bachelor of Arts with Honors**

**Department of Chemistry  
Mount Holyoke College  
South Hadley, Massachusetts**

**December 2013**

This thesis was prepared under the direction of Dr. Himali Jayathilake

## ACKNOWLEDGEMENTS

The researcher wishes to acknowledge the invaluable contribution of various persons in respect to this project.

I wish to thank Dr. Himali Jayathilake, my thesis advisor, to whom I owe my growth as a scientist, thus far. You have been a tremendous advisor who, through continuous guidance, propelled me towards this significant achievement. Deepest appreciation to you for your patience in helping me from the beginning to the end of my project. Thank you for believing in me.

In addition to Dr. Jayathilake, I am grateful to the other members of my Thesis Defense Committee: to Professor Wei Chen, for her extended guidance, advice and encouragement from my first year at Mount Holyoke. Your input was essential to my thesis. Likewise, Professor Alexi Arango for his encouragement and insight.

To the current and former members of the Jayathilake Research Group, Liz, Zahra and Barsha, and the Chen Research Group, thank you for your comments, questions and great suggestions while I was working on this project. Also to Gillian, a friend and classmate, thank you for sharing your valuable Inorganic Chemistry knowledge with me.

I dedicate this thesis to my mother, father (now deceased), brother and extended family here in the United States. Thank you for your unconditional love and support. Thank for always convincing me to try harder. Without you I would not have reached where I am today, embracing my dreams and aspirations.

**TABLE OF CONTENTS**

|  | Page Numbers |
|--|--------------|
| ACKNOWLEDGEMENTS   | i            |
| LIST OF FIGURES AND TABLES   | v            |
| ABSTRACT   | 1            |
| CHAPTER 1. INTRODUCTION  |              |
| 1.1 Nanotechnology   | 2            |
| 1.2 Data Storage   | 5            |
| 1.3 Synthesis of Magnetic Nanoparticles  | 8            |
| 1.4 Nucleation and Growth Steps of $\gamma$ -Fe <sub>2</sub> O <sub>3</sub> Nanoparticles<br>During Thermal Decomposition      | 10           |
| 1.5 Influential Parameters for Synthesis of $\gamma$ -Fe <sub>2</sub> O <sub>3</sub><br>Nanoparticles By Thermal Decomposition | 13           |
| 1.6 Protection and Stabilization of Fe Nanoparticles   | 16           |
| 1.7 The Goal   | 17           |
| CHAPTER 2. INSTRUMENTAL METHODS  |              |
| 2.1 Spin Casting   | 20           |
| 2.2 Atomic Force Microscopy (AFM)  | 23           |
| 2.3 Scanning Electron Microscopy (SEM)   | 29           |
| 2.4 Ultra-violet Visible Spectrophotometry (UV-Vis)  | 33           |
| 2.5 Fourier Transform Infrared Spectroscopy (FT-IR)  | 35           |
| CHAPTER 3. EXPERIMENTAL  |              |
| 3.1 Synthesis of Monodisperse and Crystalline $\gamma$ -Fe <sub>2</sub> O <sub>3</sub>   |              |

|   |    |
|---|----|
| Nanocrystallites  | 39 |
| 3.2 Washing of Monodisperse and Crystalline $\gamma$ -Fe <sub>2</sub> O <sub>3</sub>            |    |
| Nanocrystallites  | 41 |
| 3.3 Solvent Selection   | 42 |
| 3.4 Agitation Method (Vortex Mixing vs. Sonication)   | 42 |
| 3.5 Silicon Wafer Cleaning  | 43 |
| 3.6 Spin Casting Settings   | 44 |
| 3.7 Broadly Varying the Concentration of $\gamma$ -Fe <sub>2</sub> O <sub>3</sub>               |    |
| Nanoparticles Redispersed in Octane   | 45 |
| 3.8 Slightly Varying the Concentration of $\gamma$ -Fe <sub>2</sub> O <sub>3</sub>              |    |
| Nanoparticles Redispersed in Octane   | 46 |
| 3.9 Characterization with AFM   | 47 |
| 3.10 Characterization with UV-Vis   | 48 |
| 3.11 Characterization with FT-IR  | 48 |
| 3.12 Characterization with SEM  | 49 |
| <br>  |    |
| CHAPTER 4. RESULTS AND DISCUSSION   |    |
| 4.1 Identification of the $\gamma$ -Fe <sub>2</sub> O <sub>3</sub> Nanocrystallites Synthesized | 50 |
| 4.1.1. AFM Analysis   | 50 |
| 4.1.2. UV-Vis Analysis  | 54 |
| 4.1.3. FT-IR Analysis   | 55 |
| 4.2 Investigating the effect of Agitation Methods on $\gamma$ -Fe <sub>2</sub> O <sub>3</sub>   |    |
| Nanoparticle Self-Assembly  | 56 |
| 4.2.1 Sonication  | 58 |
| 4.2.1.1 Hexane  | 58 |
| 4.2.1.2. Octane   | 60 |
| 4.2.1.3. Toluene  | 63 |

|  |     |
|--|-----|
| 4.2.1.4. Compilation of Sonication Results:  |     |
| Hexane, Octane and Toluene   | 65  |
| 4.2.2 Vortex Mixing  | 67  |
| 4.2.2.1 Hexane   | 67  |
| 4.2.2.2. Octane  | 69  |
| 4.2.2.3. Toluene   | 71  |
| 4.2.2.4. Compilation of Vortex Mixing Results:   |     |
| Hexane, Octane and Toluene   | 74  |
| 4.3 Results from Ultrasonically Cleaning the Silicon Wafers  | 76  |
| 4.4 Results from the Experimentation with Spin Casting Settings<br>in Different Solvents   | 77  |
| 4.4.1. Octane  | 77  |
| 4.4.2 Toluene  | 78  |
| 4.5 Results from Broadly Varying the Concentration of $\gamma$ -Fe <sub>2</sub> O <sub>3</sub><br>Nanoparticles Redispersed in Octane  | 80  |
| 4.6 Results from Slightly Varying the Concentration of $\gamma$ -Fe <sub>2</sub> O <sub>3</sub><br>Nanoparticles Redispersed in Octane | 87  |
| 4.7 SEM Analysis   | 92  |
| <br>   |     |
| CHAPTER 5. CONCLUSIONS AND FUTURE WORK   | 98  |
| <br>   |     |
| REFERENCES CITED   | 100 |

## LIST OF FIGURES, TABLES AND SCHEMES

|  | <b>Page Number</b> |
|--|--------------------|
| <b>Figure 1:</b> The magnetic domains of iron with respect to size of material.  | 4                  |
| <b>Figure 2:</b> A Magnetic Force Microscope image of a 394 Gigabyte/inche <sup>2</sup> disk.  | 6                  |
| <b>Figure 3:</b> The hypothesized means of storing data on individual magnetic iron nanoparticles.   | 7                  |
| <b>Figure 4:</b> (a) TEM images of samples extracted from solution during synthesis (b) Proposed schematic diagram of nucleation and growth process. Samples were extracted at the intervals indicated above.  | 11                 |
| <b>Figure 5:</b> Increasing the rates of temperature increase for the decomposition, (a) 5°C/min, (b) 15°C/min, (c) 25°C/min and (d) 35°C/min.   | 14                 |
| <b>Figure 6:</b> Synthesis of Fe <sub>3</sub> O <sub>4</sub> nanocrystals. The second and third panels are TEM images of the as-synthesized nanocrystals taken at different reaction times.  | 15                 |
| <b>Figure 7:</b> The decomposition temperature (°C) of iron pentacarbonyl and the nanoparticle size (nm) with different capping molecules.   | 15                 |
| <b>Figure 8:</b> The molecular structures of surfactants that can be used in this research project; a) Butanoic Acid; b) Octanoic Acid (Caprylic Acid); c) Lauric Acid (Dodecanoic Acid); d) Oleic Acid ((9Z)-Octadec-9-enoic Acid); e) Erucic Acid ((Z)-Docos-13-enoic acid). | 17                 |
| <b>Figure 9:</b> The self-assembly of two $\gamma$ -Fe <sub>2</sub> O <sub>3</sub> nanoparticles.  | 18                 |
| <b>Figure 10:</b> Centrifugal force acting outwards on a spherical body kept in a circular motion by a string.   | 21                 |
| <b>Figure 11:</b> Example of a size distribution chart for a sample set of nanoparticles in the center of a silicon wafer that contains sample.  | 22                 |

|  |    |
|--|----|
| <b>Figure 12:</b> Atomic force microscopy functional probe. A tip protruding from a standard Commercial Cantilever that is mounted onto a Si based chip, also called a holder plate.   | 24 |
| <b>Figure 13:</b> Cantilever deflection as it approaches the surface of the sample.  | 25 |
| <b>Figure 14:</b> Atomic force microscopy functional probe. There are usually two different scanning modes used in AFM, a) contact mode and b) non-contact mode. Aiming a laser beam at the back of the cantilever, and mapping the position of the reflected beam with a position-sensitive deflector, measures the cantilever's deflection while it scans the surface. | 28 |
| <b>Figure 15:</b> A schematic of a typical Scanning Electron Microscope (SEM).   | 31 |
| <b>Figure 16:</b> A schematic diagram of the UV-Vis spectrophotometer.   | 34 |
| <b>Figure 17:</b> Schematic diagram of a FT-IR configured, Michelson interferometer.   | 37 |
| <b>Figure 18:</b> Apparatus for $\gamma$ -Fe <sub>2</sub> O <sub>3</sub> Nanocrystallites synthesis using the Thermal Decomposition method. Nitrogen gas was used to create an inert atmosphere only in Part (b) of the synthesis. The temperature of the oil bath was used as an approximate indicator of the reaction temperature.                                     | 39 |
| <b>Figure 19:</b> Molecular structures of $\gamma$ -Fe <sub>2</sub> O <sub>3</sub> Nanocrystallite precursors: a) Octanoic Acid (Caprylic Acid), b) Dioctyl ether, c) Iron Pentacarbonyl, d) Trimethylamine N-oxide.   | 40 |
| <b>Figure 20:</b> Side view and annotated diagram of the set up for ultrasonically cleaning the silicon wafers.  | 44 |
| <b>Figure 21:</b> Method used to prepare samples closer in concentration.  | 46 |
| <b>Figure 22:</b> AFM images of $\gamma$ -Fe <sub>2</sub> O <sub>3</sub> nanoparticles on silicon wafers, (a) dispersed in octane (b), (c) dispersed in hexane. Graphs d), e) and f) are the corresponding histograms, each having a sample set of 50 nanoparticles. Samples were vortex mixed for   | 51 |

the time indicated.

- Figure 23:** Effect of solvent and vortex mixing on the average size and monodispersity of nanoparticles. The average sizes and standard deviations were calculated using Microsoft Excel from a sample set of 50 nanoparticles for each sample shown in Figure 22. 53
- Figure 24:** UV-Vis spectrum of  $\gamma$ -Fe<sub>2</sub>O<sub>3</sub> nanoparticles redispersed in Octane. 54
- Figure 25:** FT-IR spectrum of dried  $\gamma$ -Fe<sub>2</sub>O<sub>3</sub> nanoparticles at room temperature. 55
- Figure 26:** AFM images of samples containing  $\gamma$ -Fe<sub>2</sub>O<sub>3</sub> nanoparticles redispersed in hexane and their corresponding AFM Video Camera snap shots of the sample surface. Samples were sonicated. 58
- Figure 27:** Effect of  $\gamma$ -Fe<sub>2</sub>O<sub>3</sub> nanoparticle size distribution as a function of sonication time. Hexane is used as the solvent to disperse nanoparticles. 60
- Figure 28:** AFM images of samples containing  $\gamma$ -Fe<sub>2</sub>O<sub>3</sub> nanoparticles redispersed in octane and their corresponding AFM Video Camera snap shots of the sample surface. Samples were sonicated. 61
- Figure 29:** Effect of  $\gamma$ -Fe<sub>2</sub>O<sub>3</sub> nanoparticle size distribution as a function of sonication time. Octane is used as the solvent to disperse nanoparticles. 62
- Figure 30:** AFM images of samples containing  $\gamma$ -Fe<sub>2</sub>O<sub>3</sub> nanoparticles redispersed in toluene and their corresponding AFM Video Camera snap shots of the sample surface. Samples were sonicated. 63
- Figure 31:** Effect of  $\gamma$ -Fe<sub>2</sub>O<sub>3</sub> nanoparticle size distribution as a function of sonication time. Toluene is used as the solvent to disperse nanoparticles. 64
- Figure 32:** Representation of characteristic features of samples drop casted for hexane, octane and toluene. 65

- Figure 33:** A compiled chart showing the effects of all three redispersing solvents and sonication on the average sizes of nanoparticles. 66
- Figure 34:** AFM images of samples containing  $\gamma$ -Fe<sub>2</sub>O<sub>3</sub> nanoparticles redispersed in hexane and vortex mixed, along with their corresponding AFM Video Camera snap shots of the sample surface. The AFM cantilever was present in snap shots. 68
- Figure 35:** Effect of  $\gamma$ -Fe<sub>2</sub>O<sub>3</sub> nanoparticle size distribution as a function of vortex mixing time. Hexane is used as the solvent to disperse nanoparticles. 69
- Figure 36:** AFM images of samples containing  $\gamma$ -Fe<sub>2</sub>O<sub>3</sub> nanoparticles redispersed in octane and vortex mixed, along with their corresponding AFM Video Camera snap shots of the sample surface. The AFM cantilever was present in snap shots. 70
- Figure 37:** Effect of  $\gamma$ -Fe<sub>2</sub>O<sub>3</sub> nanoparticle size distribution as a function of vortex mixing time. Octane is used as the solvent to disperse nanoparticles. 71
- Figure 38:** AFM images of samples containing  $\gamma$ -Fe<sub>2</sub>O<sub>3</sub> nanoparticles redispersed in toluene and vortex mixed, along with their corresponding AFM Video Camera snap shots of the sample surface. The AFM cantilever was present in snap shots. 72
- Figure 39:** Effect of  $\gamma$ -Fe<sub>2</sub>O<sub>3</sub> nanoparticle size distribution as a function of vortex mixing time. Toluene is used as the solvent to disperse nanoparticles. 73
- Figure 40:** A compiled chart showing the effects of all three redispersing solvents and vortex mixing on the average sizes of nanoparticles. 74
- Figure 41:** Results after attempting the method of ultrasonically cleaning the wafers, as used by Benitez et al. a) Appearance of Si wafer immediately after the ultrasonically cleaning in acetone, b) AFM Height image of a section of one sample with which this cleaning method was used. 76
- Figure 42:** Spin casted samples: a) AFM images of samples containing  $\gamma$ -Fe<sub>2</sub>O<sub>3</sub> nanoparticles redispersed in octane and vortex

mixed for 2 minutes and sonicated for 15 minutes, b) A plot of Spin Caster speed (rpm) vs. Average sizes of nanoparticles for each sample. 78

**Figure 43:** Spin casted samples: a) AFM images of samples containing  $\gamma$ -Fe<sub>2</sub>O<sub>3</sub> nanoparticles redispersed in toluene and vortex mixed for 2 minutes and sonicated for 15 minutes, b) A plot of Spin Caster speed (rpm) vs. Average sizes of nanoparticles for each sample. 79

**Figure 44:** AFM video camera snap shots of  $\gamma$ -Fe<sub>2</sub>O<sub>3</sub> nanoparticles redispersed in octane at various initial concentrations as indicated. The AFM cantilever was present in snap shot 3, only. The letters Q and D represent the program used. 81

**Figure 45:** AFM Images of sample 4, prepared at low concentrations, and spin casted at 3000rpm for 30 seconds. The AFM images are 10 $\mu$ m $\times$ 10 $\mu$ m in size. 82

**Figure 46:** A histogram of the AFM image in Figure 24 c), It was fitted with a Gaussian curve. The most frequently occurring average nanoparticle size (mode) is 3.68 $\pm$  1.4 nm. The average nanoparticle size is 5.42 $\pm$  3.6 nm. 83

**Figure 47:** A histogram of the AFM image shown in Figure 45 b). The solid line shows the Gaussian distribution. The most frequently occurring average nanoparticle size (mode) is 6.20 $\pm$  1.5 nm. The average nanoparticle size is 7.73 $\pm$  3.7 nm. 84

**Figure 48:** A histogram of the nanoparticles shown in Figure 45 c). The solid line is a fit done by using the Gaussian function. The most frequently occurring average nanoparticle size (mode) is 10.60 $\pm$  3.4 nm. The average nanoparticle size is 11.00 $\pm$  4.3 nm. 85

**Figure 49:** AFM video camera snap shots of  $\gamma$ -Fe<sub>2</sub>O<sub>3</sub> nanoparticles redispersed in octane at various concentrations as indicated. Program Q with 1000rpm was used to spin cast. 87

**Figure 50:** Images of sample 1, to which 0.15mg of nanoparticles were added, while suspended in solution, to the silicon wafer, which was spun at 1000rpm for 30 seconds. The AFM images are all 20 $\mu$ m $\times$ 20 $\mu$ m in size, for the exception of a) which is 10 $\mu$ m $\times$ 10 $\mu$ m in size. 88

- Figure 51:** The histogram of the AFM image in Figure 29 a). The solid line shows the Gaussian distribution. The most frequently occurring average nanoparticle size (mode) is  $36.684 \pm 10.4$  nm. The average nanoparticle size is  $38.50 \pm 8.7$  nm. There is a large particle size distribution in this sample. 89
- Figure 52:** The histogram of the AFM image in Figure 29 b). The solid line shows the Gaussian distribution. The most frequently occurring average nanoparticle size (mode) is  $5.87 \pm 0.0.268$  nm, with a fairly narrow size distribution. The average nanoparticle size is  $7.77 \pm 4.87$  nm. 90
- Figure 53:** The histogram of the AFM image in Figure 29 c), It was fitted with a Gaussian curve. The most frequently occurring average nanoparticle size (mode) is  $5.90 \pm 4.1$  nm, with a narrow size distribution. The average nanoparticle size is  $7.03 \pm 3.51$  nm. 91
- Figure 54:**  $\gamma$ -Fe<sub>2</sub>O<sub>3</sub> nanoparticles, in purple, are surrounded by a ‘cloud’ of surfactants (octanoic acid), blue, that are anchored to the surface of the nanoparticle. The two different methods used to measure the spacing between two nanoparticles: a) by subtracting the measured diameter of individual nanoparticles from the measured distance between the center of one nanoparticle and the center of the other b) by directly measuring the spacing between the two nanoparticles. Ideally, both methods should give similar results. 93
- Figure 55:** SEM image of a section of single aggregate of  $\gamma$ -Fe<sub>2</sub>O<sub>3</sub> nanoparticles. 94
- Figure 56:** SEM image of a single aggregate of  $\gamma$ -Fe<sub>2</sub>O<sub>3</sub> nanoparticles. 95
- Figure 57:** SEM image of an aggregate of  $\gamma$ -Fe<sub>2</sub>O<sub>3</sub> nanoparticles 96
- Table 1:** Surfactant Spacing (nm) 19
- Table 2:** Spin Coater Program and Settings 45
- Table 3:** Sample Preparation for this experiment. 46
- Table 4:** Average sizes calculated using Microsoft Excel from a sample set of 50 nanoparticles for each sample shown in Figure 22. 52

|  |    |
|--|----|
| <b>Table 5:</b> A compilation of average sizes for all three redispersing solvents as they relate to sonication period.            | 66 |
| <b>Table 6:</b> A compilation of average sizes for all three redispersing solvents as they relate to vortex mixing period.         | 74 |
| <b>Table 7:</b> Spin casted samples: tabulated compilation of spin casted samples for particles redispersed in octane and toluene. | 79 |
| <b>Scheme 1:</b> Molecular Structure of the Iron-octanoate complex   | 12 |
| <b>Scheme 2:</b> Molecular Structure of Trimethylamine.  | 16 |

## ABSTRACT

$\gamma$ -Fe<sub>2</sub>O<sub>3</sub> maghemite nanoparticles were synthesized via the homogeneous thermal decomposition of iron pentacarbonyl. This synthesis took place in the presence of a capping molecule, octanoic acid, and a mild oxidant, trimethylamine oxide. The presence of octanoic acid capped  $\gamma$ -Fe<sub>2</sub>O<sub>3</sub> nanoparticles was confirmed using AFM, UV-Vis and FTIR. The use of different solvents, agitation periods, casting methods and  $\gamma$ -Fe<sub>2</sub>O<sub>3</sub> nanoparticle concentration, as parameters, were hypothesized to significantly influence the monodispersity, crystallinity and assembly of the particles. The nanoparticles were re-dispersed in three different solvents: hexane, octane and toluene, after which they were sonicated (0min, 5min, 10min, 15min, 20min, 30min), vortex mixed (0min, 2min, 4min, 6min, 8min), or sonicated and vortex mixed (2min vortex mixing and 15 min sonication). They were then drop-casted or spin casted on silicon wafers to observe the assembly under AFM or SEM. AFM was further used to characterize the size and distribution of  $\gamma$ -Fe<sub>2</sub>O<sub>3</sub> nanoparticles. The AFM imaging, followed by histogram analysis, shows that the diameter of nanoparticles can vary from ~3-40 nm with averages ranging from 1.84 nm to 47.23 nm. Spin casting was successfully used to remove aggregates from the center of the substrate, leaving a fair amount of monodisperse nanoparticles at the center. SEM imaging of three-dimensionally packed nanoparticles shows an average spacing of ~2nm between individual nanoparticles confirming the theoretical predictions.

## 1. INTRODUCTION

### 1.1 Nanotechnology

Nanotechnology is the manipulation of matter on the nanometer scale, in order to fabricate useful devices and materials.<sup>1</sup> Defined by size, the particles of interest range from 1 to 100 nanometers (nm): they are called “nanoparticles”, or “ultrafine particles”.<sup>2</sup> Nanoparticles have become popular because their mechanical and chemical properties have been observed to deviate greatly from the bulk material counterpart that is greater than 100nm in all dimensions. This is because below 100nm the molecular surface-to-volume ratio increases and makes a considerable difference in how the material behaves. As a result, these nanoparticles can be constructed into bigger, macroscopic structures, producing materials with new and cutting edge behaviors. These include, but are by no means limited to, paints, textiles, medical materials for drug diagnostics, targeting and delivery, skincare products and electronics.<sup>3</sup>

The use of nanoparticles, for what we now categorize as nanotechnology, date back to 2700 B.C. with the invention of Indian ink supposedly made in China. The production of this ink relied on the formation of Carbon nanoparticles in water. Still, it was not until Democritus and his teacher, Leucippus, proposed the concept of the “a-tomon” (Greek for “uncuttable”) that anyone, on record, ever thought of or philosophized about anything as small as the atom.<sup>4</sup> They both proposed that matter is not continuous; there has to be a point at which matter can no longer break down into smaller parts. We now know that this ‘smallest part’ is

the atom. Democritus' philosophy reminds us of the importance of the atom and the analysis of materials on the smallest scale.<sup>5</sup>

Iron, in particular, behaves differently as an atom and as a nanoparticle than it does as its bulk counterpart. Like the Nickel and Cobalt atoms, Iron atoms behave as magnets with permanent dipoles. The strength of the magnetism is determined by the magnetic dipole moment,  $\mu$ , given by the equation below:

$$\mu = IA \quad (1)$$

where  $I$  is the circulated current created by the motion of electrons about the nucleus and  $A$  is the area of the enclosed loop of current. The interaction between two Iron atoms causes each to align their magnetization in the same direction; both combine to form a larger permanent magnet. This unusual phenomenon continues as the atoms combine forming crystals as large as 100nm in diameter. Beyond this size the material begins to behave like its bulk counterpart by eliminating its permanent dipole. This limit is known as the single-domain limit. The limitations corresponding to single-domain tell us that as size of the material decreases, the number of magnetic domains also decreases. This is because, for a bulk material, having more than one magnetic domain, separated by domain walls, can lower the overall energy, but as the size decreases to a nanometer-sized particle, the lowest energy state is achieved when the particle has only one magnetic domain, establishing no domain walls,<sup>6</sup> Figure 1.

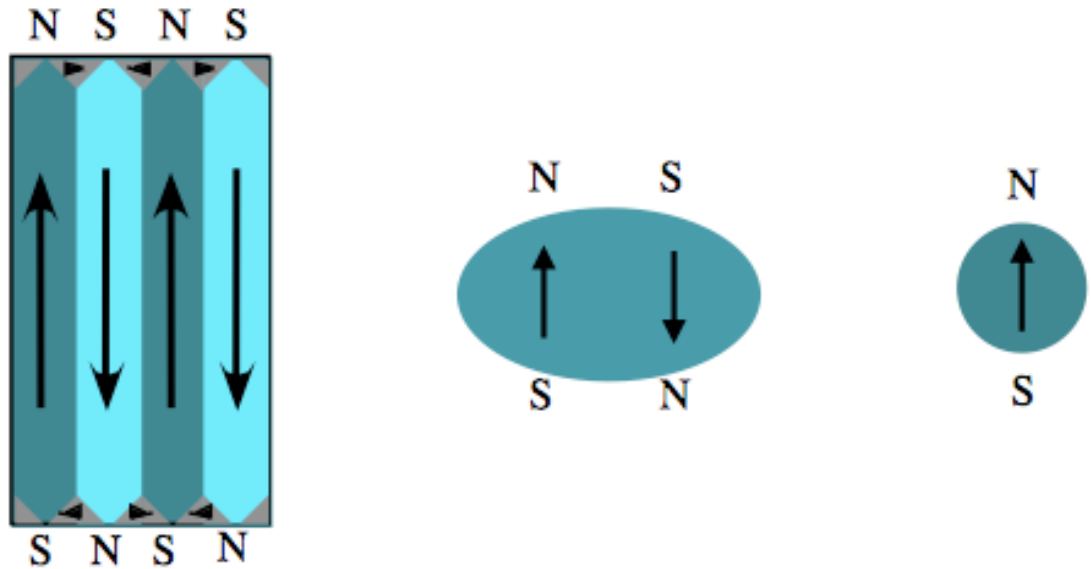


**Figure 1:** The magnetic domains of iron with respect to the size of the material.<sup>5</sup>

Another finite-size effect limit is the critical diameter. This is the diameter below which a nanoparticle can lose its magnetization in the absence of an external magnetic field: below a particular size, it can no longer behave as a permanent magnet. For iron, this critical diameter is 6nm. Hence below 6nm iron is super-paramagnetic; the magnetism of iron becomes unstable in the absence of a magnetic field. The super-paramagnetic limit is highly dependent on temperature because thermal fluctuations depend on temperature. Since thermal fluctuations decrease as temperature decreases, the super-paramagnetic limit decreases as temperature decreases. There is also a temperature above which particles of a certain size lose a stable magnetization and are unable to store data. This is known as the blocking temperature. Surface effects are another limitation

on the magnetic properties of iron: as the particle size decreases the percentage of surface atoms increases, and their surface spins contribute more to magnetism.

Since the magnetic properties of iron nanoparticles are size-dependent, these effects become considerably important when determining the potential storage density of a system for data storage applications.<sup>5</sup>

## **1.2 Data Storage**

Currently, data on hard disk is stored on a continuous film of densely packed magnetic nanoparticles. Information is stored in the form of magnetization oriented along a single axis that is perpendicular to the surface of the disk. The orientation along this axis mirrors the binary method of storing data, and essentially, each data bit consists of about 100, 10 – 20nm sized, nanoparticles (Figure 2).

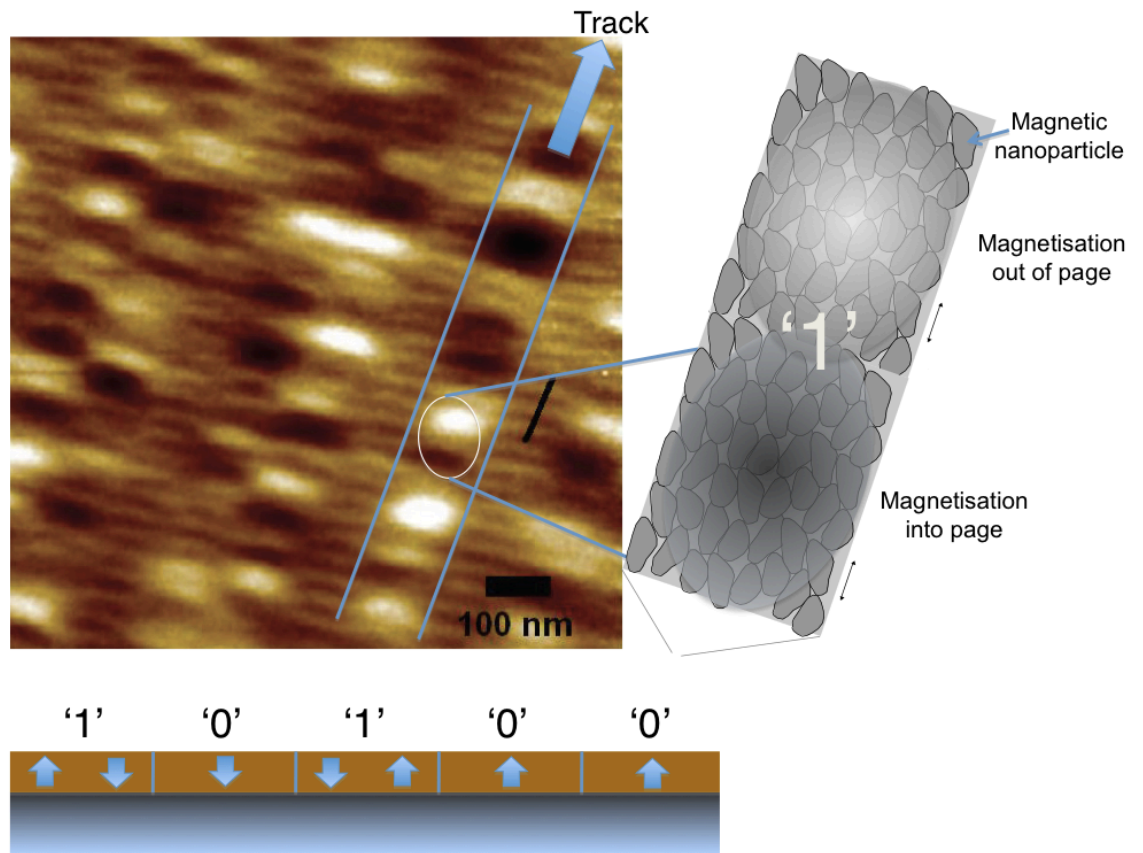


**Figure 2:** A Magnetic Force Microscope image of a 394 Gigabyte/inch<sup>2</sup> disk.<sup>5</sup>

As illustrated in the diagram above, within the area of one data bit can exist the presence of a magnetic reversal, which represents the presence of two different magnetizations within that area. The presence of a reversal serves for '1' and the absence of one serves for '0'.<sup>5</sup>

Rather than using one hundred nanoparticles to carry a single bit of data, it could be more efficient to use one magnetic nanoparticle to carry one data bit (Figure 3).

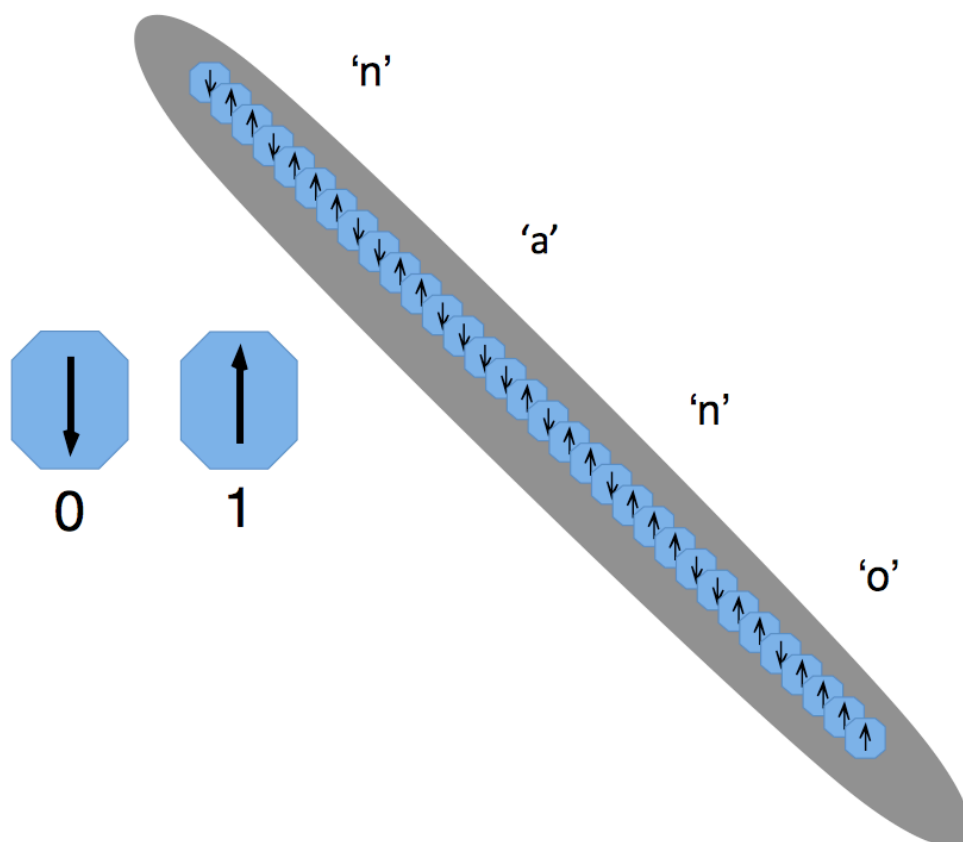


**Figure 3:** The hypothesized means of storing data on individual magnetic iron nanoparticles.<sup>5</sup>

Figure 3 above depicts a hypothetical example of storing data on single iron nanoparticles. If one nanoparticle represents one bit, the presence or absence of a reversal need not be considered. The magnetization is still oriented along a single axis, and so a magnetization oriented downwards could serve for '0', and that oriented upwards could serve for '1', as illustrated above. The feasibility of this hypothesis is limited to a favorable synthesis and assembly of these magnetic particles, as well as a way of magnetically manipulating them to write data.

### 1.3 Synthesis of Magnetic Nanoparticles<sup>6</sup>

In the past few decades, scientists have been developing methods of synthesizing magnetic nanoparticles for favorable assembly. They have proposed ways of controlling metal precursors and parameters during synthesis to produce monodisperse and crystalline arrays of nanoparticles.<sup>7</sup> Co-precipitation, Microemulsion, Hydrothermal Synthesis and Thermal Decomposition, are four common methods used for synthesizing magnetic nanoparticles.

In chemistry, **Coprecipitation** (CPT) can be used to synthesize iron oxide nanoparticles, such as  $\gamma$ -Fe<sub>2</sub>O<sub>3</sub> and Fe<sub>3</sub>O<sub>4</sub>, by adding a base to aqueous salt solutions of Fe<sup>2+</sup>/Fe<sup>3+</sup> under an inert atmosphere. The former soluble precursors are allowed to precipitate.<sup>8</sup> Varying the ratio of Fe<sup>2+</sup> to Fe<sup>3+</sup>, the type of salt used, the temperature of the reaction and the pH, not only varies the composition of the nanoparticles, but also the size and shape of them. Although this method is reproducible, the nanoparticles precipitated are inevitably polydisperse, which is unfavorable for data storage applications.

**Microemulsion** is the isotropic and thermodynamically stable dispersion of two immiscible liquids. The system is stabilized by surfactants implemented as an interface between the two liquids. For microemulsions of water-in-oil, water is dispersed as microdroplets surrounded by a layer of surfactants that have both a hydrophobic and hydrophilic end. The diameter of the dispersion domain is usually between 10 and 50nm in diameter, but can vary from 1 to 100nm.<sup>9</sup> To synthesize nanoparticles, two similar microemulsions are combined. By colliding,

fusing and splitting, the two types of micelles are able to exchange precursors. This results in precipitate formation within the micelles, which can then be extracted by adding a solvent to the mixture, like ethanol. Like Coprecipitation, the Microemulsion method also produces polydisperse nanoparticles. Also, the reaction yield of nanoparticles is low relative to other methods, and an excessive amount of solvent is needed to carry out a reasonable reaction.<sup>6</sup>

In **Hydrothermal Synthesis**, products are crystallized from aqueous solutions that are kept at high temperatures and vapor pressures. One type of method used is the liquid-solid-solution reaction. The system contains a liquid phase, a solid phase and a solution phase made distinct by interfaces across which there is a transfer of precursors to different mechanisms within each phase.<sup>10</sup> However little is known about this method as it relates to magnetic nanoparticle synthesis and reaction yield of nanoparticles. This method produces a very narrow size distribution of high-quality nanoparticles. Though the quality of synthesized nanoparticles is higher than those synthesized using the previous two methods, it is not as high as those synthesized by Thermal Decomposition.

In the **Thermal Decomposition** method of synthesizing magnetic nanoparticles, organometallic compounds are thermally decomposed in high-boiling organic solvents like dioctyl ether. The organometallic precursors include metal acetylacetonates, carbonyls and metal ions, like iron. Organic solvents contain surfactants, also known as ligands or capping molecules, for stabilization; for instance, oleic acid, lauric acid and octanoic acid are surfactants.<sup>6</sup> Although

the synthesis procedure is relatively complicated, requires an inert atmosphere, requires high reaction temperatures, and has reaction periods that can last from hours to days, the size distribution of particles is considerably narrow, the yield is high and the shapes of the nanoparticles can be controlled during synthesis. Owing to these advantages, the thermal decomposition method was chosen for  $\gamma$ - $\text{Fe}_2\text{O}_3$  nanoparticle synthesis.

#### **1.4 Nucleation and Growth Steps of $\gamma$ - $\text{Fe}_2\text{O}_3$ Nanoparticles During Thermal Decomposition**

Byung Hyo Kim *et al.* used MALDI-TOS (matrix-assisted laser desorption/ionization time of flight) mass spectrometry (MS), to monitor the formation of iron oxide nanoparticles, Figure 4.

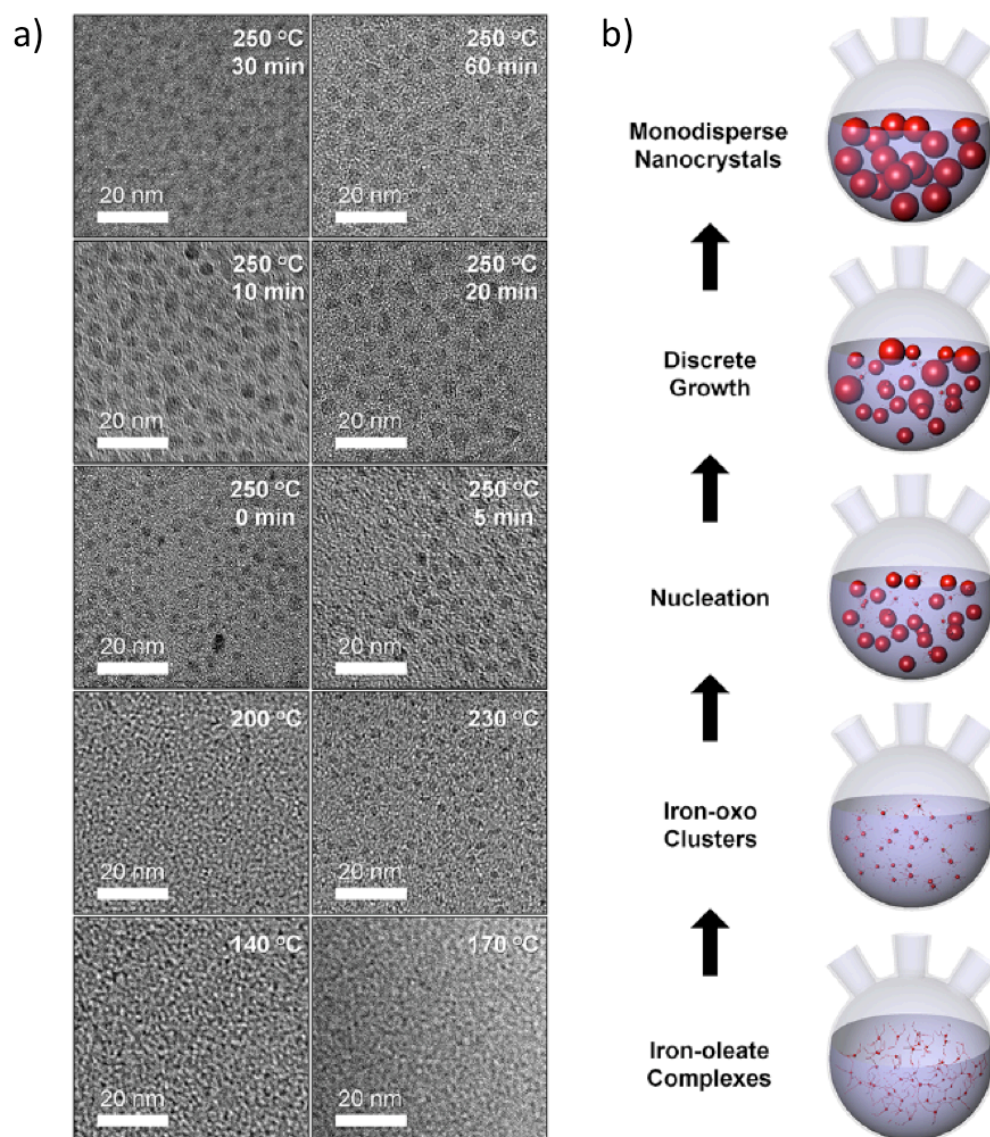


**Figure 4:** (a) TEM images of samples extracted from solution during synthesis (b) Proposed schematic diagram of nucleation and growth process. Samples were extracted at the intervals indicated above.<sup>11</sup>

Byung Hyo Kim *et al.* used MALDI-TOS (matrix-assisted laser

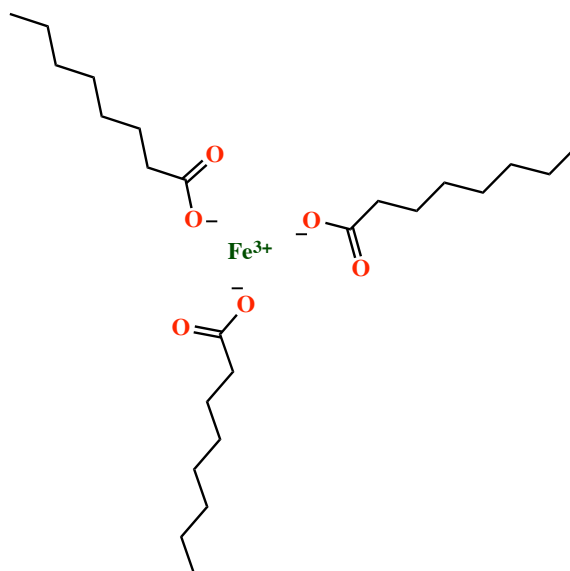
desorption/ionization time of flight) mass spectrometry (MS), to monitor the

formation of iron oxide nanoparticles, Figure 4.

The mechanism of iron oxide nanocrystal formation, with oleic acid surfactants in

their case, begins with the formation of iron-oleate complexes when iron precursors decompose during synthesis. The decomposition is facilitated by the reaction between dissociated oleic acid molecules and iron pentacarbonyl (3:1 optimum ratio).<sup>12</sup> This 3:1 ratio ensures that there is sufficient surfactant present to obtain a favorable particle size and particle quality.<sup>13</sup>

It is also expected that iron-octanoate complexes, as synthesized for this experiment, would begin to form in a similar manner to the iron-oleate complexes in Hyeon et al.'s report, Scheme 1.



**Scheme 1:** Molecular Structure of the Iron-octanoate complex

As temperatures continue to rise, as Hyeon et al. report, iron-oxo clusters form, which consist of a coordinated ratio of iron atoms to oleate molecules (~8:11). Iron-oxo clusters then accumulate to form 2.0nm-sized nanocrystals and the larger clusters continue to grow. Further increases in temperature and aging (reflux at

high temperatures for extended periods) lead to further growth (nucleation) of crystals, and hence cluster consumption, as nanocrystals grow.<sup>11</sup>

### **1.5 Influential Parameters for Synthesis of $\gamma$ -Fe<sub>2</sub>O<sub>3</sub> Nanoparticles by Thermal Decomposition**

Thermal decomposition is the most studied method of synthesizing magnetic nanoparticles. It has been successful in synthesizing oxides and semiconductor nanocrystals of high quality and high yield. Essentially, by using this method, iron (III) oxide nanocrystals ( $\gamma$ -Fe<sub>2</sub>O<sub>3</sub>) can also be synthesized. Also, by varying the ratio of iron metal to surfactant, along with the reaction temperature, the reaction time, the nanoparticle aging and other influential parameters, the size and morphology of the magnetic nanoparticles can be controlled.

Previous research has shown that increasing the rate of temperature increase, during the decomposition of iron pentacarbonyl in the presence of the surfactant, increases the monodispersity of the nanoparticles, (Figure 5)

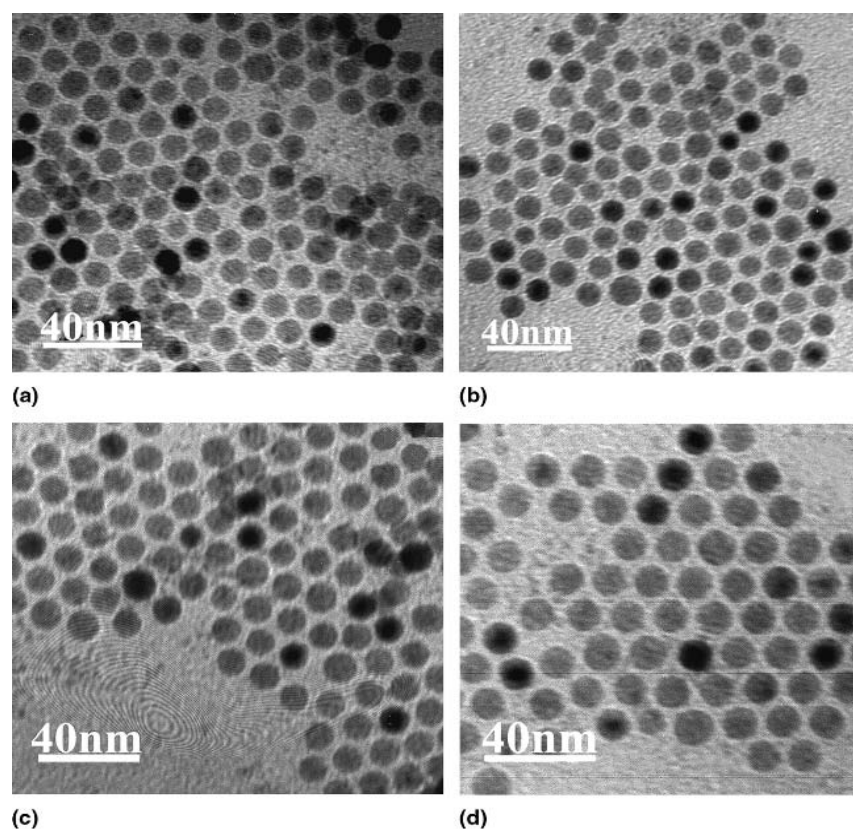


**Figure 5:** Increasing the rates of temperature increase for the decomposition, (a) 5°C/min, (b) 15°C/min, (c) 25°C/min and (d) 35°C/min.<sup>12</sup>

Figure 5 shows that as the rate of temperature increase increased from 5°C/min to 35°C/min, the disparity decreased from 12% to 3%.

Additionally, researchers have also reported an increase in monodispersity and crystallinity of particles due to an increase in the thermal decomposition reaction time, (Figure 6).

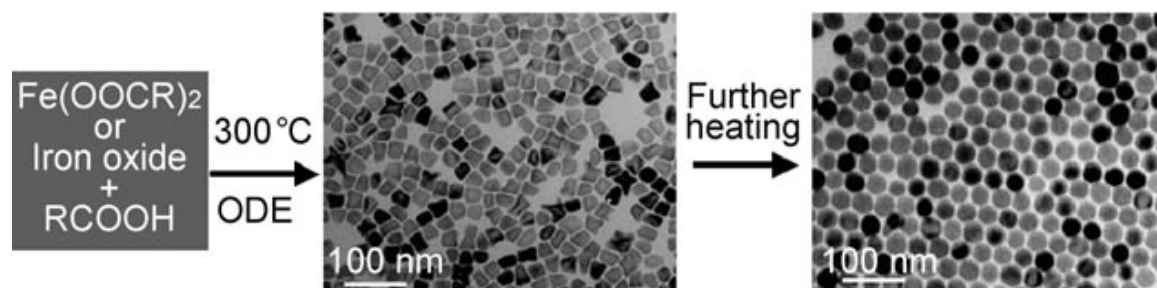


**Figure 6:** Synthesis of Fe<sub>3</sub>O<sub>4</sub> nanocrystals. The second and third panels are TEM images of the as-synthesized nanocrystals taken at different reaction times.<sup>14</sup>

By changing the length and the concentration of the surfactant, the reactivity can also be controlled. A faster reaction rate can be achieved by using a shorter surfactant, and if the rate of reaction is too slow due to an increase in length of surfactant, then primary amines or alcohols can both exponentially increase the rate and lower the reaction temperature.<sup>6</sup> In addition to the reaction rate, the decomposition temperature and the particle size increase as the length of the capping molecule increases, Figure 7.<sup>12</sup>

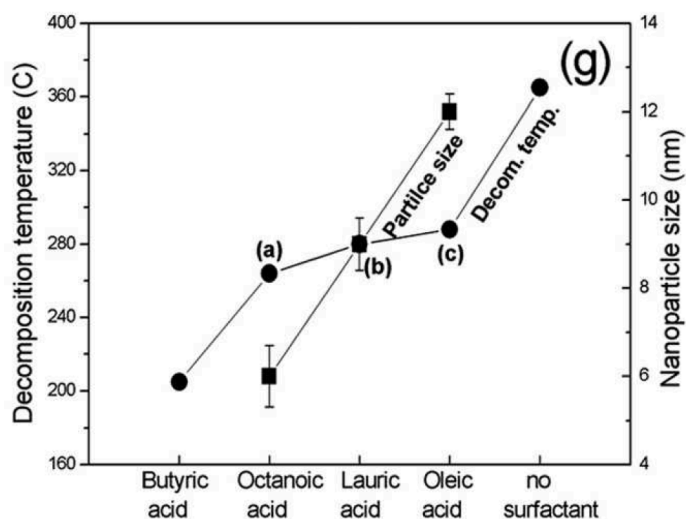
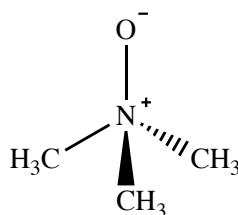


**Figure 7:** The decomposition temperature (°C) of iron pentacarbonyl and the nanoparticle size (nm) with different capping molecules.<sup>12</sup>

## 1.6 Protection and Stabilization of Fe Nanoparticles

Protection and stabilization of the particles are very important; after synthesizing these particles, they need to remain stable enough for the long-term. In this research project, the Fe nanoparticles are stabilized both by mild oxidation and surfactant coating to passivate the surface against external oxidation and agglomeration, respectively. Passivating the surface against external oxidation prevents the air molecules from affecting the functionality of pure metals (eg. Fe, Ni, Co) and alloys, which become even more air sensitive as surface to volume ratio increases. Therefore, by significantly decreasing oxidative air-sensitive catalysis, proper functionality can be maintained. Trimethylamine oxide was used as the mild oxidant for this experiment (Scheme 2).



**Scheme 2:** Molecular Structure of Trimethylamine.

Oxidizing the iron-oleate complex creates an iron oxide anti-ferromagnetic shell around the ferromagnetic iron core.

It is also important to passivate the surface against agglomeration. When this is done, a stable state of colloid-like  $\gamma$ -Fe<sub>2</sub>O<sub>3</sub> nanoparticles are produced due to dispersion via electrostatic and or steric repulsion. Surfactants are either chemically absorbed or physically anchored to the surface of nanoparticles. In this way, polymers containing certain functional groups (eg. Carboxylic acids) can

bind to the particle surface. Some examples of these polymers are poly(pyrrole), poly(aniline), polyesters, poly(lactic acid), poly(glycolic acid) and their copolymers. The following are surfactants, with carboxylic acid functional groups, Figure 8. In this experiment octanoic acid is used as the surfactant.

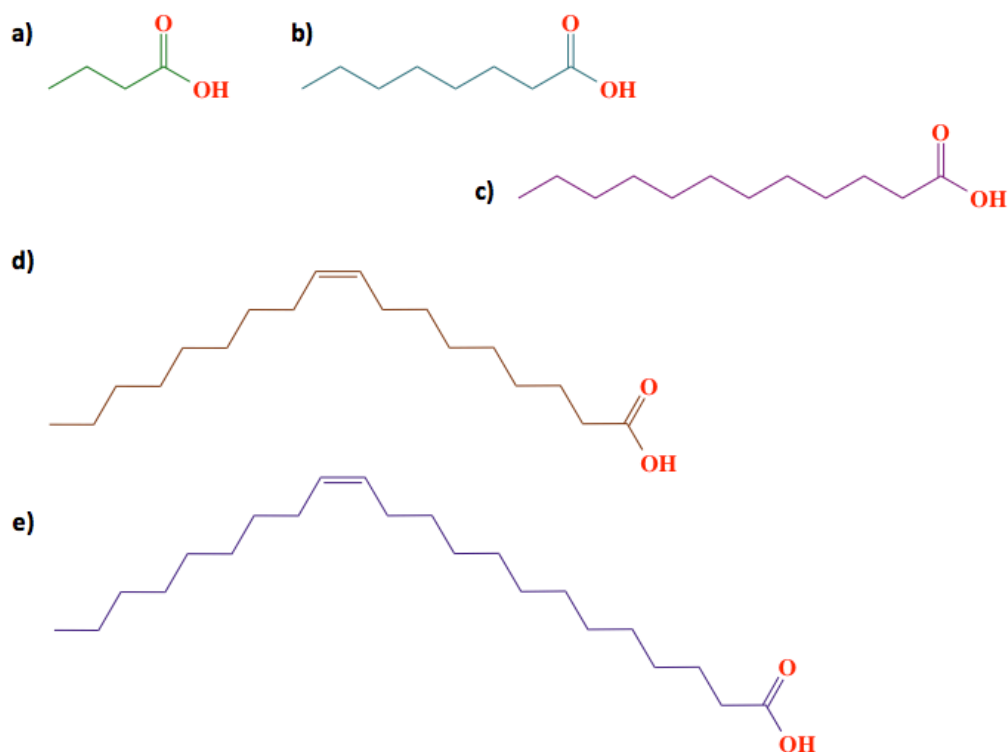


**Figure 8:** The molecular structures of surfactants that can be used in this research project; a) Butanoic Acid; b) Octanoic Acid (Caprylic Acid); c) Lauric Acid (Dodecanoic Acid); d) Oleic Acid ((9Z)-Octadec-9-enoic Acid); e) Erucic Acid ((Z)-Docos-13-enoic acid).

### 1.7 The Goal

This research project focuses on synthesizing magnetic material for data storage applications. To be more specific, the effects of certain  $\gamma$ -Fe<sub>2</sub>O<sub>3</sub> precursors on the

synthesis process, as well as the monodispersity of the produced nanocrystals, are being analyzed. The ligands are expected to increase the stability of the magnetic nanoparticles by preventing them from physically contacting each other. Therefore the magnetization is also expected to remain the same (unless changed externally). For shorter ligands, a longer synthesis time and narrower size distribution is expected. The opposite condition, however, is expected for longer ligands: a longer synthesis time and wider dispersion. It may also be possible to observe the effect that alkene functional groups have on the monodispersity of particles.

The goal of this project is to study the effect of length and conformation of each surfactant (capping molecule) on synthesis and overall self-assembly of the  $\gamma\text{-Fe}_2\text{O}_3$  nanoparticles. Ultimately, it is the intention to concentrate on measuring the spacing between the nanoparticles. (Figure 9)

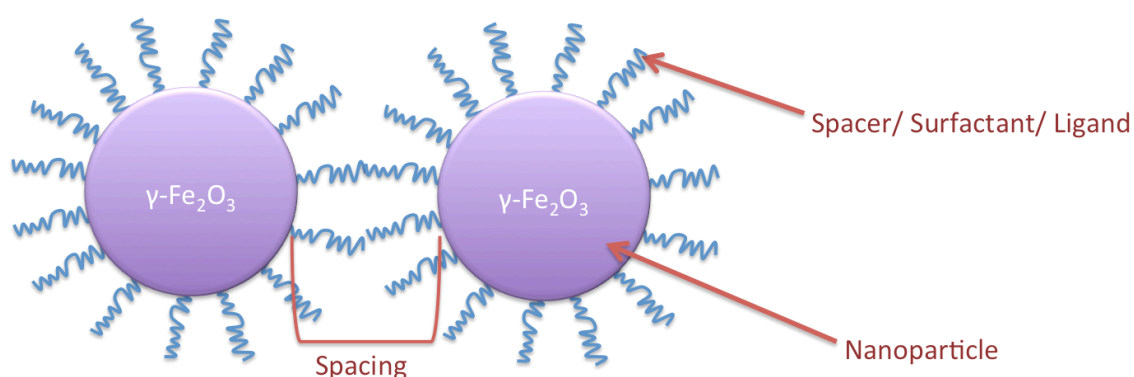


**Figure 9:** The self-assembly of two  $\gamma\text{-Fe}_2\text{O}_3$  nanoparticles.

Table 1 below shows the length of each ligand in units of nanometers, obtained from literature, Gaussian and simple calculations.

**Table 1:** Surfactant Spacing (nm)

| <b>Surfactant</b>    | <b>Spacing /nm<br/>(Literature)</b> | <b>Spacing /nm<br/>(Calculated)</b> | <b>Spacing /nm<br/>(Gaussian)<sup>15</sup></b> |
|----------------------|-------------------------------------|-------------------------------------|--|
| <b>Butanoic Acid</b> | -.--                                | 1.36                                | 1.31   |
| <b>Octanoic Acid</b> | 2.00                                | 2.40                                | 2.34   |
| <b>Lauric Acid</b>   | 3.50                                | 3.44                                | 3.22   |
| <b>Oleic Acid</b>    | 4.50                                | 3.80                                | 3.42   |
| <b>Erucic Acid</b>   | -.--                                | 5.10                                | 4.82   |

However before this can be accomplished, it is imminent to attain the best possible molecular self-assembly of the nanoparticles. For this purpose, nanoparticles need to be monodisperse and crystalline, which are characteristics that can only be obtained after using optimum synthesis and assembly conditions.

Nanoparticles have been characterized with Atomic Force Microscopy (AFM), Ultraviolet-visible Spectrophotometry (UV-Vis), Fourier Transform Infrared Spectroscopy (FT-IR) and Scanning Electron Microscopy (SEM) in order to verify and analyze the  $\gamma$ -Fe<sub>2</sub>O<sub>3</sub> nanoparticles and the spacing between them. UV-Vis and FT-IR spectroscopic methods can be used to verify the presence of nanoparticles and capping molecules. It is possible to measure the space between small nanoparticles with high resolution Atomic Force Microscopy (AFM) and high resolution Scanning Electron Microscopy (SEM). These characterization techniques will be discussed in this report.

## 2. INSTRUMENTAL METHODS

### 2.1 Spin Casting of Nanoparticles

Generally nanoparticles re-dispersed in a solvent can be casted onto a silicon wafer (substrate). Once the solvent gets evaporated a thin layer of nanoparticles remain. If the evaporation occurs too slowly, the nanoparticles, while still dispersed in the solvent, quickly agglomerate. Contrarily, if the solvent is evaporated at a faster rate, less agglomeration should occur. One way of casting is drop casting, which consists of dropping the nanoparticle-solvent solution onto a hot substrate for rapid solvent evaporation. Spin casting, also known as spin coating, consists of dropping the nanoparticle-solvent solution onto a rotating substrate for fast solvent evaporation.<sup>16</sup> The manner in which spin casting affects the assembly of the nanoparticles on the substrate can be explained by the concept of centrifugal force. Centrifugal force ( $F$ ) is a fictitious force that opposes centripetal force. As shown in Figure 10 below, centrifugal force acts outward.

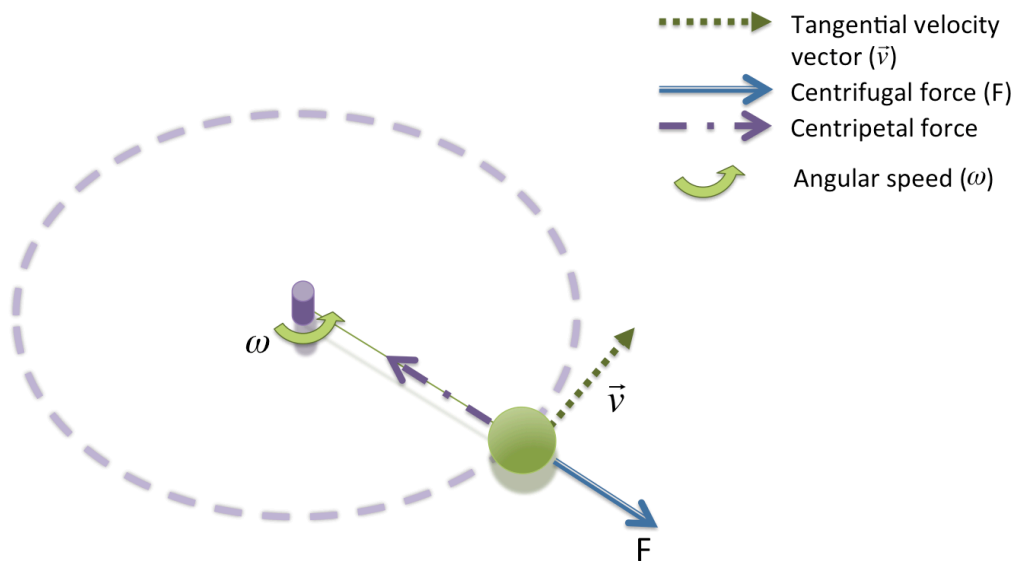


**Figure 10:** Centrifugal force acting outwards on a spherical body kept in a circular motion by a string.

Equation 1 below shows that centrifugal force is directly proportional to the mass of the particle ( $M$ ) it is acting on, the radius of the circular path ( $r$ ) and the speed of rotation ( $\omega$ ).

$$F = M\omega^2 r \quad (2)$$

where  $F$  is the centrifugal force and  $\omega$  is the angular speed of the particles. Since the centrifugal force is directly proportional to the mass of the particle, it is expected that, in samples of low concentrations, heavier particles will move further away from the center of the silicon wafer at a given angular speed. It is also expected that increasing the spin casting speed, of samples at low concentrations, will push larger particles out toward the edge of the wafer. Hence, the average size of the nanoparticles remaining in the center of the silicon wafer is expected to decrease as the angular speed increases. Figure 11 is an example of a

size distribution chart that could be observed for a sample set of nanoparticles in the center of a silicon wafer. In Figure 11 below, when the sample is spin casted using Program B, which has a slow angular speed, larger particles are expected to remain near the center of the silicon wafer. As the angular speed increases, the average size of nanoparticles expected to remain near the center decreases. Eventually Program D, which has the fastest angular speed is used, the smallest average size of nanoparticles should remain around the center of the silicon wafer.

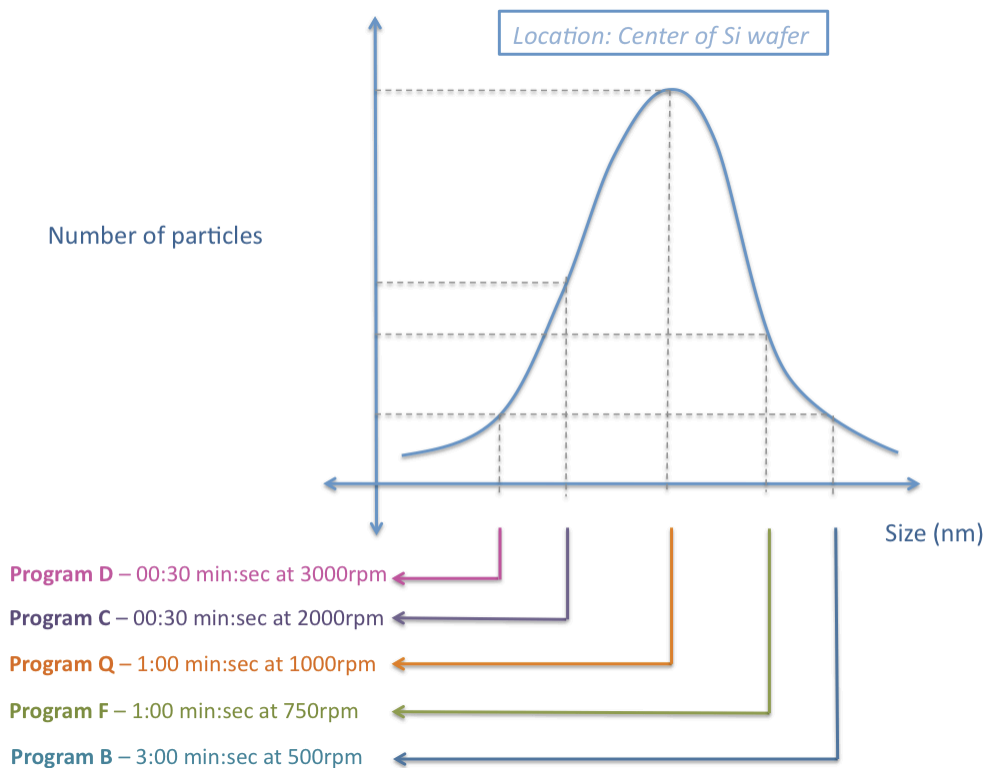


**Figure 11:** Example of a size distribution chart for a sample set of nanoparticles in the center of a silicon wafer that contains sample.

The results from both drop casting and spin casting will be compared in the results section.

## **2.2 Atomic Force Microscopy (AFM)<sup>17</sup>**

The atomic force microscopy (AFM) is a type of scanning probe microscopy: it uses a physical probe to scan the surface of a sample. It is able to form images with high resolution, on the order of fractions of a nanometer.<sup>18</sup> AFM was developed in 1986 by Binnig et. al., with a correction for a problem found in its close relative, the Scanning Tunneling (STM). This allows it to obtain images from insulating surfaces. The function of AFM, like the STM, is centered around an ultra-sharp tip that allows it to measure, image and manipulate of matter on the scale of a few nanometers. The AFM tip is mounted onto the end of a tiny cantilever, Figure 12.

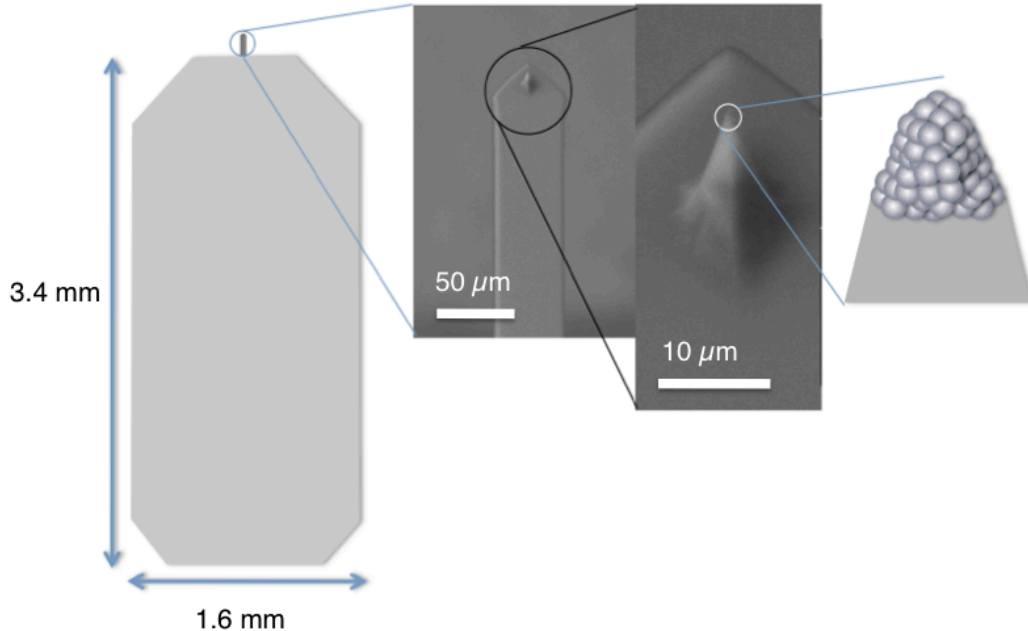


**Figure 12:** Atomic force microscopy functional probe. A tip protruding from a standard Commercial Cantilever that is mounted onto a Si based chip, also called a holder plate.<sup>17</sup>

In the ideal world the tip would be small enough for the radius of the apex to correspond to that of a single atom. In the real world, scientists have been able to manufacture sharp tips that have tip radii a few nanometers ( $<10\text{nm}$ ). It protrudes from the underside of a cantilever that is mounted onto a silicon or silicon nitride chip, also known as a holder plate, usually 3.4mm by 1.6mm in size, Figure 12.

The cantilever is then mounted onto a piezoelectric control device. This allows for fine movements with accuracy and a sub-nanometer precision of  $\sim 0.1\text{nm}$ . The piezoelectric control device is a ceramic tube that changes in size when a voltage is applied to it. By placing electrodes on the device and applying voltage across certain points, it is possible to get it to bend or to expand with sub-

nanometer precision control. Rather than scanning the sample at a constant height, which could cause damage to the tip and the sample, a feedback mechanism is used to adjust the distance between the tip and the sample. This allows for the maintenance of constant force between the tip and the sample.

In order to obtain information about the sample, the AFM needs to gather information from cantilever deflection, which results from tip-sample interaction. This information is gathered from the laser beam that is reflected onto the position-sensitive detector.

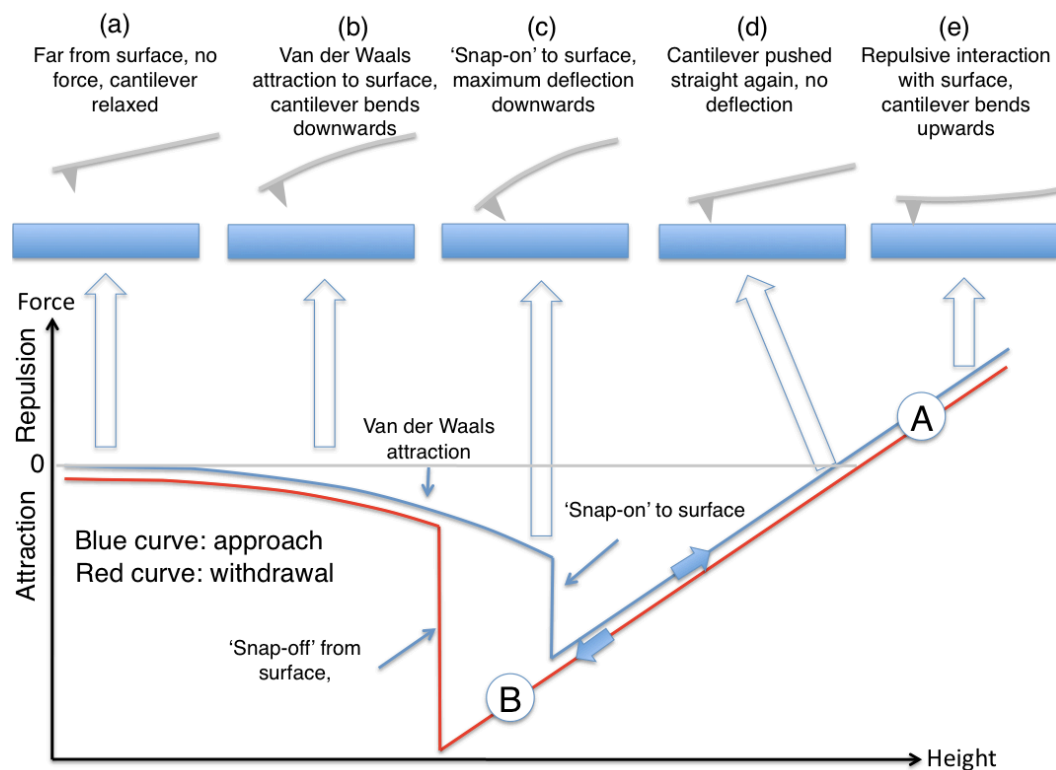


**Figure 13:** Cantilever deflection as it approaches the surface of the sample.<sup>17</sup>

The curves above (Figure 13) represent the measured force as a function of the decreasing height of the tip above the sample: the blue curve (top) represents the approaching tip and the red curve (bottom) represents the withdrawn tip. The images at the top of the figure correspond to the curve for the approaching tip: they help to illustrate the state of the cantilever at the various heights. The cantilever is relaxed when it is far from the surface of the sample (a). As the tip approaches the sample (b), the tip-sample interaction causes a downward deflection of the tip towards the sample. Tip-sample interactions result from interactive forces: a few examples of these forces are van der Waals forces, capillary forces, magnetic forces, solvation forces and electrostatic forces. Tip-sample interactive forces depend on the sample. The instrument measures this deflection. As the tip continues to descend onto the sample, it eventually reaches a critical distance. At this distance, the random thermal vibrations in the cantilever cause notably large swing towards the sample causes a larger tip-sample repulsive force that prevents the tip from returning to its relaxed position as it swings away from the surface. When the tip swings back towards the sample, it is closer to the surface, and on coming into contact with the surface (“snap on”), it reaches its maximum downward deflection (c). As the tip continues to descend onto the sample, the cantilever straightens out into a relaxed position (d). As the cantilever descends further, it begins to bend upwards (e). At this point, the repulsive forces increase, as depicted on the blue curve in Figure 13. Withdrawal, on the other hand occurs in the opposite direction, from (A) to (B) on the red curve. This force

curve is slightly shifted relative to the other, and the height at which the tip detaches itself from the sample (“snap off”) is further away from the “snap on” position. This is because the tip is already in contact with the surface and needs more withdrawal in order to detach from the surface.

The cantilever is fastened to the stage of the microscope, and during scans, a laser beam is aimed towards the back of the cantilever and is reflected from the cantilever onto a position-sensitive detector, which measures the cantilever deflection by the behavior of the reflected beam.

There are two basic modes used in AFM to obtain images: the contact mode and the non-contact mode, Figure 14. In contact mode, the tip is brought into contact with the sample, until it experiences a deflection force: either an attractive force (negative) or a repulsive force (positive). This means that the set-point force would be either negative or positive. The system then moves the cantilever in the x and y positions while altering the z position to keep the cantilever deflection force constant. To obtain an image, the system plots the x and y positions against the z position piezo voltage. In contact mode, the tip and sample are more easily damaged, than in tapping mode.

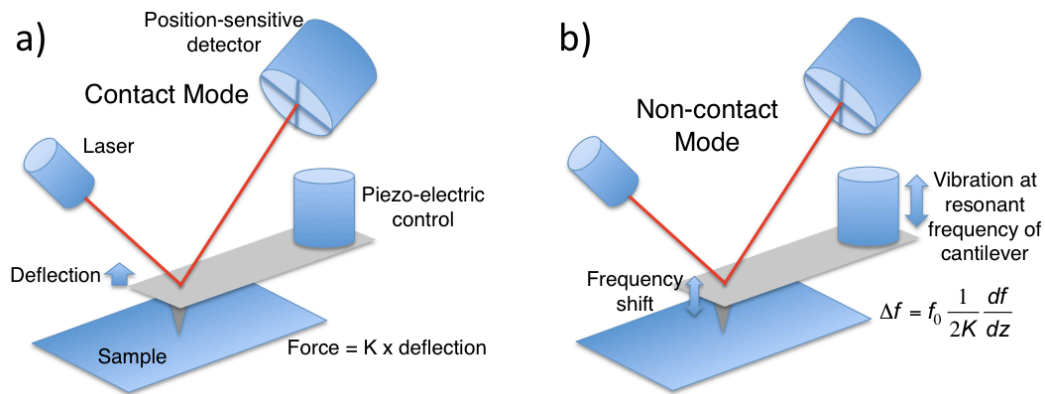


**Figure 14:** Atomic force microscopy functional probe showing, a) contact mode and b) non-contact mode.<sup>17</sup>

In non-contact mode the tip does not touch the surface of the sample, but is allowed to vibrate at its resonant frequency,  $f_0$ , usually 10 - 100kHz. The position-sensitive detector detects the cantilever's deflections from the reflected laser beam. As the tip descends unto the surface and is attracted to it, there is a frequency shift,  $\Delta f$ , Equation 2.

$$\Delta f = f_0 \frac{1}{2K} \frac{df}{dz} \quad (3)$$

where  $K$  is the cantilever's stiffness constant. The force between the tip and sample increases as the tip descends. As the probe scans in the  $x$  and  $y$  positions, the control system alters the  $z$  position in order to keep the frequency shift,  $\Delta f$ , constant. To obtain an image, the  $z$  position piezo voltage is mapped as a function of the  $x$  and  $y$  positions.

Non-contact mode, however, is faced with the challenge of a developing liquid layer on most samples. It makes tip-sample force detection difficult.

Tapping mode was invented to sidestep this problem.<sup>19</sup>

In tapping mode, the piezoelectric device, which is fixed to the AFM tip holder, allows the cantilever to oscillate close to its resonance frequency. As the tip descends closer to the sample, the amplitude decreases. The z position of the cantilever is adjusted to maintain a fixed cantilever oscillation amplitude during scans. Tapping mode is not in constant contact with the sample's surface, so imaging results only from the periodic tip-sample interactions.<sup>20</sup> Tapping mode is commonly preferred to constant mode, since less tip-sample interaction causes less damage to the sample. For this reason, tapping mode was used in this project, to verify the presence of, and to characterize the  $\gamma$ -Fe<sub>2</sub>O<sub>3</sub> nanoparticles.

### **2.3 Scanning Electron Microscopy (SEM)<sup>21</sup>**

Electron microscopy (EM) produces magnified images by using electron beams to irradiate specimens. Since electrons have wavelengths about 100,000 shorter than photons of visible light, electron microscopes can reveal the composition of smaller objects and have a superior resolving power to that of a light microscope.

A scanning electron microscope (SEM) is a type of electron microscope. It generates images by scanning a sample with a directed and focused beam of electrons. The electrons in that beam interact with the atoms in the sample. This interaction leads to the production of signals that the instrument can detect and process in order to relay information about the surface topography and composition of the sample. The beam of electrons uses the raster scan pattern

method of scanning. The instrument uses the combination of the electron beam position and the detected signals to generate the image.

The SEM produces different types of signals, which result from interaction of the beam with atoms at the surface or near to the surface of the sample. These signals include secondary electrons (SE), back-scattered electrons (BSE), light cathodoluminescence (CL), characteristic X-rays, transmitted electrons and specimen current. Rarely is there an instrument, however, that will contain detectors for all of these signals.

The most common detectable signal processed by the SEM is the secondary electrons that atoms emitted when excited by the focused electron beam. In fact, secondary electron detectors are standard for all SEMs. The amount of secondary electrons emitted is proportional to the angle between the surface and focused electron beam. When the surface is flat, the sample contains most of the secondary electrons. However, when the surface is tilted, more secondary electrons are exposed: this leads to the emission of more electrons from the surface of the sample. SEM is able to generate images with high resolution, enough to reveal details that are smaller than 1nm. Also, because the electron beam is narrow, the micrographs obtained have a large depth of field. Depth of field, in optics, refers to the perceived distance between the nearest and farthest objects present in a fairly sharp image. This large depth of field, allows the generated image to have a three-dimensional appearance, which contributes to the understanding of sample topography and surface features. The range of acceptable

magnifications is wide for SE generated images, spanning from  $10\times$  to  $500,000\times$ , the latter being about 250 times the limit of powerful light microscopes.

Since the topography of the sample being analyzed was more important for this report, the secondary electron analysis technique was used.

The figure below (Figure 15) shows a schematic of the SEM instrument.

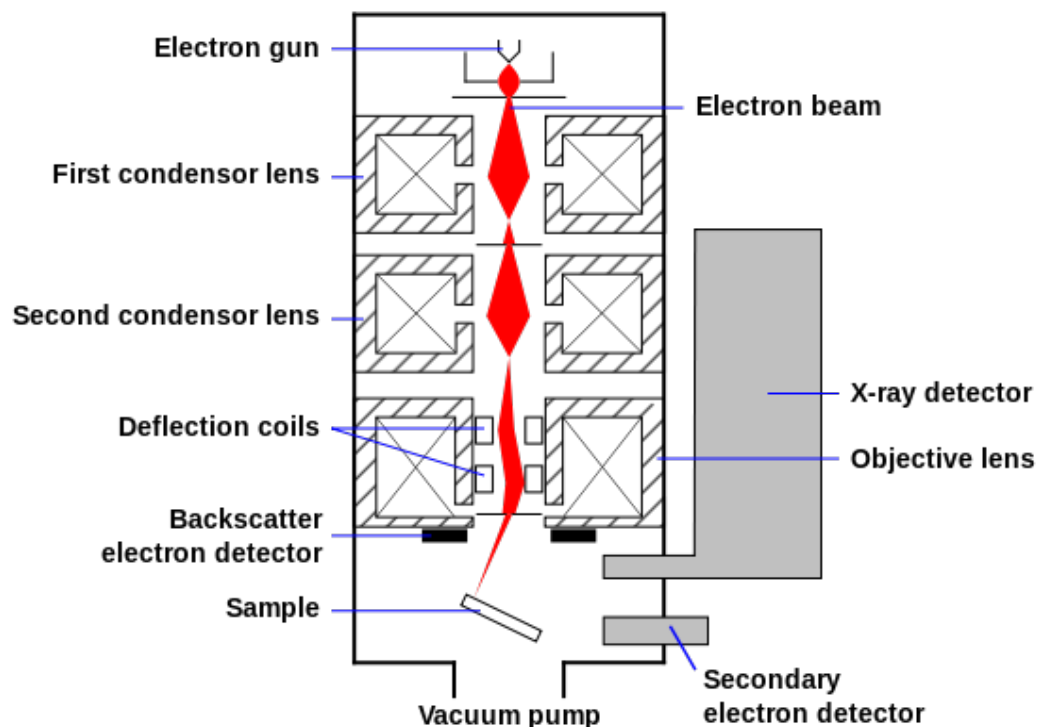


**Figure 15:** A schematic diagram of a typical Scanning Electron Microscope (SEM).<sup>21-22</sup>

As depicted in the diagram above, generally in SEM an electron beam is emitted from an electron gun. The electron gun is fitted with a tungsten filament cathode. Tungsten is usually used for this purpose, thermoionic electron guns, not only because of its low cost, but also because it has the lowest vapor pressure and

the highest melting point of all the metals. This allows it to be heated for the emission of electrons.

The energy of the electron beams usually ranges from 0.2 keV to 40 keV. After the beam is emitted from the electron gun, it then passes through one or two condenser lenses, which focus the beam to a spot of about 0.4 nm to 5nm in diameter. In fact, the spatial resolution of the SEM image generated would depend on the size of the electron spot and the extent of interaction of the sample with the beam. The electron spot depends on the wavelength of the electrons and the system that generates the scanning beam. After passing through the condenser lenses, the beam passes through pairs of deflection coils, usually in the final lens; the coils deflect the beam in the x and y axis in order to scan the surface of the sample with the raster scan method. The raster scan is done over a rectangular area of the surface.

As discussed previously, the exchange of energy between the primary electron beam and the sample, brings about the reflection of high-energy electrons, via the inelastic scattering of emitted secondary electrons, via the elastic scattering of electrons and via electromagnetic radiation emission. The corresponding detector, as shown in Figure 15, can detect each of the emitted electrons.

## 2.4 Ultraviolet-visible Spectrophotometry (UV-Vis)<sup>23</sup>

Ultraviolet-visible spectroscopy refers to the absorption of radiation as a function of wavelength in the ultraviolet-visible spectral region. The ultraviolet-visible region refers to use of light in the visible region and the adjacent, near-infrared (NIR) and near-UV regions. When chemicals absorb or reflect light in the visible region, the colors perceived are affected. This is because the molecules in that chemical undergo electronic transitions from the ground state to the excited state. The UV-Vis spectrometer measures these electronic transitions.<sup>23</sup> The molecules that are capable of absorbing energy in the form of ultraviolet or visible light are those containing  $\pi$ -electrons or non-bonding electrons. When these molecules absorb light, those electrons are excited to higher anti-bonding molecular orbitals.<sup>24</sup> If the electrons within that molecule are easily excited, then the molecule is able to absorb longer wavelengths of light. This is because the lower the energy gap between the highest occupied molecular orbital (HOMO) and the lowest unoccupied molecular orbital (LUMO), the less energy is needed to excite an electron from the HOMO to the LOMO.

The UV-Vis spectrophotometer directly measures  $I$ , the intensity of light that passes through the sample, and compares it with  $I_0$ , the initial intensity the light had before it passed through the sample. The  $I/I_0$  ratio is usually expressed as transmittance ( $T$ ), in percentage. The equation below shows how the absorbance,  $A$ , is related to the transmittance.

$$A = -\log\left(\frac{I}{I_0}\right) \quad (4)$$

The spectrophotometer consists of four basic parts: the sample holder, the light source, a monochromator or prism containing a diffraction grating to separate the different wavelengths of light and a detector, Figure 16.

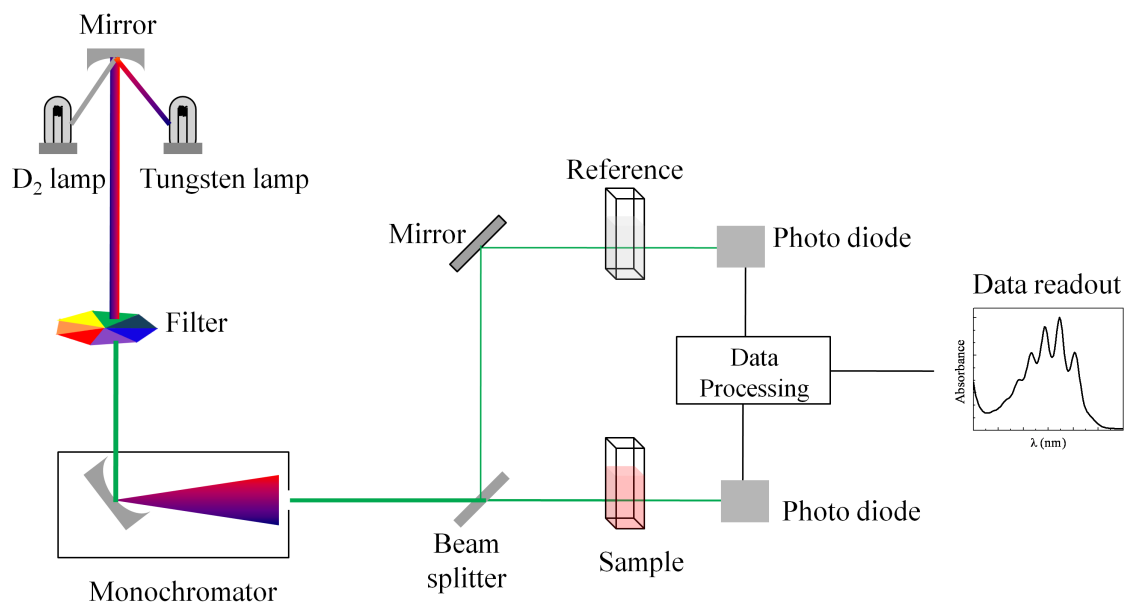


**Figure 16:** A schematic diagram of the UV-Vis spectrophotometer.<sup>25</sup>

The radiation source usually consists of a Tungsten filament, which is continuous from 300-2500nm; a Xenon arc lamp, which is continuous from 160 to 2000nm; a deuterium arc lamp which is continuous from 190 to 400nm, the ultraviolet region; and for visible wavelengths, the light emitting diodes (LED). The detector is usually a photodiode, a photodiode array, a photomultiplier tube, or a charge-coupled device.

There are single beam and double beam spectrophotometers. In a single beam, commonly used in teaching labs and industrial labs, all of the light is allowed to pass through the sample cell. The initial intensity,  $I_0$ , therefore needs to be measured separately by removing the sample from the solution having a reference, which is usually measured first and set to have zero absorbance. In a double beam, Figure 16, the light, before reaching the sample, is split into two beams. One passes through the sample and the other is used as a reference. The reference beam is set to have zero absorbance (100% transmittance). The measurements will take into account the  $I/I_0$  ratio between the sample and the reference. Due to the presence of two photodiode detectors, unlike the single beam, the sample beam and the reference beam can usually be measured at the same time.

A single beam instrument was used to characterize the  $\gamma\text{-Fe}_2\text{O}_3$  nanoparticles. Since Fe atoms have valence electrons that can be excited from HOMO to LUMO, the presence of Iron can be confirmed with UV-Vis spectrometry: a peak corresponding to this transition should be observed on the spectrum.

## **2.5 Fourier Transform Infrared Spectroscopy (FT-IR)<sup>26</sup>**

Fourier transform infrared spectroscopy obtains an infrared spectrum of Raman scattering, photoconductivity, absorption or emission of a solid, liquid or gas. FT-IR is able to collect electromagnetic spectral data in a wide range. The

'Fourier Transform' term in FT-IR refers to a mathematical process used to convert the raw data collected by the spectroscope into the desired spectrum. FT-IR and UV-Vis, both absorption spectroscopes, measure how efficiently a sample is able to absorb initial beam(s) of light at each wavelength. Rather than shining a monochromatic light beam through the sample, like UV-Vis spectrometers, FT-IR shines light of many different frequencies, all at once, in a single light beam. It then measures how much of the light from the beam is actually absorbed by the sample. After recording the first data point, the instrument modifies the light beam to contain a different frequency combination to gather information for the next data point. This modification occurs many times, and is followed by a recollection and assessment of the collected data concurrent with an inference of the absorption corresponding to each wavelength.

The initial beam generated is a broadband light source, which is ideal for applications that require a wide spectral range. The broadband light source contains the full electromagnetic spectrum of wavelengths that are to be measured. That light is shone into a Michelson interferometer, Figure 17. The Michelson interferometer produces an interference pattern by using a beam splitter and mirrors to split the initial light beam into two different paths, and then allowing the beams to bounce back and recombine. The different paths may vary in lengths and or material composition.

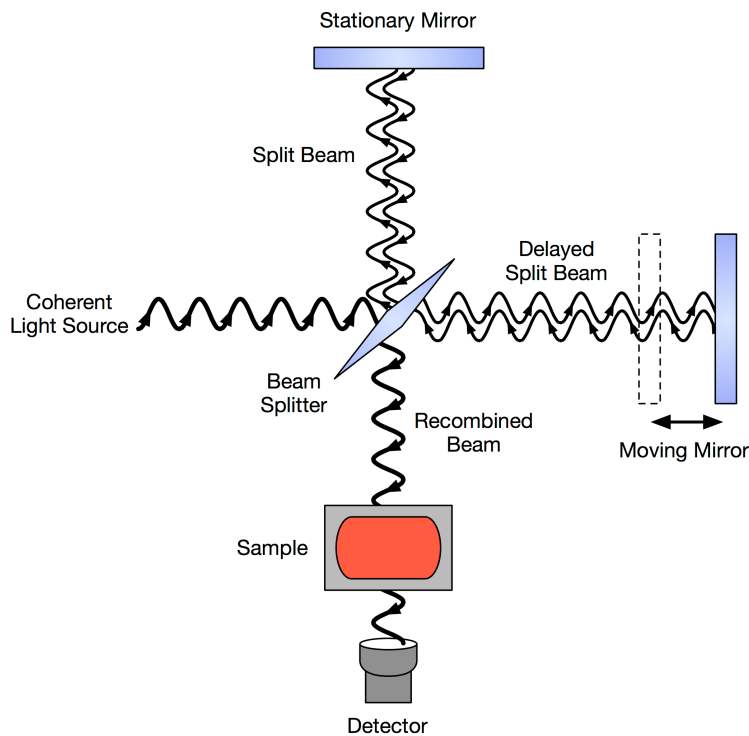


**Figure 17:** Schematic diagram of a FT-IR configured, Michelson interferometer.<sup>27</sup>

The mirrors in the Michelson interferometer are configured so that a motor can move one of the mirrors. As the motor moves the mirror, the Michelson interferometer uses wave interference to systematically block, transmit, block, and transmit each wavelength of light in the beam. The modulation of different wavelengths occurs at different rates to allow the beam, coming out of the Michelson interferometer, to have a different spectrum each time.

In order to convert the absorption of light for each mirror position, the raw data, into the absorption of light for each wavelength, the desired data, the computer processes the raw data using the fairly complex Fourier transform common algorithm. After which a spectrum of Transmittance (%) as a function of

Wavenumber ( $\text{cm}^{-1}$ ) is generated. From that spectrum, peaks corresponding to vibrational transitions characteristic of different bonds should be observed. These bonds include the C=O, C-H and O-H bonds in the octanoic acid surfactant molecules. Hence the presence of octanoic acid on synthesized  $\gamma\text{-Fe}_2\text{O}_3$  nanoparticles can be confirmed with FT-IR spectroscopy.

### 3. EXPERIMENTAL

#### 3.1 Synthesis of Monodisperse and Crystalline $\gamma\text{-Fe}_2\text{O}_3$ Nanocrystallites<sup>13</sup>

##### *Part (a) – Synthesizing monodispersed Fe nanoparticles*

The experiment was set up as shown in Figure 18 below.

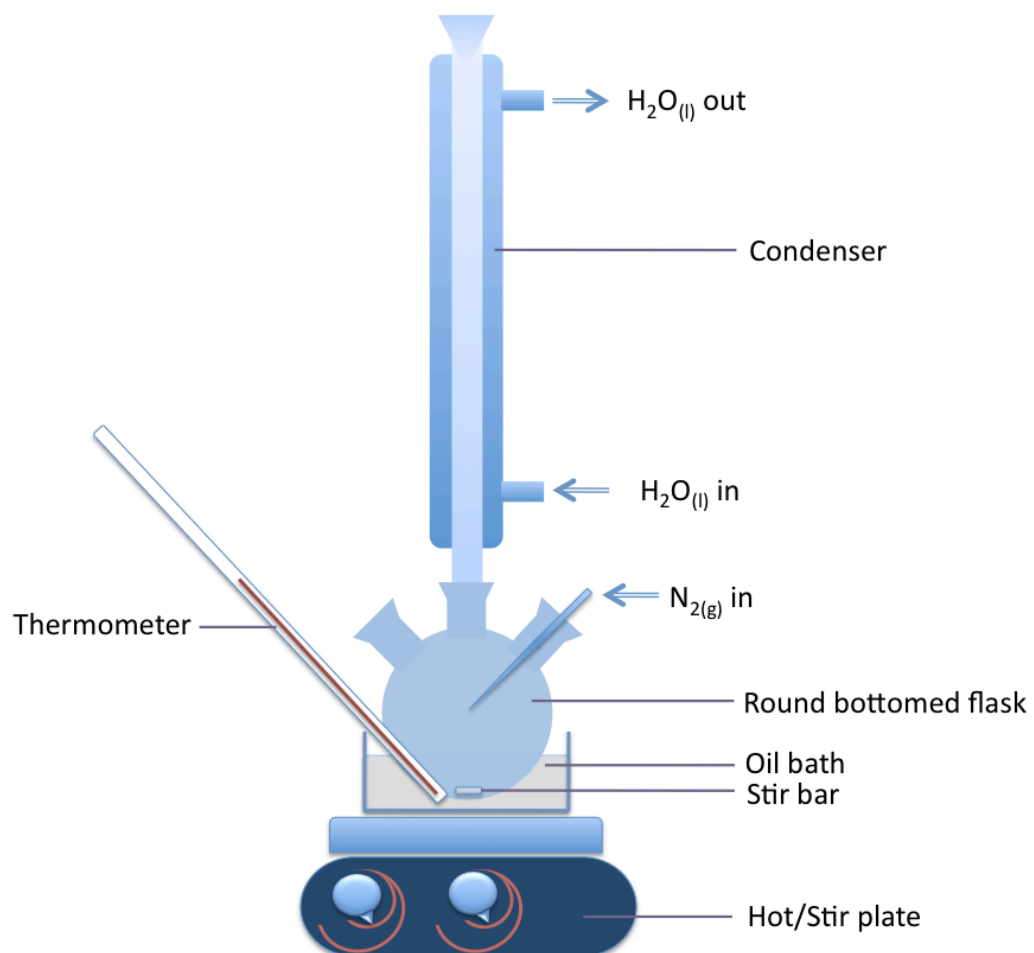


**Figure 18:** Apparatus for  $\gamma\text{-Fe}_2\text{O}_3$  Nanocrystallites synthesis using the Thermal Decomposition method.

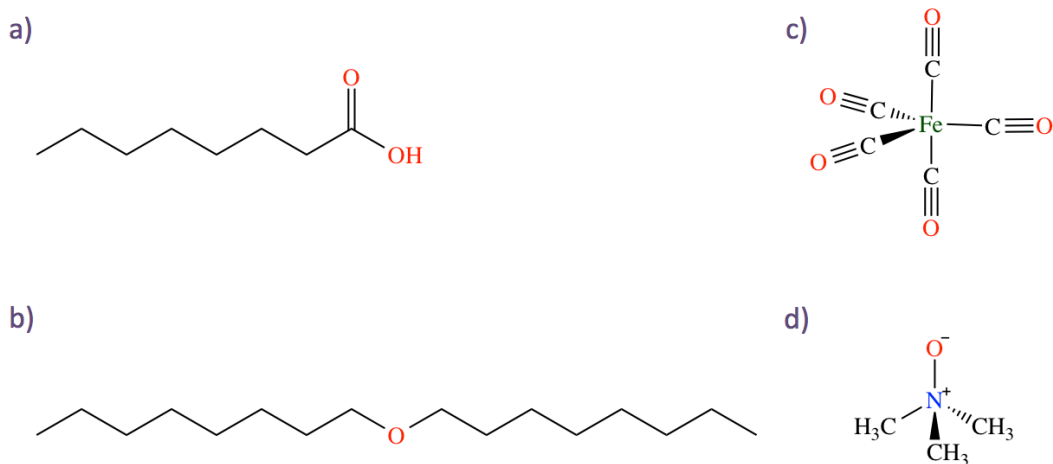


**Figure 19:** Molecular structures of  $\gamma$ -Fe<sub>2</sub>O<sub>3</sub> Nanocrystallite precursors: a) Octanoic Acid (Caprylic Acid), b) Dioctyl ether, c) Iron Pentacarbonyl, d) Trimethylamine N-oxide.

For the synthesis of Fe nanoparticles, 0.72ml (4.56mmol) of octanoic acid surfactant was dissolved in 10ml of dioctyl ether in the round-bottomed flask. This surfactant-solvent mixture was then heated quickly to 100°C, at which 0.2ml (1.52mmol) of Fe(CO)<sub>5</sub> was added. The temperature of the oil bath was used as an approximate indicator of the reaction temperature (Figure 18). The resulting orange colored mixture was heated to reflux at a rate of 30°C/min. The mixture was then left to reflux for 1 hour, within a temperature range of 280°C and 330°C. During reflux, a gradual color change from orange to black was observed. After reflux, the black mixture was allowed to cool to room temperature (~22°C). All chemicals were purchased from Sigma-Aldrich.

**Part (b) – Synthesizing  $\gamma$ -Fe<sub>2</sub>O<sub>3</sub> Nanocrystallites from the *Fe nanoparticle precursor***

Fe nanoparticles were oxidized to form  $\gamma$ -Fe<sub>2</sub>O<sub>3</sub> Nanocrystallites. In the second part of the synthesis, first, a continuous stream of nitrogen was pumped into the round-bottomed flask to establish an inert atmosphere only in Part (b) of the synthesis. To the black solution, 0.34g (4.56mmol) of anhydrous (CH<sub>3</sub>)<sub>3</sub>NO was added. Any openings to the round-bottomed flask were then sealed to prevent excess nitrogen flow out and unwanted oxygen flow in. The mixture was heated to 130°C, and that temperature was maintained for 2 hours. During the 2 hours, a color change from black to brown was observed. The brown solution was slowly heated to reflux at a rate usually slower than 5°C/min. The reflux temperature, within the range of 280°C and 330°C, was maintained for 1 hour. During reflux, a color change from brown to black was observed. After reflux, the black solution was allowed to cool to room temperature. Ethanol was then added to the mixture to precipitate the black solution, which was transferred to glass vials and stored at room temperature before washing.

### **3.2 Washing of Monodisperse and Crystalline $\gamma$ -Fe<sub>2</sub>O<sub>3</sub> Nanocrystallites**

To wash the  $\gamma$ -Fe<sub>2</sub>O<sub>3</sub> Nanocrystallites, the black solution was transferred to 1.5 ml Eppendorf® Microcentrifuge tubes and spun down at 133,000min<sup>-1</sup> for ~15min in the Microcentrifuge (Fisher Scientific Micro 17R) to extract the original solvents from the solution. The remaining solid was then redispersed in

hexane, octane or toluene, and spun down again to extract unwanted material from the solution. The  $\gamma$ -Fe<sub>2</sub>O<sub>3</sub> Nanocrystallites were washed 3 to 4 times and stored at room temperature (~22°C).

### **3.3 Solvent Selection**

Three solvents were chosen for the redispersion of  $\gamma$ -Fe<sub>2</sub>O<sub>3</sub> nanoparticles: hexane, octane and toluene. These solvents have different molecular structures and boiling points and were expected to influence the redispersion and molecular self-assembly of the  $\gamma$ -Fe<sub>2</sub>O<sub>3</sub> nanoparticles differently. To test their effectiveness, nanoparticles that were redispersed in these solvents were agitated for set periods and drop casted (1 drop), using a short glass pipette, onto a cleaned silicon wafer substrate cut into ~1.0cm by ~1.5cm rectangular pieces. The wafers were then placed on a hot plate on low heat, in order for the hydrocarbon solvent to fully evaporate. Atomic Force Microscopy was then used to characterize the nanoparticles and the self-assembly for the different solvents.

### **3.4 Agitation Method (Vortex Mixing vs. Sonication)**

Two methods were used to agitate  $\gamma$ -Fe<sub>2</sub>O<sub>3</sub> nanoparticles and break up aggregates: vortex mixing and sonication.

Vortex is the motion of a fluid flowing rapidly in a spinning motion around an invisible center. The rate and speed of vortical flow is fastest at the center of the vortex and slows down as one moves outward. Thus this method was

used to thoroughly mix solutions in order to break up aggregates. The Fisher Scientific Analog Vortex Mixer was used. All samples were mixed at ‘Speed 10’, 3200rpm.

$\gamma$ -Fe<sub>2</sub>O<sub>3</sub> nanoparticles redispersed in hexane, octane and toluene were agitated for 0.00, 2.00, 4.00, 6.00 and 8.00 minutes. Although the concentration was not measured, it was kept constant, since all samples were extracted from the same Eppendorf® tubes.

Sonication agitates particles through the application of ultrasonic energy to a sample. Usually, as in this report, nanoparticle-solution samples were put in a water bath (ultrasonic probe) through which the sound waves propagated. The Ultrasonic cleaner, Bransonic 1510R-MTH, was used.  $\gamma$ -Fe<sub>2</sub>O<sub>3</sub> nanoparticles redispersed in hexane, octane and toluene were agitated for 0.00, 5.00, 10.00, 15.00, 20.00 and 30.00 minutes. Although the concentration was not measured, it was kept constant, since all samples were extracted from the same volumetric flasks.

After vortex mixing or sonicating, particles were drop casted onto cleaned silicon wafers.

### **3.5 Silicon wafer cleaning**

Two cleaning procedures were attempted and their effectiveness assessed by analysis of the topography under AFM.

The first, and most used entailed rubbing the surface with nitrile gloves (Kimberly-Clark) under a strong stream of distilled water, drying with compressed air, placing on a hot plate on low heat for ~5minutes and storing in 24 well plate inside of a desiccator, before use.

The second procedure, used by Benitez et al.,<sup>28</sup> entailed ultrasonically cleaning the silicon wafers in acetone for 15 minutes, as shown in Figure 20 below.

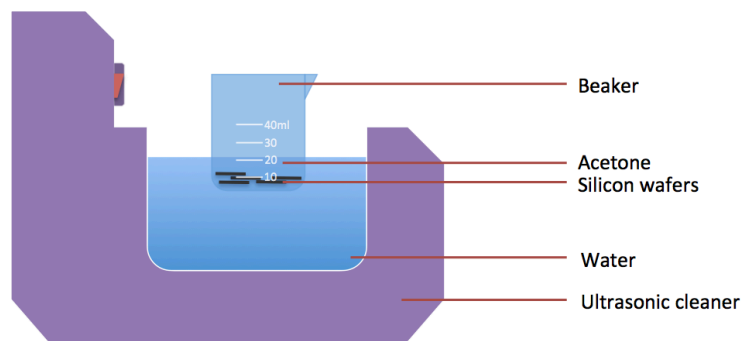


**Figure 20:** Side view and annotated diagram of the set up for ultrasonically cleaning the silicon wafers.

The Silicon wafers were then rinsed with isopropanol and dried under a Nitrogen gas ( $N_2$ ) stream.

### 3.6 Spin casting Settings

The WS-400-6NPP-Lite Spin Coater (Laurell Technologies Corp.) was used to spin cast samples. In order to determine the best spin casting setting for favorable molecular self-assembly, different programs were used:

**Table 2:** Spin Coater Program and Settings

| Program | Settings       |             |
|---------|----------------|-------------|
|         | Time (min:sec) | Speed (rpm) |
| B       | 3:00           | 500         |
| F       | 1:00           | 750         |
| Q       | 1:00           | 1000        |
| C       | 0:30           | 2000        |
| D       | 0:30           | 3000        |

The concentration of nanocrystallites in octane was 1.9 mg/ml, and in toluene, 1.6 mg/ml. Concentrations were kept constant. All samples for octane were taken from the same Eppendorf® tube and all samples of nanoparticles dispersed in toluene were taken from the same Eppendorf® tube, in order to minimize inconsistency in other parameters.

Samples were prepared by vortex mixing for 2 minutes and then sonicating for 15 minutes. They were spin casted after dropping two droplets of sample onto the wafer.

### **3.7 Broadly varying the concentration of $\gamma$ -Fe<sub>2</sub>O<sub>3</sub> nanoparticles redispersed in octane**

After the optimum spin casting programs were selected, the concentration of the samples redispersed in octane was varied. It was only during this time that the Benitez et al. method of ultrasonically cleaning the wafers in acetone and rinsing

with isopropanol was used. The table below summarizes the sample preparation for this experiment.

**Table 3:** Spin casting programs used for this experiment.

| Program | Program Settings  | Concentration (mg/ml) |
|---------|-------------------|-----------------------|
| Q       | 1000rpm for 1min  | 21.27                 |
| D       | 3000rpm for 30sec | 21.27                 |
| D       | 3000rpm for 30sec | 9.80                  |
| D       | 3000rpm for 30sec | 6.25                  |

The nanoparticle solution was dried on a hot plate at 80°C for 20 minutes.<sup>28</sup>

### 3.8 Slightly varying the concentration of $\gamma$ -Fe<sub>2</sub>O<sub>3</sub> nanoparticles redispersed in octane

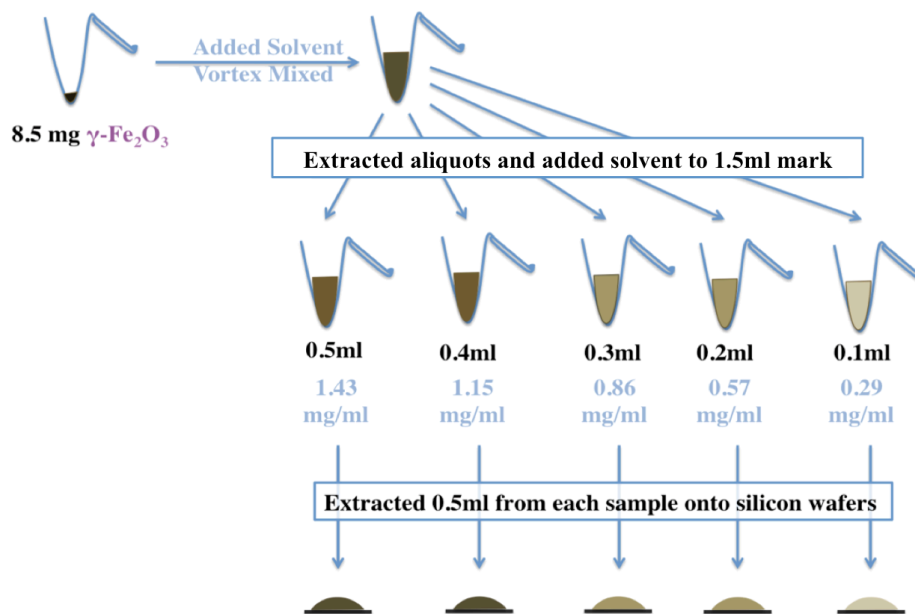


**Figure 21:** Method used to prepare diluted nanoparticle dispersions.

The solution was assumed to have a smooth consistency of nanoparticles after vortex mixing in the primary Eppendorf® tube for 15 minutes. The secondary Eppendorf® tubes were vortex mixed for 5 minutes after adding solvent to the 1.5ml mark, to ensure thorough mixing, Figure 21. After 0.5ml from each sample was deposited onto the wafers, the samples were spin casted using Program Q (1000rpm for 30 seconds), after which they were characterized with AFM.

### **3.9 Characterization with AFM**

The Veeco Innova Atomic Force Microscope was used to characterize nanoparticles deposited on silicon wafers. To probe the contours of all samples in this report, tapping mode was used. To tune the doped Si, rectangular, cantilever (Model Part: MPP-11123-10;  $f_c$ : 260-380kHz), a broad initial frequency range of 0 to 1000kHz, a drive amplitude value less than 1V, and an input gain of  $\times 4$  were used.

The tip ( $\sim 8\text{nm}$ - $12\text{nm}$  radius) was auto engaged into the sample in normal mode. A scan rate of 0.3000-0.5000 kHz was used. To obtain low-resolution images 128 sample lines and a scan range of  $20\mu\text{m} \times 20\mu\text{m}$  were used. Rough area analysis (to obtain the average height of particles) and line analysis (to obtain height difference calculations) were usually done with low-resolution images. To obtain medium-resolution images 256 sample lines and a scan range of  $10\mu\text{m} \times 10\mu\text{m}$  were used. To obtain high-resolution images 512 sample lines and a scan range of  $5\mu\text{m} \times 5\mu\text{m}$  were most commonly used.

In addition to roughness analysis, line measure was used to further analyze the topography of the sample with attempts to measure the spacing in between different nanoparticles close in proximity. Line measure was used to analyze the height of individual particles for histogram analysis. The Veeco Innova AFM Video Camera was used to take snap shots of each sample.

### **3.10 Characterization with UV-Vis**

The Cary 50 UV-Vis Spectrophotometer was used to confirm the presence of Iron (Fe) in the  $\gamma$ -Fe<sub>2</sub>O<sub>3</sub> nanoparticle dispersion. Since Iron contains non-bonding electrons, a peak at 330nm was expected.<sup>13</sup> A low concentration of solution was used. A medium scan rate was used for scanning the UV-Vis region.

### **3.11 Characterization with FTIR**

The Bruker-Alpha FTIR was used to confirm the presence of surfactants in the  $\gamma$ -Fe<sub>2</sub>O<sub>3</sub> nanoparticle solution. Since FTIR collects data in a wide spectral range, different peaks from 750cm<sup>-1</sup> to 4000cm<sup>-1</sup> were analyzed. These peaks included, but were not limited to, the C-H stretch in alkanes (3000cm<sup>-1</sup> -2850cm<sup>-1</sup>) and the C=O stretch in carboxylic acids (1760cm<sup>-1</sup> to 1690cm<sup>-1</sup>). To achieve more precise spectra, 32 scans were used.

### 3.12 Characterization with SEM

Previously prepared samples were examined with the FEI Magellan 400 Scanning Electron Microscope (2.00kV). The secondary electron detection mode was used to obtain information about the sample topography. From the images generated, the diameters of  $\gamma$ -Fe<sub>2</sub>O<sub>3</sub> nanoparticles and the spacing in between them were measured with Image J, an image-processing program.

## 4. RESULTS AND DISCUSSION

### 4.1 Identification of the $\gamma$ -Fe<sub>2</sub>O<sub>3</sub> Nanocrystallites Synthesized

The synthesis of  $\gamma$ -Fe<sub>2</sub>O<sub>3</sub> nanoparticles with octanoic acid surfactants produced a fairly substantial yield of particles. The resulting  $\gamma$ -Fe<sub>2</sub>O<sub>3</sub>-octanoic acid nanoparticles were powdery in appearance, not clumpy. They dispersed easily in hydrocarbon solvents.

To verify the presence of, and identify, the  $\gamma$ -Fe<sub>2</sub>O<sub>3</sub> nanocrystallites, AFM (Figure 22), UV-Vis Spectroscopy (Figure 24) and FT-IR Spectroscopy (Figure 25) were used.

#### 4.1.1. AFM Analysis

The AFM images show  $\gamma$ -Fe<sub>2</sub>O<sub>3</sub> nanoparticles deposited on silicon wafers by dropcasting from octane Figure 22 (a), and hexane Figure 22 (b), (c). Though no attention was paid to sample concentration, octane appears to be the better redispersing solvent: the particles in Figure 22 a) are more defined than those in b) and c). The two most frequently occurring nanoparticle sizes, as seen in Figure 22 for Octane are 4nm and 8nm. The AFM image not only shows that the concentration of nanoparticles was high for this sample, but also shows the formation of multilayers. Since the average size was calculated via a height analysis, it is highly possible that the larger particles are those at the top layer, and the smaller particle sizes correspond to those particles in another layer below.

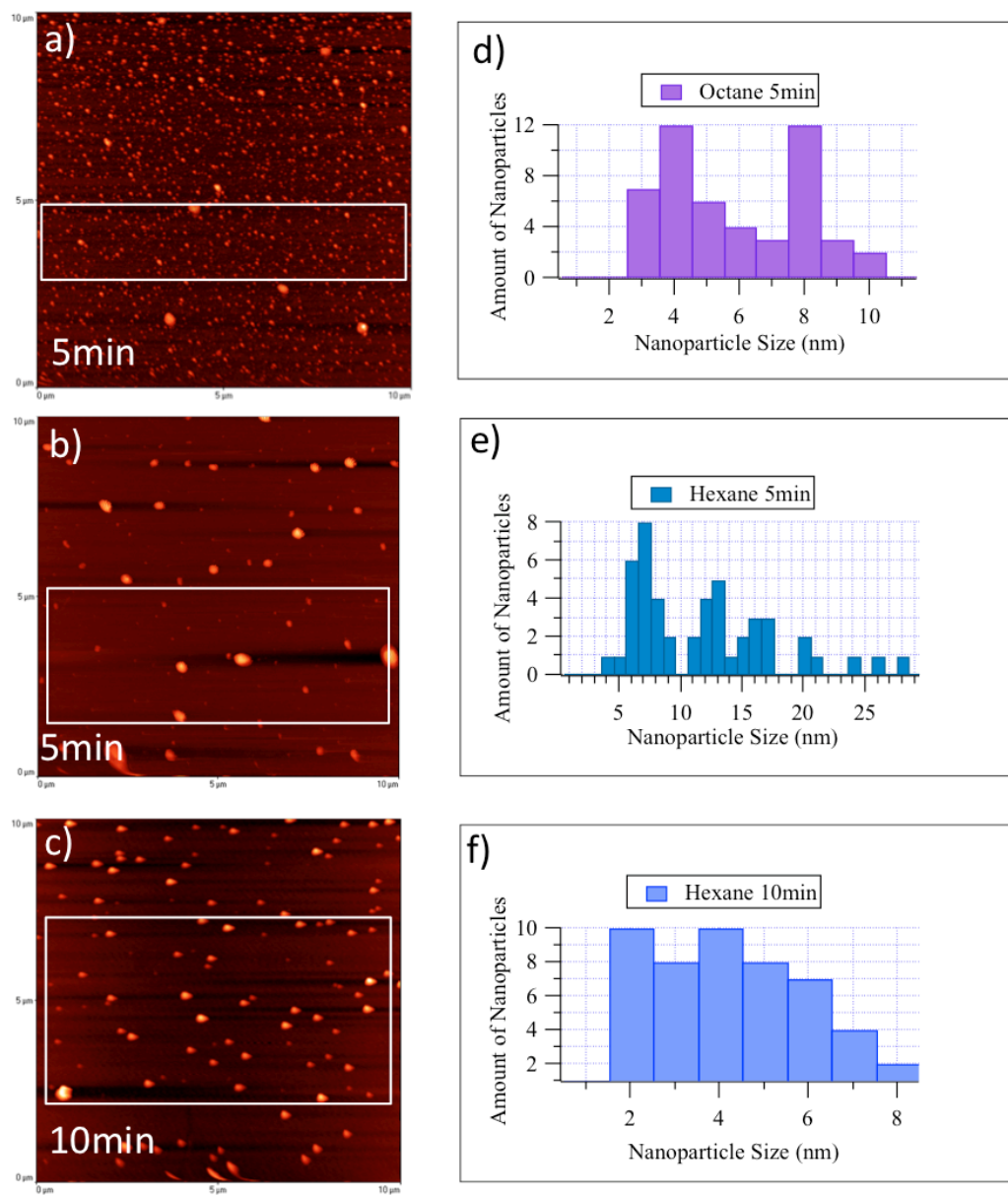
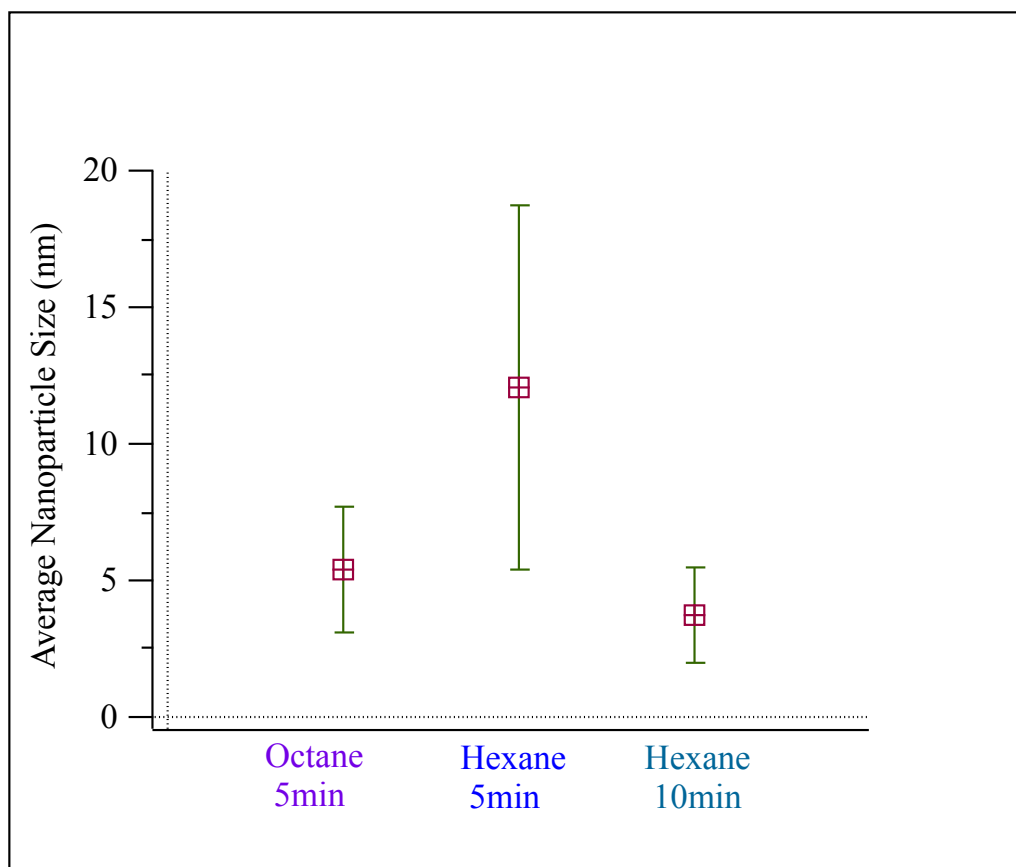


**Figure 22:** AFM images of  $\gamma$ -Fe<sub>2</sub>O<sub>3</sub> nanoparticles on silicon wafers, (a) dispersed in octane (b), (c) dispersed in hexane. Graphs d), e) and f) are the corresponding histograms: samples were vortex mixed for the time indicated.

**Table 4:** Average sizes calculated using Microsoft Excel from a sample set of 50 nanoparticles for each sample shown in Figure 22.

| <b>Sample</b> | <b>Average Size (nm)</b> |
|---------------|--------------------------|
| Octane 5min   | $5 \pm 2$                |
| Hexane 5min   | $12 \pm 7$               |
| Hexane 10min  | $4 \pm 2$                |

For the particles redispersed in hexane, the same is also possible, however considering that the concentration of the sample appears much lower than that of octane, it is more likely that the larger particles in Figure 22 b), are representative of aggregates. By increasing the agitation period, i.e. vortex mixing, for Hexane to 10 minutes, Figure 22 c), the prevalence of aggregates diminished, and sample became to be more monodisperse.



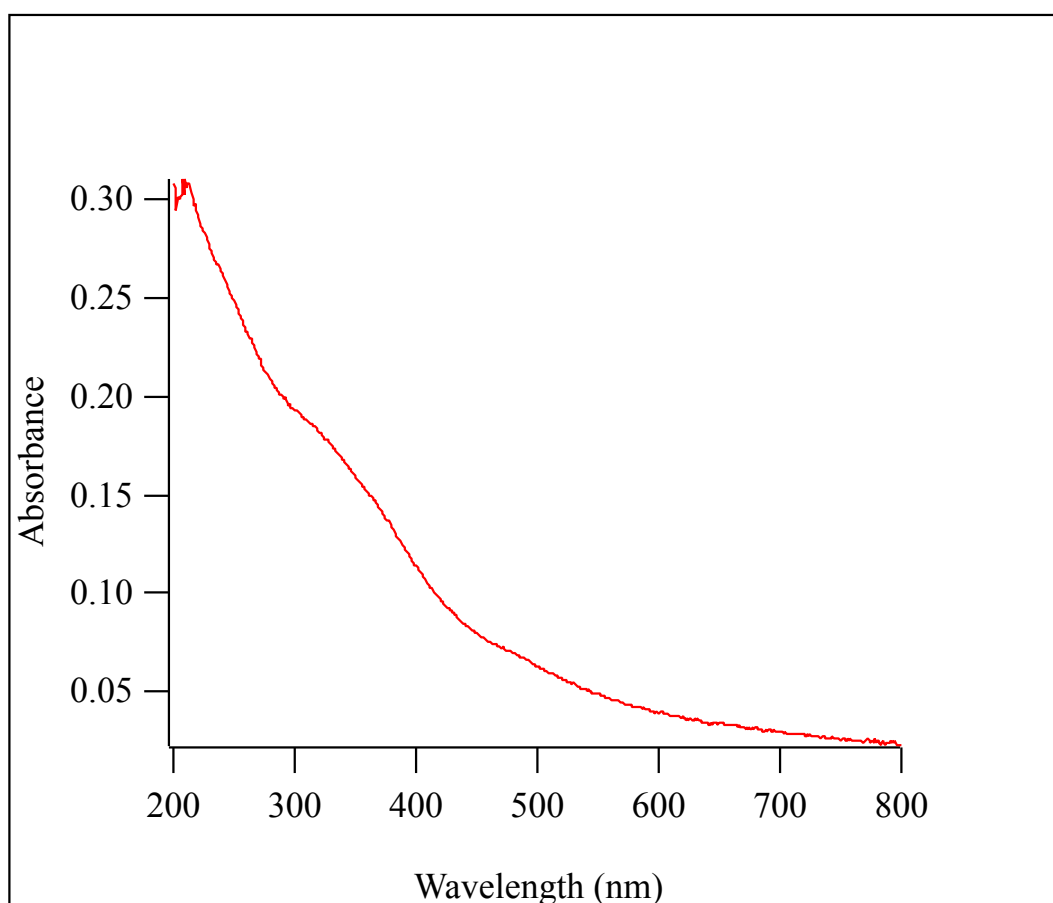
**Figure 23:** Effect of solvent and vortex mixing on the average size and monodispersity of nanoparticles. The average sizes and standard deviations were calculated using Microsoft Excel.

Figure 23 shows the average sizes corresponding to data in Figure 22 and Table 4.

The average sizes were calculated from a sample set of 50 nanoparticles from each image. As seen in the graph above, the average size and standard deviation of hexane decreased with extended vortex mixing. However, octane was able to provide favorable results in 5 minutes of vortex mixing, where as hexane provided similar results in 10 minutes of vortex mixing.

#### 4.1.2. UV-Vis Analysis

The UV-Vis spectroscopy data below shows a peak at  $\sim 330\text{nm}$ , similar to an intense peak that Hyeon et al. found at  $330\text{nm}$ .<sup>13</sup> This peak corresponded to a charge transfer process between  $\text{Fe}^{3+}$  and oleate. Also similar to their UV-Vis spectra, is the small shoulder at  $\sim 480\text{nm}$ . The observed results show that a similar charge transfer process between  $\text{Fe}^{3+}$  and octanoate occurs.



**Figure 24:** UV-Vis spectrum of  $\gamma\text{-Fe}_2\text{O}_3$  nanoparticles redispersed in Octane.

This evidence of the presence of iron aids in confirming  $\gamma$ -Fe<sub>2</sub>O<sub>3</sub> nanoparticles. For further confirmation, supporting evidence of the surfactant, octanoic acid, is essential. To confirm the presence of the fatty acid, Fourier Transform Infrared Spectroscopy was used, Figure 25.

#### 4.1.3. FT-IR Analysis

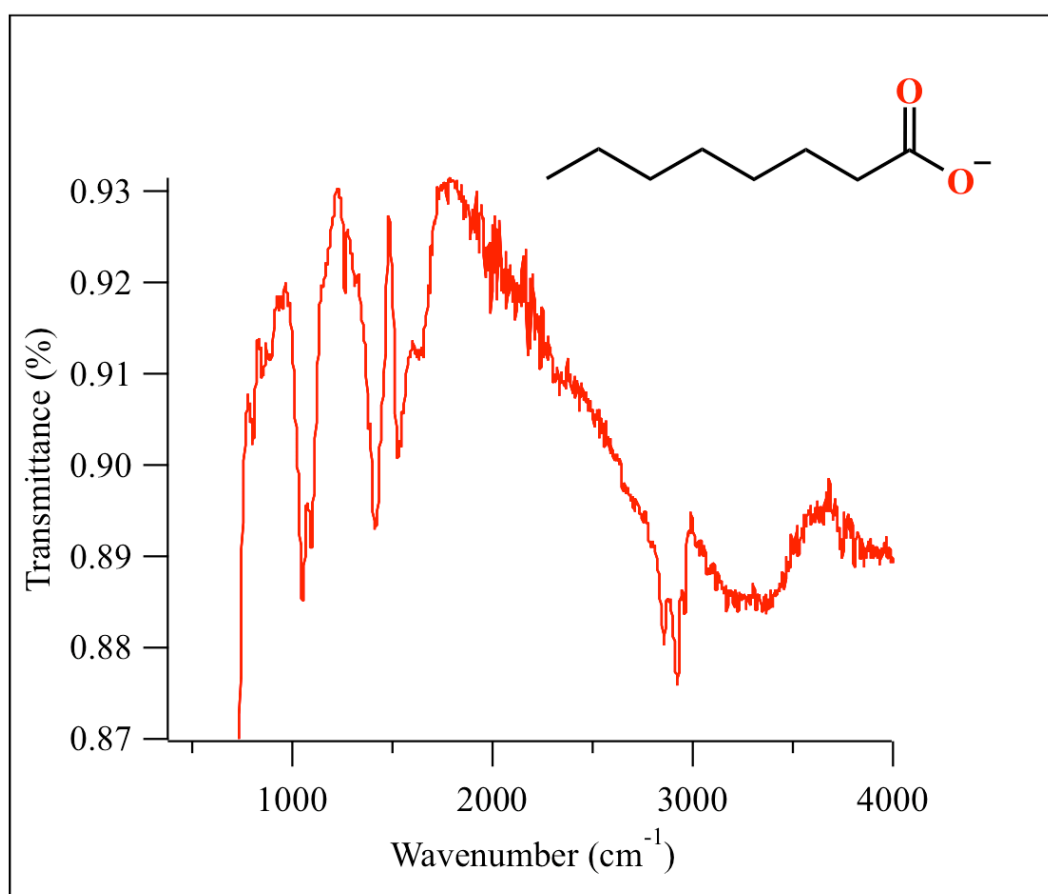


**Figure 25:** FT-IR spectrum of dried  $\gamma$ -Fe<sub>2</sub>O<sub>3</sub> nanoparticles at room temperature.

The fingerprint region in infrared spectroscopy contains numerous complex absorption peaks for intermolecular bending and vibrations that vary depending on the compound. That region lies below  $1500\text{cm}^{-1}$ . Beyond that region, is a peak at  $1615\text{cm}^{-1}$  which corresponds to a C=O stretch for iron carboxylate salts.<sup>29</sup> Iron carboxylate complexes should still be present, because the  $\gamma\text{-Fe}_2\text{O}_3$  nanoparticles should consist of an iron-octanoic acid core encapsulated by a  $\gamma\text{-Fe}_2\text{O}_3$  shell. In the spectra above, a  $1710\text{cm}^{-1}$  characteristic of the C=O stretch of saturated carboxylic acids is barely visible. Though it is likely that there is a peak that is either slightly shifted to the left or camouflaged by the  $1610\text{cm}^{-1}$ , the apparent absence of that peak suggests that virtually all the free octanoic acid was removed during the washing process. Overall, there is evidence that the carboxylate was strongly attached to the nanoparticle.<sup>11</sup> Peaks  $2853\text{cm}^{-1}$ ,  $2920\text{cm}^{-1}$  and  $2957\text{cm}^{-1}$  in the C-H bond region correspond to alkyl (methyl) groups in octanoic acid. Peak  $2853\text{cm}^{-1}$  corresponds to the  $\text{CH}_2$  symmetric stretch vibrations; peak  $2920\text{cm}^{-1}$  corresponds to the  $\text{CH}_2$  antisymmetric stretch vibrations; and peak  $2957\text{cm}^{-1}$  corresponds to the  $\text{CH}_3$  in-plane and out-of plane stretch vibrations.<sup>30</sup>

## **4.2 Investigating the effect of Agitation Methods on $\gamma\text{-Fe}_2\text{O}_3$ Nanoparticle**

### **Self-Assembly**

Two agitation methods, sonication and vortex mixing, were tested to identify the best way to produce particles with more favorable monodispersity and assembly. First, particles were redispersed in three different solvents: hexane,

octane and toluene. Then, the samples were sonicated in each solvent for 0, 5, 10, 15, 20 and 30 minutes. Vortex mixing was performed to agitate another batch of nanoparticles in solution. Similarly, particles were redispersed in three different solvents: hexane, octane and toluene. After which samples were vortex mixed in each solvent for 0, 2, 4, 6 and 8 minutes. . Vortex mixing had already proved to break down aggregates in a fairly short period of time, achieving fairly monodispersed particles. Shorter agitation periods were chosen for vortex mixing.

AFM Video Camera snapshots, AFM images, and the subsequent analysis of those data, allow an effective evaluation of these two methods. Multiple scans of the samples were done, and the data from all images were averaged to achieve data that represents the entire sample. It is expected that as the sonication period increases, the size of the aggregates should be further broken down resulting in smaller particles. This allows us to predict that agitation period is inversely proportional to the average size of the nanoparticles in the sample.

It is important to note that samples were drop casted onto the silicon wafer at low heat (~65-80°C) to rapidly evaporate the solvent.

### 4.2.1 Sonication

#### 4.2.1.1. Hexane

Figure 5 shows the AFM images of the nanoparticles deposited on the Si wafers after sonication for different time periods (0min, 5min, 10min, 15min, 20min, 30min). A noticeable trend was observed with regards to solvent evaporation in hexane.

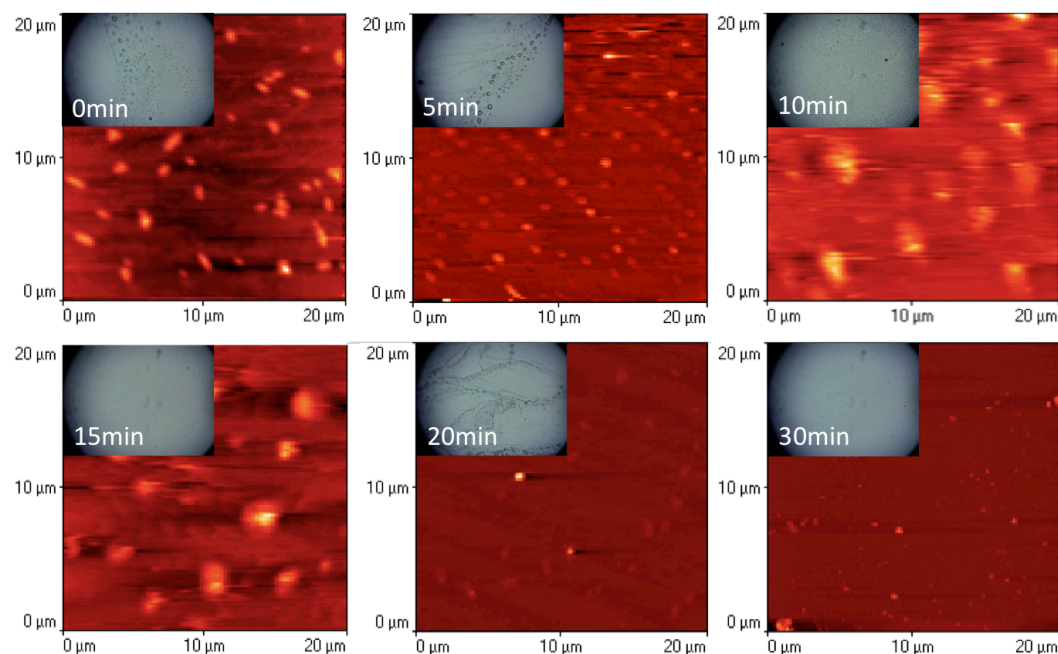


**Figure 26:** AFM images of samples containing  $\gamma\text{-Fe}_2\text{O}_3$  nanoparticles redispersed in hexane and their corresponding AFM Video Camera snapshots of the sample surface. All samples were sonicated for the time indicated.

Aggregates are observed in all samples and skewed the results of data analysis. Most of these aggregates could be some unidentified solvent residues.

These solvent residues are visible in video camera snap shots in figure inserts. Nanoparticles can be clearly visible only in the samples prepared by sonicating nanoparticles for 20 minutes and 30 minutes. Sharper edges observed in these images verify that these are individual nanoparticles, or small aggregates, and not solvent residues. In addition to breaking up nanoparticle aggregates, which was the intended use of this method, sonication can be used to break up large solvent residues into smaller droplets, especially at longer sonication times (30 min).

Figure 27 below shows the average size of particles for each sonication period. For the AFM analysis, the assumption has been made that the nanoparticles are roughly spherical in shape. This assumption allows us to consider the height of the particle found in the AFM images to be fairly representative of the particle's actual diameter. However, this assumption does not work for nanodroplets, not only because they are solvent droplets, but also because droplets of that size are easier to evaporate in the presence of heat. Hence in some cases, most likely in the first three samples, despite attempts to capture only images of nanoparticles, solvent residues and large solvent-nanoparticle aggregates were present.

The data does not have the expected decreasing trend in size. Also the large aggregates as portrayed in Figure 26 with shorter sonication periods, overall, appeared to have smaller sizes than most of the samples with the longer sonication periods. (Note: The solvent residue like aggregates, were excluded from the analysis.)

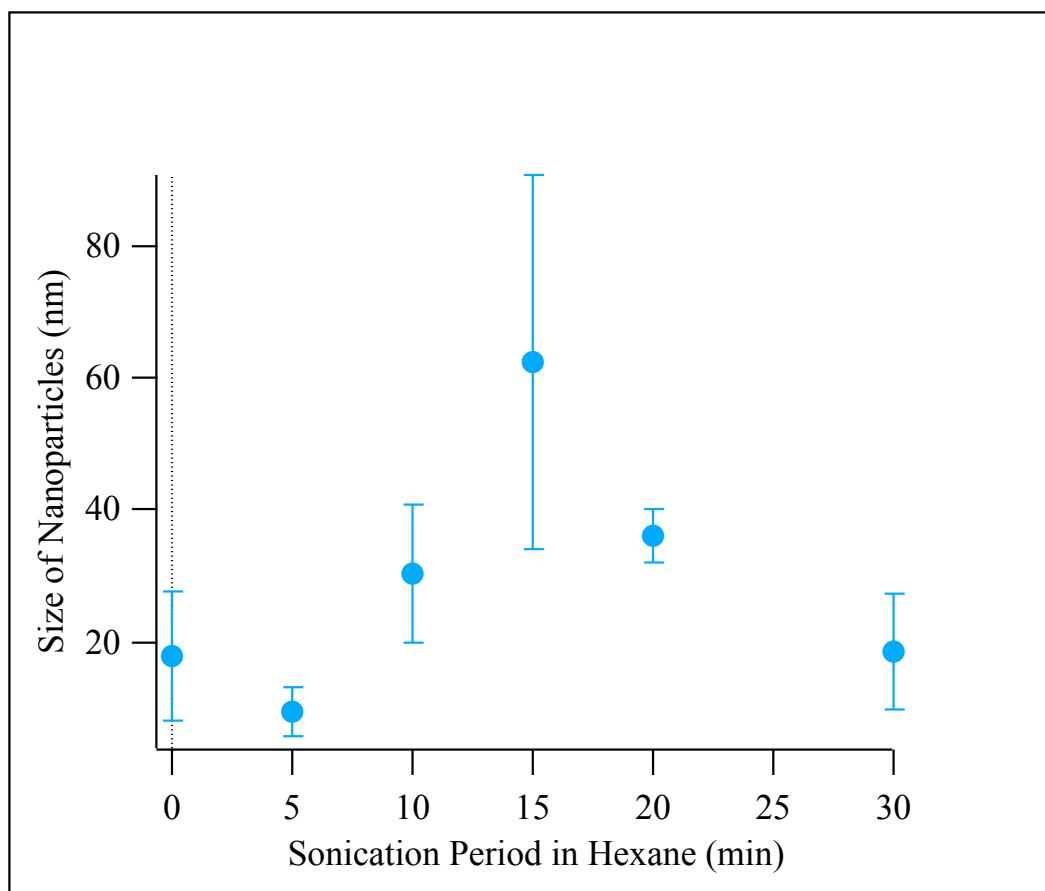


**Figure 27:** Effect of  $\gamma$ -Fe<sub>2</sub>O<sub>3</sub> nanoparticle size distribution as a function of sonication time. Hexane is used as the solvent to disperse nanoparticles.

It is important to note how this data matched up with the findings from the snapshots in the previous figure.

#### 4.2.1.2. Octane

As can be seen in the AFM video camera snapshots below, octane evaporated more efficiently, leaving no solvent residues. This observation questions the purity of the hexane solvent, which in theory has a much lower boiling point than octane. Sharp and concentrated nanoparticle rings were observed, as can be seen

in the snap shot of the 20-minute sample. Similar patterns were observed on all samples. This was expected since the solutions were drop casted onto wafers and allowed to evaporate quickly.

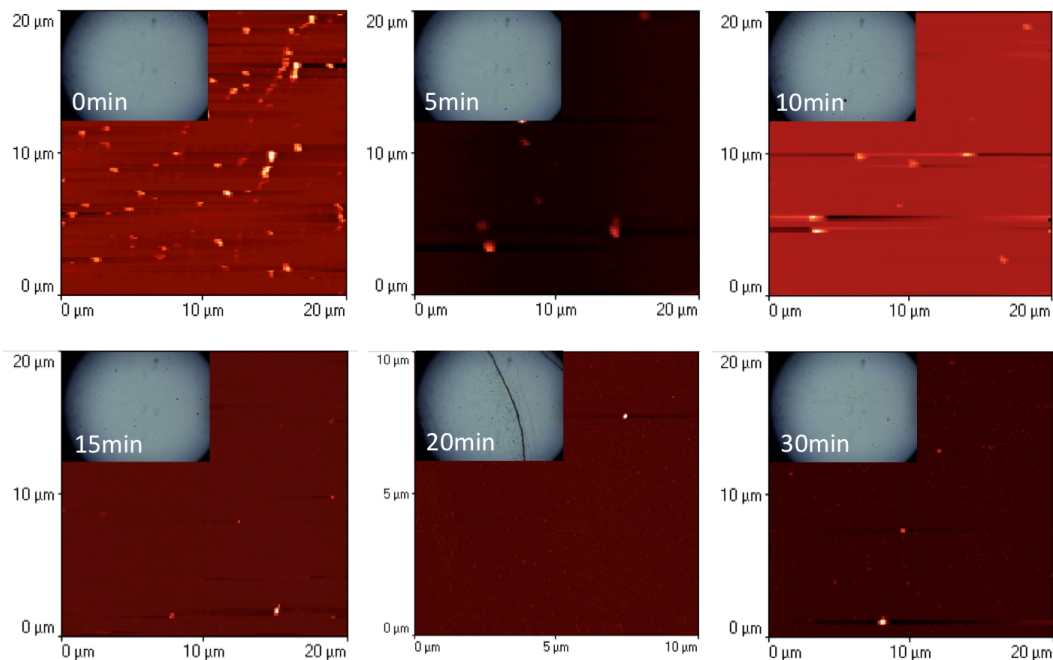


**Figure 28:** AFM images of samples containing  $\gamma\text{-Fe}_2\text{O}_3$  nanoparticles redispersed in octane and their corresponding AFM Video Camera snap shots of the sample surface. All samples were sonicated for the time indicated.

In the top three AFM images, representing the 0 and 10 minutes samples, the presence of aggregates skewed the contrast of the images and the data, making it difficult to study the smaller nanoparticles on the sample. Those aggregates appear to roughly decrease in size and quantity as the period of sonication is increased. In the bottom three images, representing the 15, 20 and 30 minutes samples, the presence of aggregates had diminished significantly, and though

barely visible in the images above, very tiny nanoparticles were seen on the images.

Figure 29 below shows the average size of particles for each sonication period in octane. The data clearly shows the expected decreasing trend. Larger aggregates present in 10-minute sample, dispersed between smaller particles that are difficult to see, broaden the variation within the sample. As expected, the 30-minute sample has the smallest and most monodisperse nanoparticles.

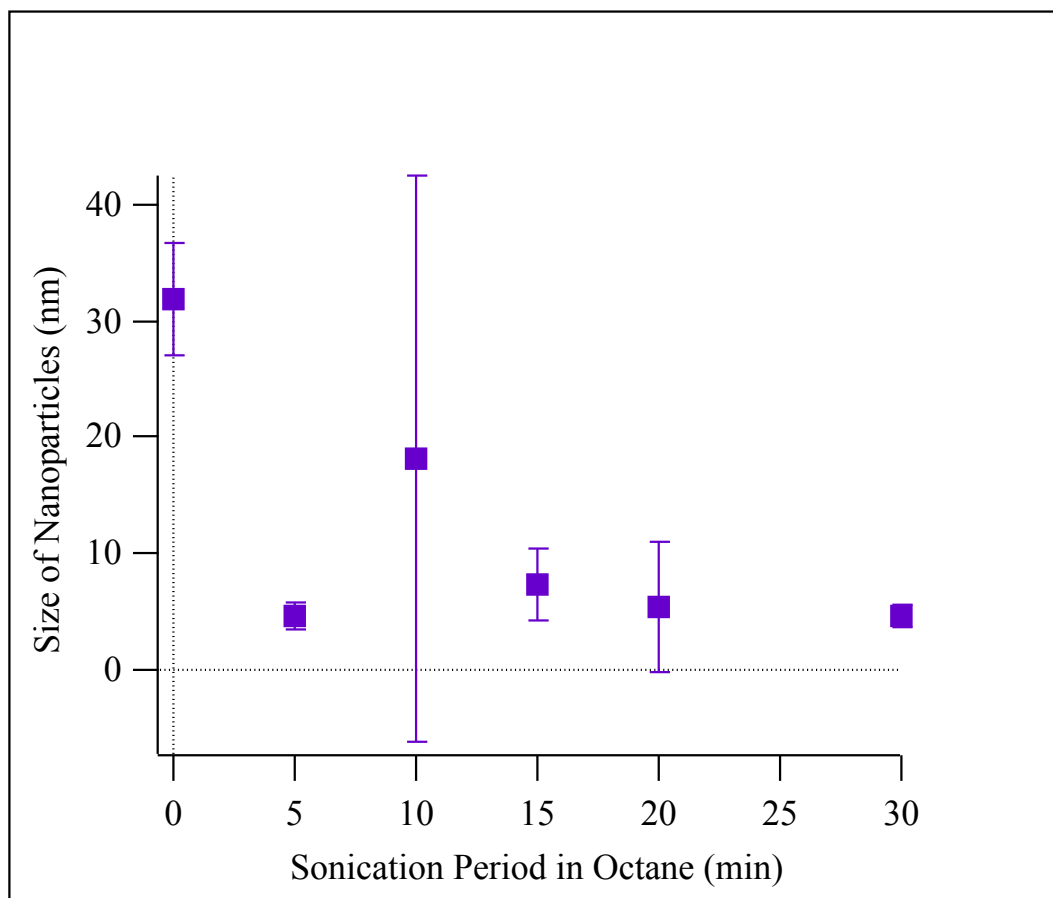


**Figure 29:** Effect of  $\gamma\text{-Fe}_2\text{O}_3$  nanoparticle size distribution as a function of sonication time. Octane is used as the solvent to disperse nanoparticles.

#### 4.2.1.3. Toluene

As can be seen in the AFM video camera snapshots below, toluene also evaporated more efficiently than hexane. In toluene, faint solvent rings were observed. The snapshot used for the 15-minutes sample is an example of the large dense patches of nanoparticles that can be seen on all samples for toluene. The dense patch was formed in areas where the toluene solvent evaporated last. The differences in observed ring formation is an indication of solvent evaporation dynamics.

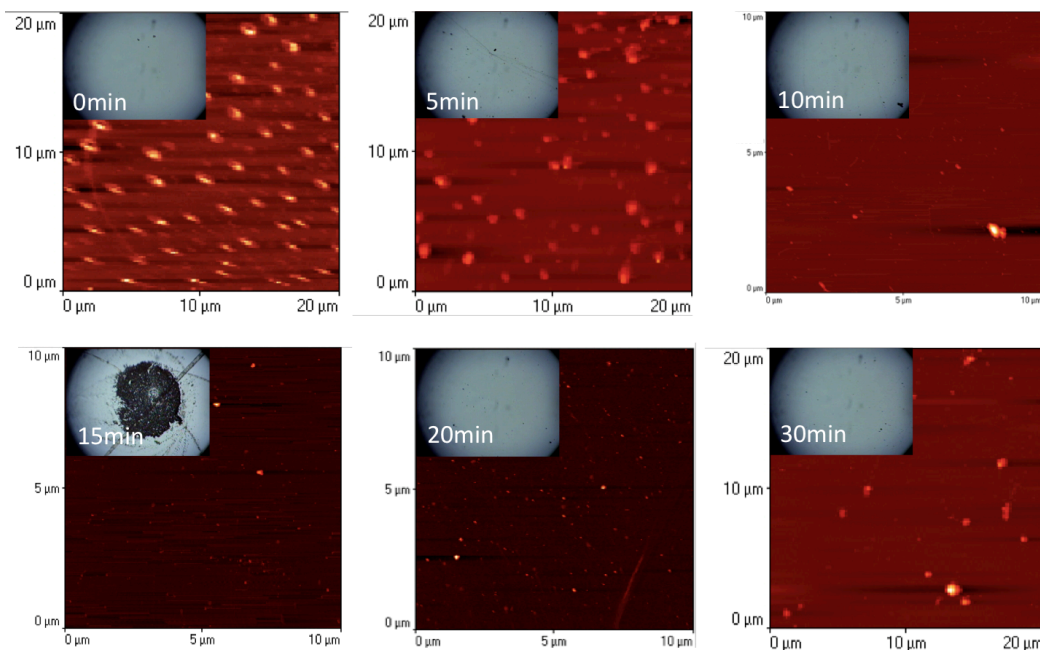


**Figure 30:** AFM images of samples containing  $\gamma\text{-Fe}_2\text{O}_3$  nanoparticles redispersed in toluene and their corresponding AFM Video Camera snapshots of the sample surface. All samples were sonicated for the time indicated.

In Figure 31 below, for the exception of the 0-minute and 30-minute samples, nanoparticle size decreases as the sonication time increases. The solvent droplets

found throughout the 0min toluene sample and the aggregates found throughout the 30min sample skew the data in a similar way as before. The solvent droplets contribute to an underestimation of average nanoparticle size in the sample. Aggregates on the other hand encourage the overestimation of the average particle size in the entire sample. In the 5min sample, both solvent residues and nanoparticles are apparent. From the 5min to the 20min sample, the solvent droplets and the sizes of nanoparticles diminish significantly. The plot below represents this comparison numerically.

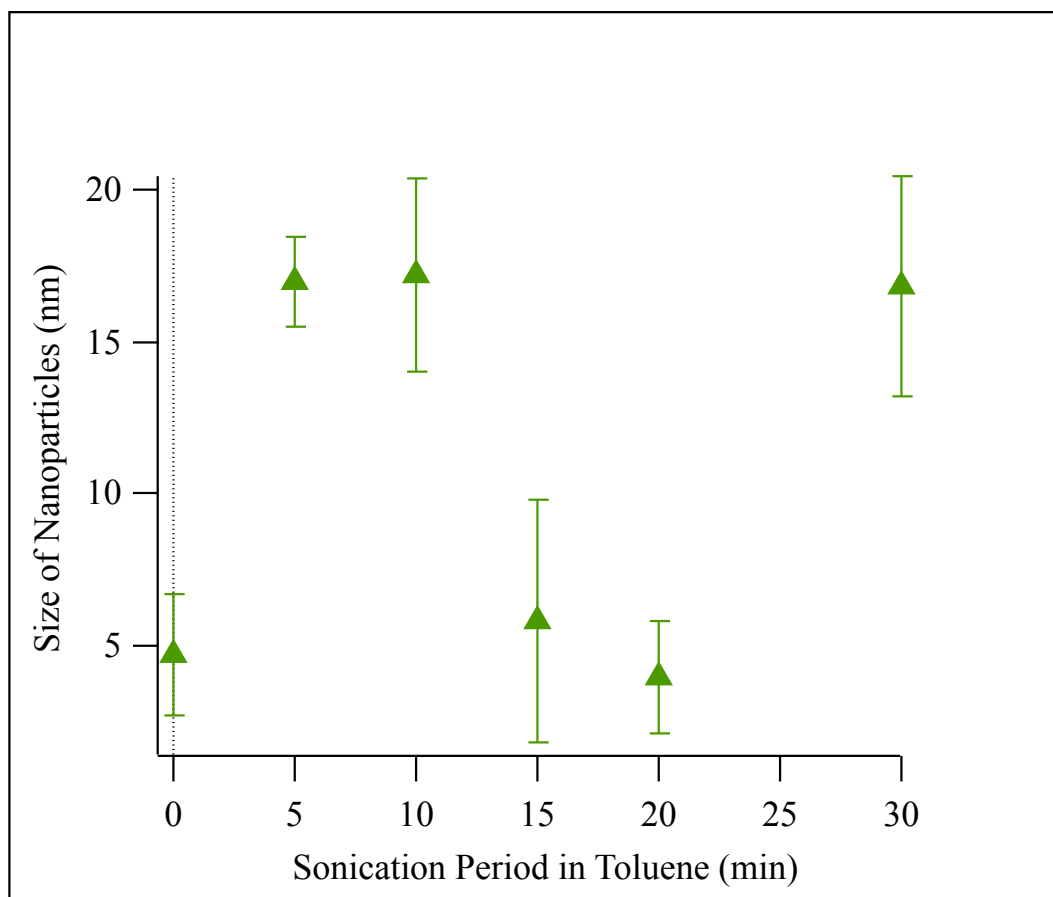


**Figure 31:** Effect of  $\gamma\text{-Fe}_2\text{O}_3$  nanoparticle size distribution as a function of sonication time. Toluene is used as the solvent to disperse nanoparticles.

#### 4.2.1.4. Compilation of Sonication Results: Hexane, Octane and Toluene

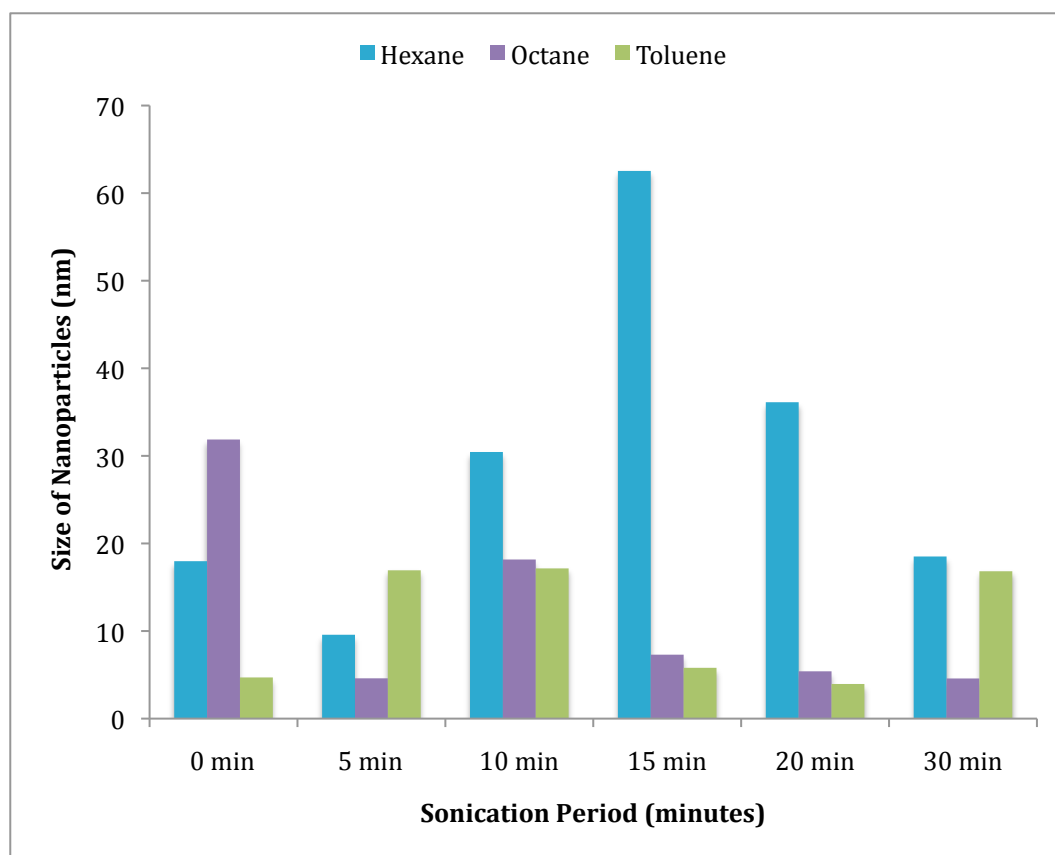
##### Comparison

Figure 11 below shows enlarged images of the AFM Video Camera snapshots under discussion. In the first image, the dried solvent residues after extended sonication time in hexane can be observed; the sharp and concentrated nanoparticle rings for octane can be observed in the second image; and the large dense patch of nanoparticles for toluene can be seen more clearly in the third image. This summarizes the variation in solvent evaporation dynamics and how it affects nanoparticle assembly under heat treatment.



**Figure 32:** Representation of characteristic features of samples drop casted for hexane, octane and toluene.

The bar chart (Figure 33) and the Table 5 below represent the relationship between sonication period and the average size of nanoparticles for all three solvents.



**Figure 33:** A compiled chart showing the effects of all three redispersing solvents and sonication on the average sizes of nanoparticles.

**Table 5:** A compilation of average sizes for all three redispersing solvents as they relate to sonication period.

| Sonication Period<br>(minutes) | Average Size of Nanoparticles (nm) |         |         |
|--------------------------------|------------------------------------|---------|---------|
|                                | Hexane                             | Octane  | Toluene |
| <b>0</b>                       | 18 ± 10                            | 32 ± 5  | 5 ± 2   |
| <b>5</b>                       | 10 ± 4                             | 5 ± 1   | 17 ± 2  |
| <b>10</b>                      | 30 ± 10                            | 18 ± 20 | 17 ± 3  |
| <b>15</b>                      | 63 ± 30                            | 7 ± 3   | 6 ± 4   |
| <b>20</b>                      | 36 ± 4                             | 5 ± 6   | 4 ± 2   |
| <b>30</b>                      | 19 ± 9                             | 5 ± 1   | 17 ± 4  |

As can be seen in both the figure and the table above, samples where hexane was used to redisperse particles generally had larger average particle sizes and the most polydispersity, followed by octane and then toluene. Octane shows the most consistent decrease in nanoparticle size and monodispersity with increased agitation. Octane also provides solvent residue free deposition of nanoparticles.

#### *4.2.2. Vortex Mixing*

Figures 13-17 show images of nanoparticles drop casted onto a heated silicon wafer after vortex mixing.

##### 4.2.2.1. Hexane (2.0 mg/ml)

The AFM Video camera snapshots below show that solvent residue lines formed when hexane evaporated. With the instrument mostly registering the aggregates and only a few nanoparticles, the results showed huge polydispersity. It clearly shows that solvent residues and other impurities were present on the wafer. The “blank” sample was used as a control by drop casting only the solvents.

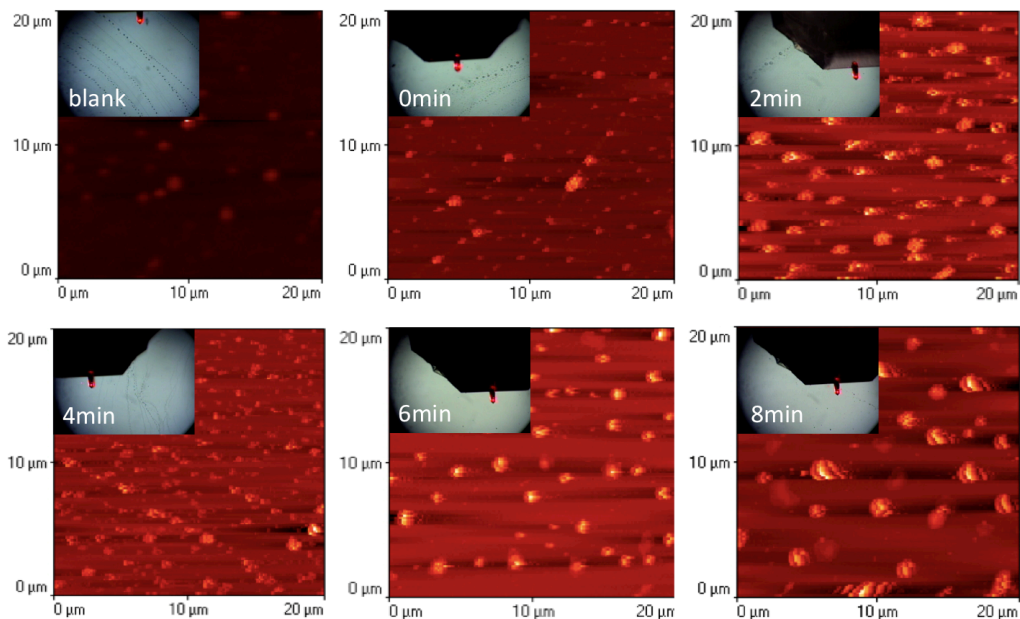


**Figure 34:** AFM images of samples containing  $\gamma\text{-Fe}_2\text{O}_3$  nanoparticles redispersed in hexane and vortex mixed for the time indicated, along with their corresponding AFM Video Camera snap shots of the sample surface.

In the plot (Figure 35) below, it is evident that the presence of solvent droplets and large aggregates are the cause for inconsistent data for the samples dropcasted for hexane. The results do not follow the trend expected, where particle size should continue to decrease with prolonged agitation. The first two samples have the most polydispersity.

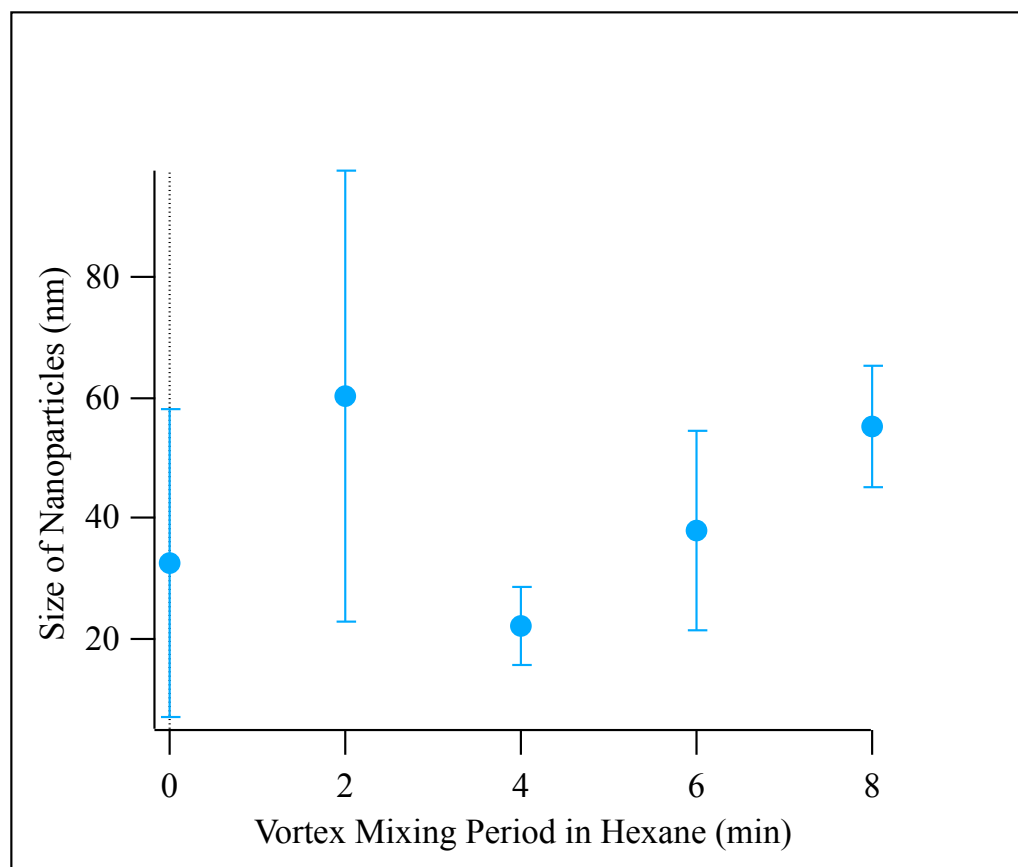


**Figure 35:** Effect of  $\gamma\text{-Fe}_2\text{O}_3$  nanoparticle size distribution as a function of vortex mixing time. Hexane is used as the solvent to disperse nanoparticles.

#### 4.2.2.2. Octane (2.5 mg/ml)

It is evident from the AFM images (Figure 36) below, that solvent residues and aggregates were also present in octane, but not as much as hexane. Images get cleaner and solvent residue-free, as vortex mixing increases.

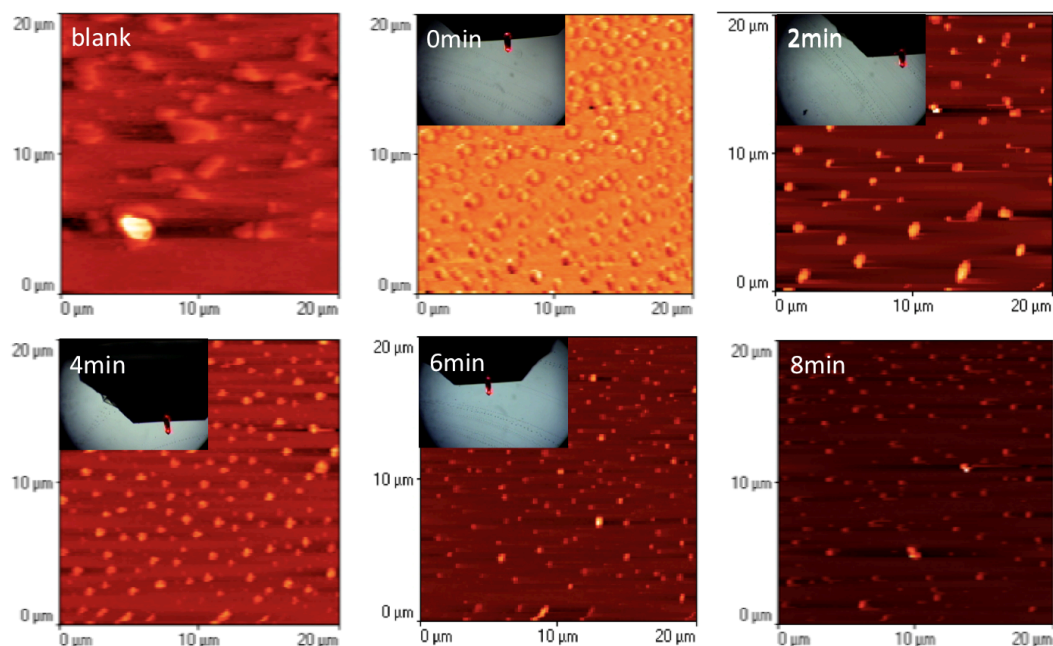


**Figure 36:** AFM images of samples containing  $\gamma\text{-Fe}_2\text{O}_3$  nanoparticles redispersed in octane and vortex mixed for the time indicated, along with their corresponding AFM Video Camera snap shots of the sample surface.

The plot below, Figure 37, shows nanoparticle size as a function of vortex mixing period. Interestingly, the average size of the nanoparticles decreases steadily with vortex-mixing period. The samples, however, were not monodisperse.

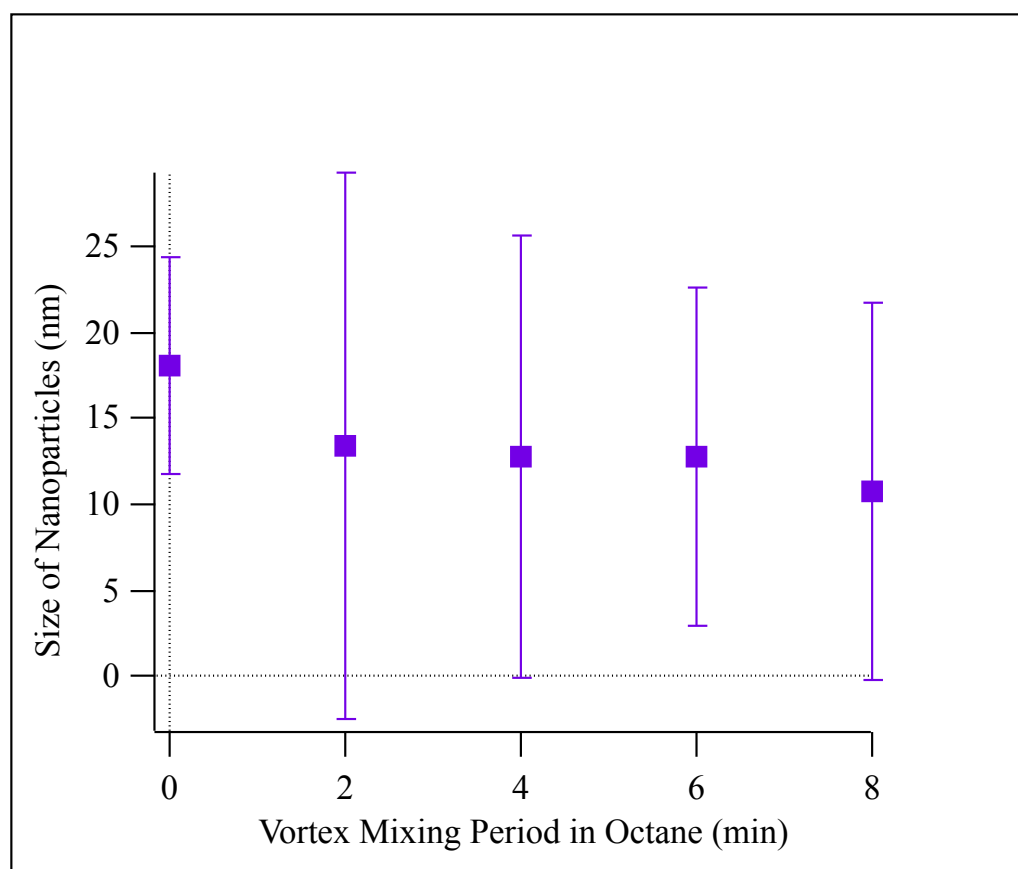


**Figure 37:** Effect of  $\gamma\text{-Fe}_2\text{O}_3$  nanoparticle size distribution as a function of vortex mixing time. Octane is used as the solvent to disperse nanoparticles.

#### 4.2.2.3. Toluene (3.3 mg/ml)

AFM images in Figure 18 show that almost all the samples are solvent residue- and aggregate-free. The height analysis shows a gradual decrease in size with increased agitation. The samples, however, like those redispersed in hexane and octane, appear polydisperse at lower vortex mixing periods.

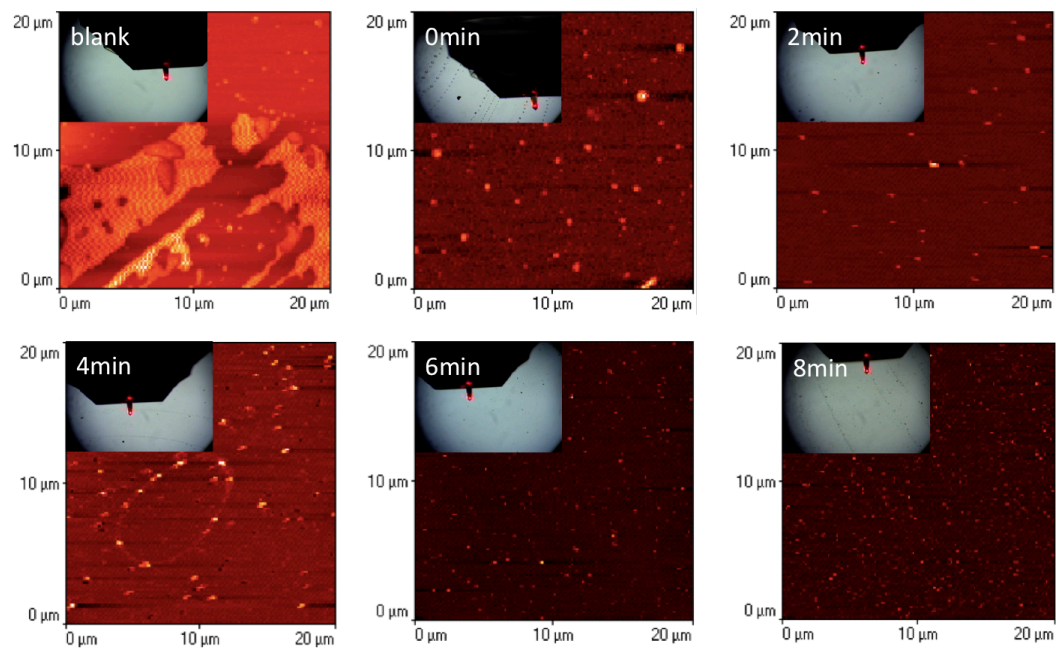


**Figure 38:** AFM images of samples containing  $\gamma\text{-Fe}_2\text{O}_3$  nanoparticles redispersed in toluene and vortex mixed for the time indicated, along with their corresponding AFM Video Camera snap shots of the sample surface.

Figure 39 below shows the corresponding height analysis results for the nanoparticles redispersed in toluene. Generally, particles seem to become more monodisperse as they break up into smaller particles. The results suggest that nanoparticles redispersed in toluene provide better separation of nanoparticles from their aggregates at higher vortex mixing periods.

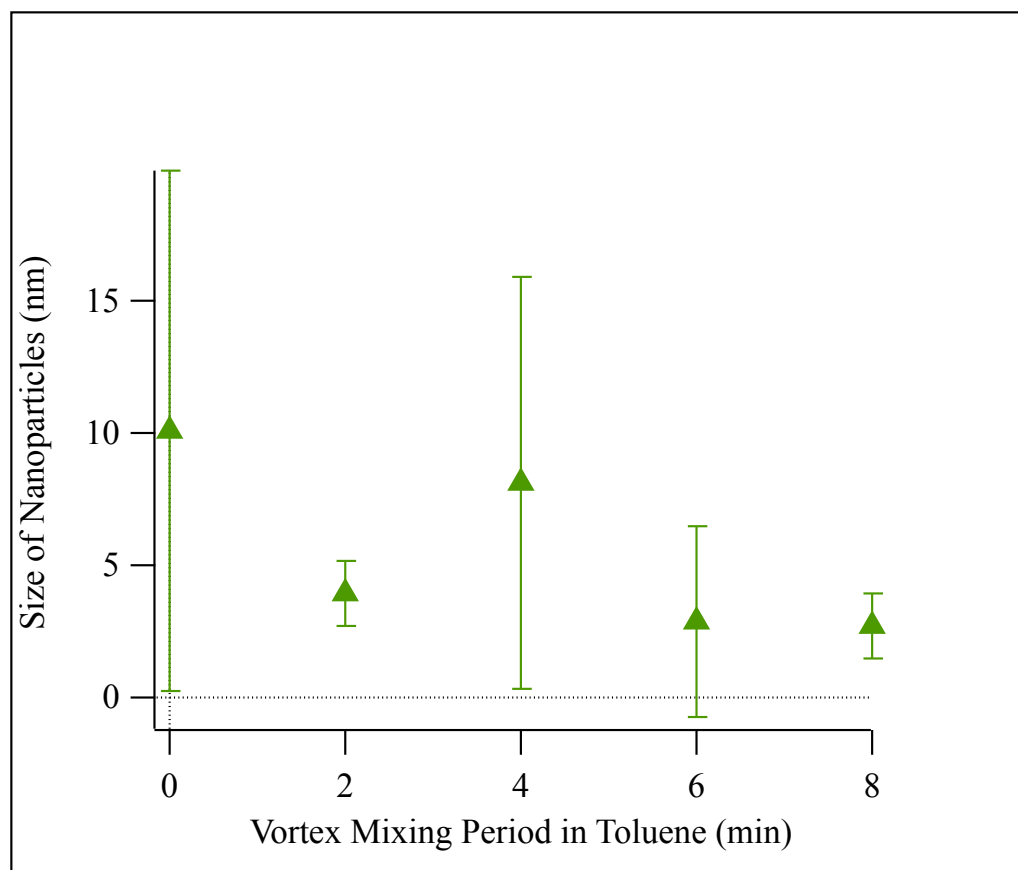


**Figure 39:** Effect of  $\gamma\text{-Fe}_2\text{O}_3$  nanoparticle size distribution as a function of vortex mixing time. Toluene is used as the solvent to disperse nanoparticles.

#### 4.2.2.4. Compilation of Sonication Results: Hexane, Octane and Toluene

##### Comparison

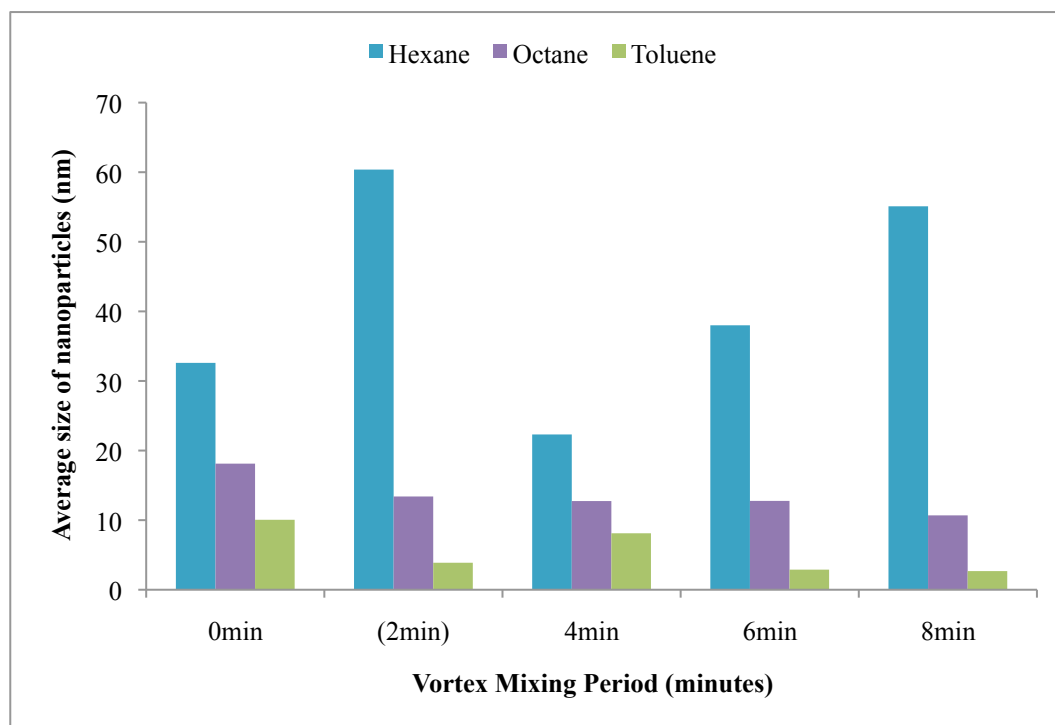


**Figure 40:** A compiled chart showing the effects of all three redispersing solvents and vortex mixing on the average sizes of nanoparticles.

**Table 6:** A compilation of average sizes for all three redispersing solvents as they relate to vortex mixing period.

| Vortex Mixing Period (minutes) | Average Size of Nanoparticles (nm) |         |         |
|--------------------------------|------------------------------------|---------|---------|
|                                | Hexane                             | Octane  | Toluene |
| 0                              | 33 ± 30                            | 18 ± 6  | 10 ± 10 |
| 2                              | 60 ± 40                            | 13 ± 16 | 4 ± 1   |
| 4                              | 22 ± 7                             | 13 ± 13 | 8 ± 8   |
| 6                              | 38 ± 17                            | 13 ± 10 | 3 ± 4   |
| 8                              | 55 ± 10                            | 11 ± 11 | 3 ± 1   |

As can be seen in both the bar chart and table above (Figure 40 and Table 6), samples for which hexane was used to redisperse particles generally had larger average particle sizes and the most polydispersity, followed by octane and then toluene. Octane shows the most consistent decrease in nanoparticle size with increased agitation, followed by toluene. Toluene had the most monodisperse particles, followed by octane.

Due to the overwhelming amount of aggregates and apparent solvent residues found on the wafer, alternate ways of silicon wafer cleaning and casting nanoparticles were investigated. Removing most aggregates and solvent droplets was expected to increase the monodispersity of the sample. It was expected that by removing the larger particles, the smaller particles remaining, most likely individual nanoparticles, would be fairly close in size.

Improving the procedures of cleaning wafers would remove any impurities that might interrupt particle assembly. On the other hand, spin casting was expected to spatially orient nanoparticles on the silicon wafer based on size; at fairly low concentrations the centrifugal force was expected to push larger particles outward from the center.

One practical reason to use vortex mixing is that the time consumption is less for vortex mixing. On the other hand, vortex mixed samples appeared to have more favorable results, in terms of particles size and distribution, than those sonicated. However, further experimentation with casting and cleaning silicon wafers needs to be done before coming to such a conclusion.

### 4.3 Results from Ultrasonically Cleaning the Silicon Wafers

Originally wafers were cleaned with distilled water, dried with compressed air and placed in a dessicator to dry. A more effective way of cleaning was needed. Benitez et al.<sup>28</sup> explains that ultrasonically cleaning them in acetone for 15 minutes, rinsing them with isopropanol, and then drying them with a pure stream of nitrogen gas cleans silicon wafers.

However, after ultrasonically cleaning the wafers in acetone, significant damage to the wafers was observed. In addition, the surface of the silicon wafer was completely covered with tiny broken pieces of silicon, Figure 41 a).

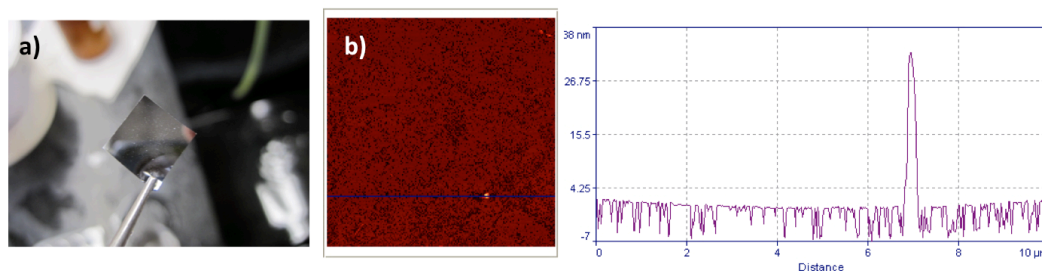


**Figure 41:** Results after attempting the method of ultrasonically cleaning the wafers, as used by Benitez et al. a) Appearance of Si wafer immediately after the ultrasonically cleaning in acetone, b) AFM Height image of a section of one of the samples.

From the two-dimensional plot on the right, only one particle appears to be present, that has a height of ~30nm. The plot also shows the holes in the wafer that surrounded that particle. This was seen frequently on samples cleaned by using that method. It was concluded that the ultrasonic cleaning damaged the wafers and that the solvent used may have contained impurities.

#### **4.4 Results from the Experimentation with Spin casting Settings in Different Solvents**

In an attempt to achieve more monodisperse nanoparticles and favorable assembly, the method of spin casting was used. Particles redispersed in octane and toluene were spin casted at various speed settings: 500rpm, 750rpm, 1000rpm, 2000rpm and 3000rpm for at least 30 seconds.

Since the centrifugal force is directly proportional to the mass of the particles according to the Equation 1 ( $F = M\omega^2r$ ), heavier particles are expected to move further away from the center of the silicon wafer during spin casting samples of low concentrations. Hence, the average size of the nanoparticles remaining in the center of the silicon wafer is expected to decrease as the angular speed increases. For these samples, only areas of the wafer close to its center were scanned and characterized with AFM.

As a trial, samples were agitated by vortex mixing for 2 minutes and then sonicating them for 15 minutes. An extended period of agitation was expected to break up aggregates in each solvent.

##### **4.4.1. Octane (1.9 mg/ml)**

As the speed increased, the average size of nanoparticles close to the center of the wafer decreased exponentially (Figure 42). As, predicted by the theory, Program

B resulted in the most aggregates, while Program D resulted in individual nanoparticles with smallest size closer to the center of the silicon wafer.

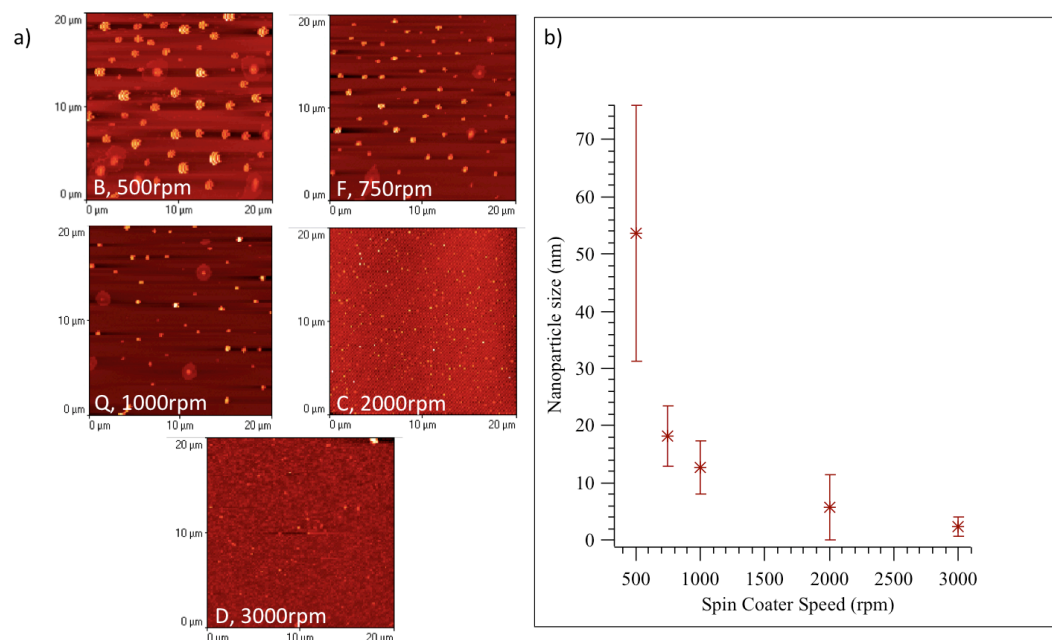


**Figure 42:** Spin casted samples: a) AFM images of samples containing  $\gamma\text{-Fe}_2\text{O}_3$  nanoparticles redispersed in octane and vortex mixed for 2 minutes and sonicated for 15 minutes, b) A plot of Spin Caster speed (rpm) vs. Average sizes of nanoparticles for each sample.

#### 4.4.2. Toluene (1.6 mg/ml)

A similar observation was made for toluene, Figure 43. An exponential decrease in the average size of nanoparticles correlated to an increase in spin casting speed.

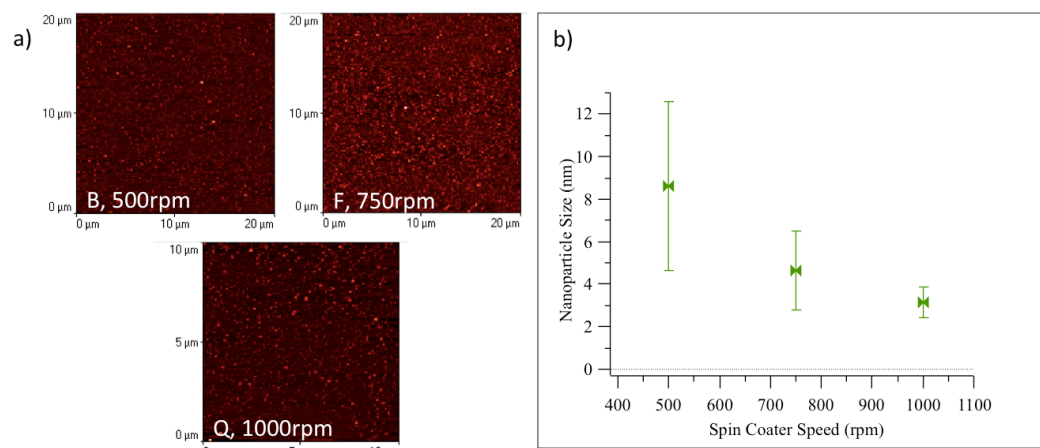


**Figure 43:** Spin casted samples: a) AFM images of samples containing  $\gamma\text{-Fe}_2\text{O}_3$  nanoparticles redispersed in toluene and vortex mixed for 2 minutes and sonicated for 15 minutes, b) A plot of Spin Coater speed (rpm) vs. Average sizes of nanoparticles for each sample.

This exponential decrease can be explained using Equation 1. Since the centrifugal force is directly proportional to the angular speed squared, varying the angular speed will affect the force exponentially. Hence with an exponential increase of the centrifugal force, there should be an exponential decrease in the size of the particles being pushed out from the center of the wafer. This explains the exponential decrease for both plots.

**Table 7:** Spin casted samples: tabulated compilation of spin casted samples for particles redispersed in octane and toluene.

| Spin Coater Program / Speed (rpm) | Average Size of Nanoparticles (nm) |               |
|-----------------------------------|------------------------------------|---------------|
|                                   | Octane                             | Toluene       |
| Program B / 500rpm                | $54 \pm 20$                        | $9 \pm 4$     |
| Program F / 750rpm                | $18 \pm 5$                         | $5 \pm 2$     |
| Program Q / 1000rpm               | $13 \pm 5$                         | $3.1 \pm 0.7$ |
| Program C / 2000rpm               | $6 \pm 6$                          | -.--          |
| Program D / 3000rpm               | $2 \pm 2$                          | -.--          |

Though both results show similar trends, nanoparticles spin casted from toluene resulted in smaller particles at the center than those prepared by spin casting from octane. Spin casting can also be used to manipulate the amount of sample present on the wafer. Program Q seemed to work best for both solvents.

All experiments thus far have been carried out with constant concentration values. While keeping the concentration constant, most effective sonication periods, vortex mixing periods and spin casting settings were evaluated.

However, concentration too influences the assembly of  $\gamma\text{-Fe}_2\text{O}_3$  nanoparticles. In the following two experiments, the concentration was varied: first very 'broadly' and then very 'slightly'.

#### **4.5 Results from Broadly Varying the Concentration of $\gamma\text{-Fe}_2\text{O}_3$**

##### **Nanoparticles Redispersed in Octane**

The concentration of nanoparticles in octane was varied on a wide scale, Figure 44.

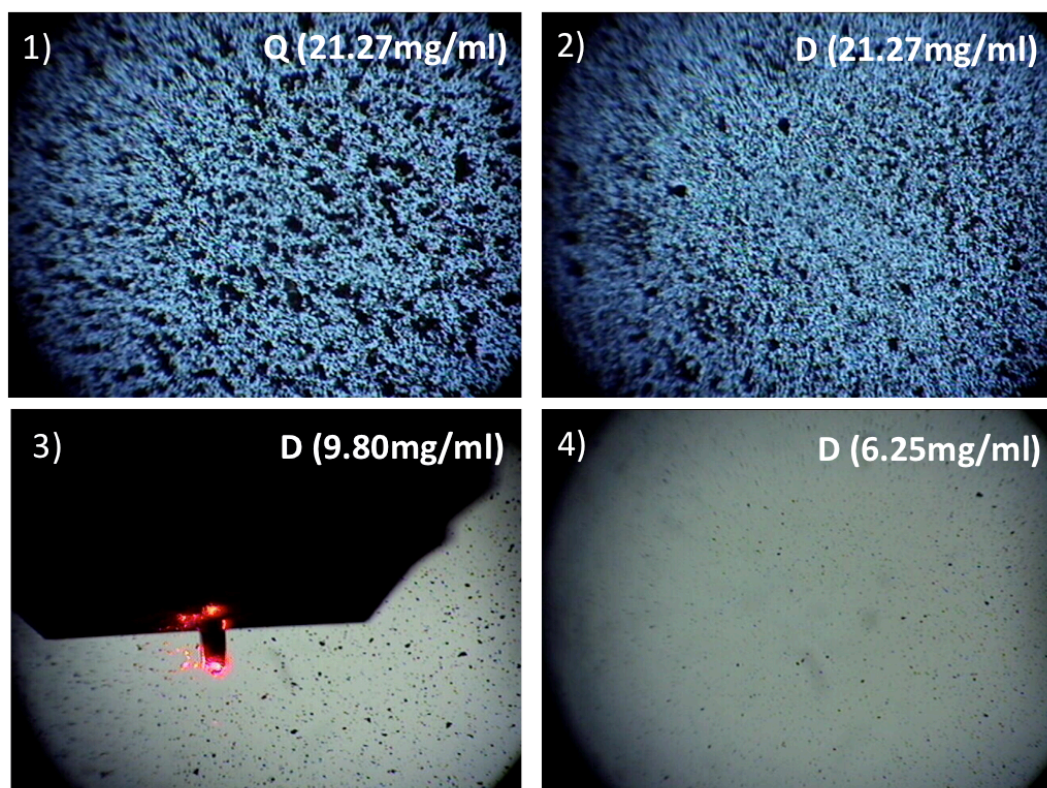


**Figure 44:** AFM video camera snap shots of  $\gamma$ -Fe<sub>2</sub>O<sub>3</sub> nanoparticles redispersed in octane at various initial concentrations as indicated. The AFM cantilever was present in snap shot 3, only. The letters Q and D represent the program used.

The first 2 samples show large aggregates throughout the silicon wafer. Analysis was not performed on these two samples, as the surface roughness was too high. The 4<sup>th</sup> sample, with 6.25mg/ml initial concentration, gave the most favorable assembly of nanoparticles as shown in Figure 45 below.

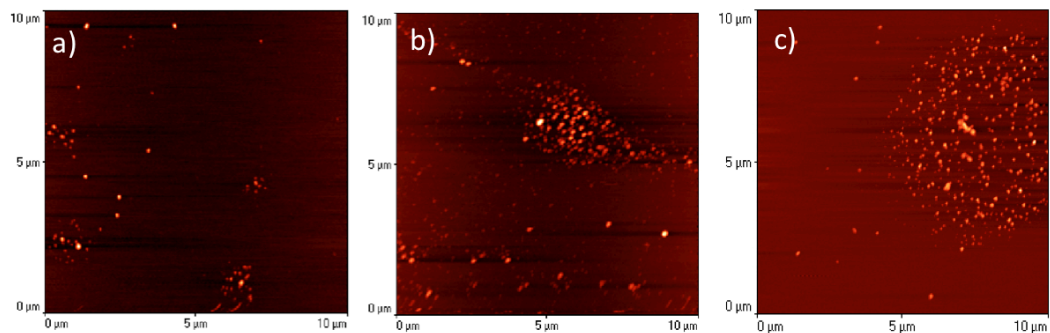


**Figure 45:** AFM Images of sample 4, prepared at low concentrations, and spin casted at 3000rpm for 30 seconds. The AFM images are  $10\mu\text{m}\times 10\mu\text{m}$  in size.

In the figure above, patches of nanoparticles are noticeable. Careful observation shows the presence of multilayers in Figure 45 b). Particles are fairly close together and appear monodisperse.

The following figures (46-48) are a series of histograms generated by performing the height analysis of the images above.

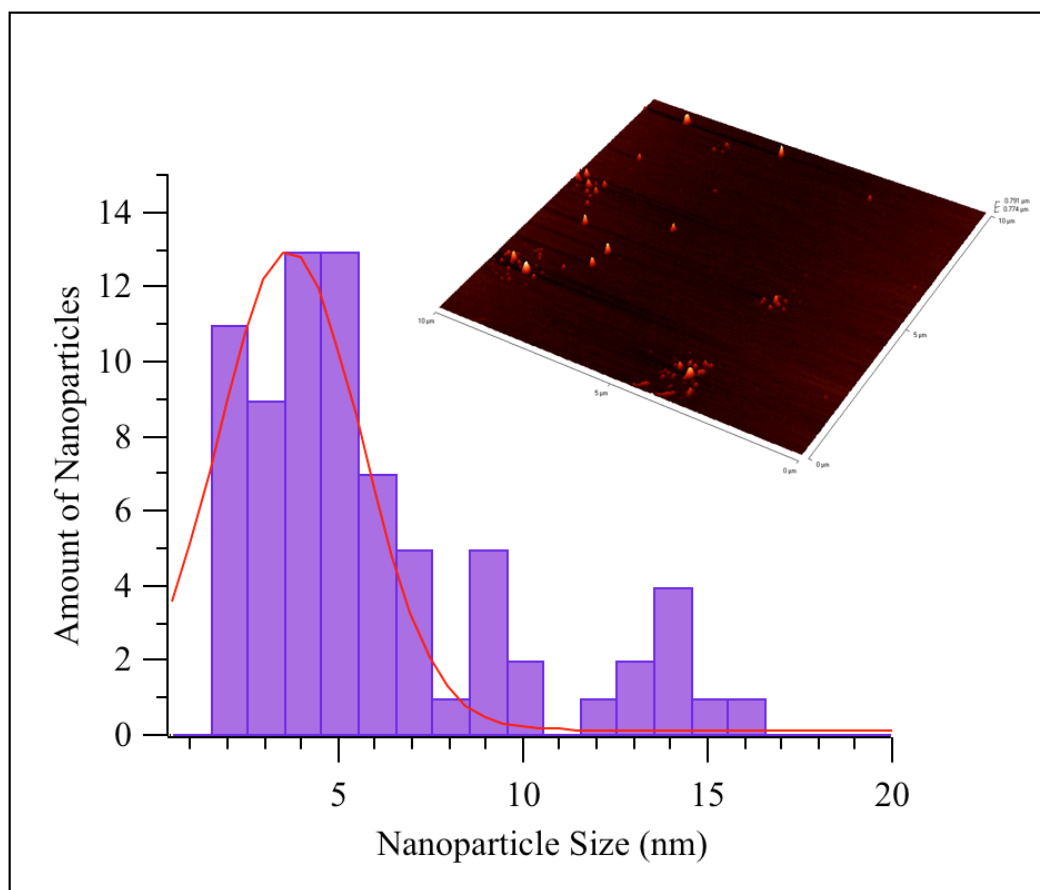


**Figure 46:** A histogram of the AFM image in Figure 24 c). It is fitted with a Gaussian curve. The most frequently occurring average nanoparticle size (mode) is  $4 \pm 1$  nm. The average nanoparticle size is  $5 \pm 4$  nm.

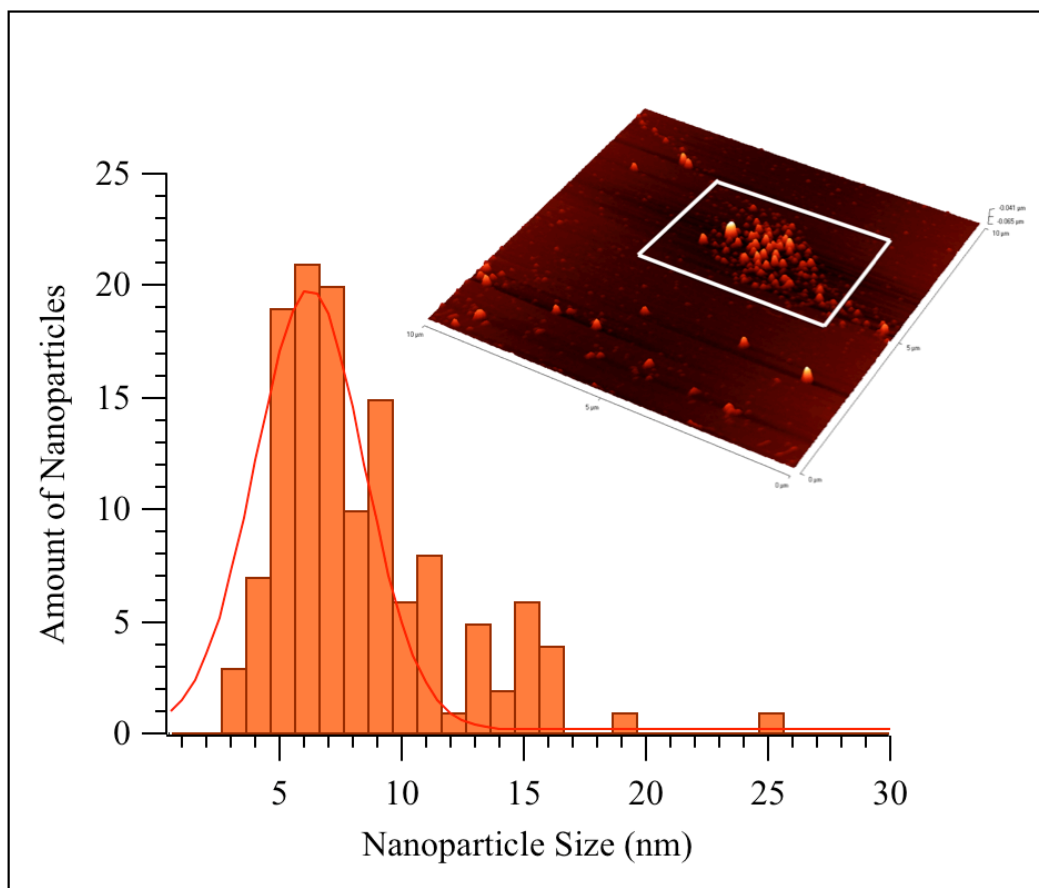


**Figure 47:** A histogram of the AFM image shown in Figure 45 b). The solid line shows the Gaussian distribution. The most frequently occurring average nanoparticle size (mode) is  $6 \pm 2$  nm. The average nanoparticle size is  $8 \pm 4$  nm.

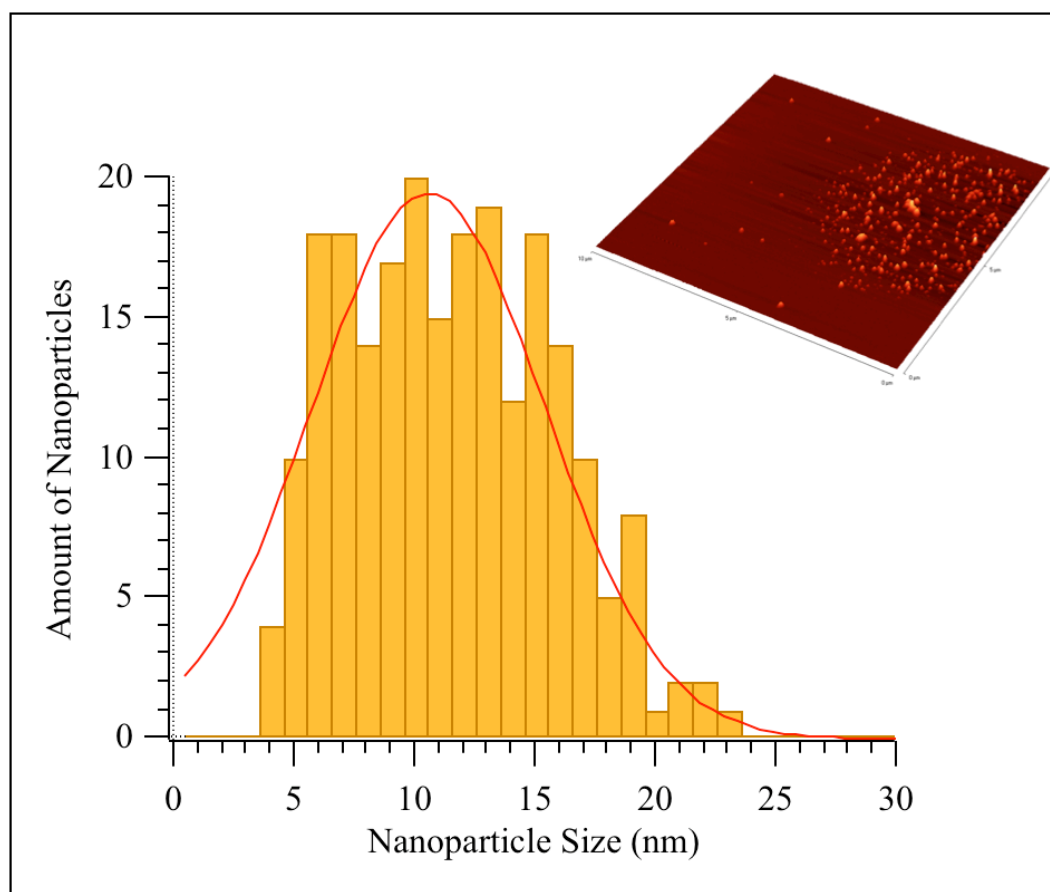


**Figure 48:** A histogram of the nanoparticles shown in Figure 45 c). The solid line is a fit done by using the Gaussian function. The most frequently occurring average nanoparticle size (mode) is  $11 \pm 3$  nm. The average nanoparticle size is  $11 \pm 4$  nm.

From the histograms above, it is evident that groups with different size distributions of nanoparticles are present on the same substrate. This is mostly because the wafers were spin casted. Spin casting encouraged a rough size segregation. The first two histograms (Figures 46 and 47) are skewed to the left and have two size distributions. For Figure 46, the second size distribution is around 14nm, and for Figure 47, around 15 nm. The presence of more than one

size distribution was not accounted for in the Gaussian function fit: only one fit was done for the entire distribution. In Figure 48, the histogram is only slightly skewed: the modal and mean values are roughly equal. From literature<sup>12</sup>, as discussed in the introduction, we expect to see an average particle size of about 6nm. Essentially, if the sample is fairly monodispersed, particles sizes of up to ~20nm are possible.

The next step then became varying the  $\gamma$ -Fe<sub>2</sub>O<sub>3</sub> nanoparticle concentration with a narrower scale. It is possible that lowering the spin coating speed to 1000rpm (Program Q), could lead to larger patches of nanoparticles leading to better assembly. Therefore, program Q was chosen for the next set of samples.

#### **4.6 Results from Slightly varying the concentration of $\gamma$ -Fe<sub>2</sub>O<sub>3</sub> nanoparticles redispersed in octane**

The concentration of nanoparticles in octane was varied on a more narrow scale, Figure 49: ranging from 0.29mg/ml to 1.43mg/ml of  $\gamma$ -Fe<sub>2</sub>O<sub>3</sub> nanoparticles applied, while suspended in solution, to the wafer.

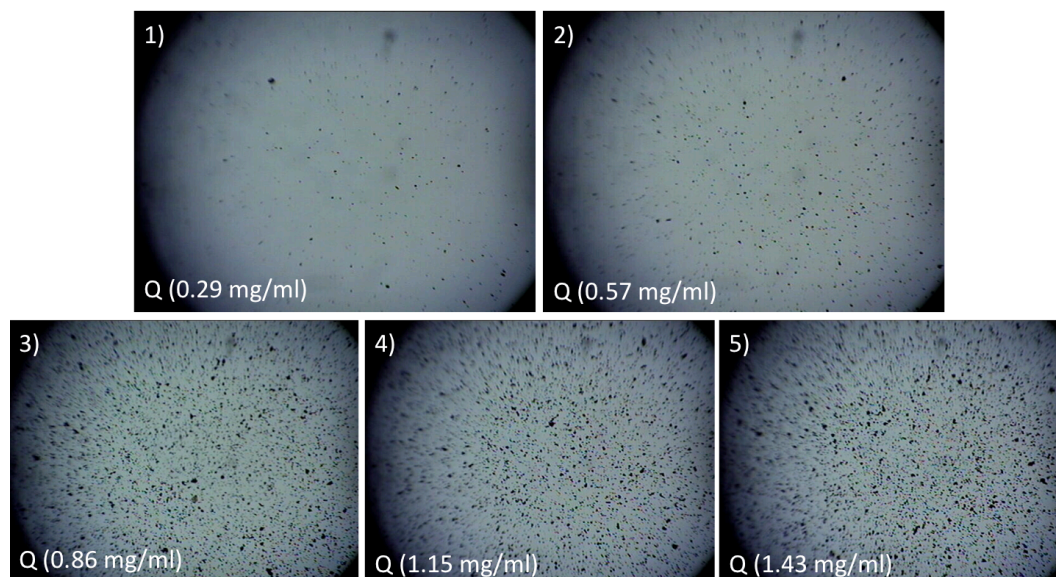


**Figure 49:** AFM video camera snap shots of  $\gamma\text{-Fe}_2\text{O}_3$  nanoparticles redispersed in octane at various concentrations as indicated. Program Q with 1000rpm was used to spin cast.

From the AFM video camera snapshots, it was evident that samples 3), 4), and 5) were too concentrated to be analyzed with AFM. Only samples 1) and 2) were scanned. Sample 1) gave more favorable results with fewer aggregates. Three AFM images from sample 1 are shown in Figure 50 below.

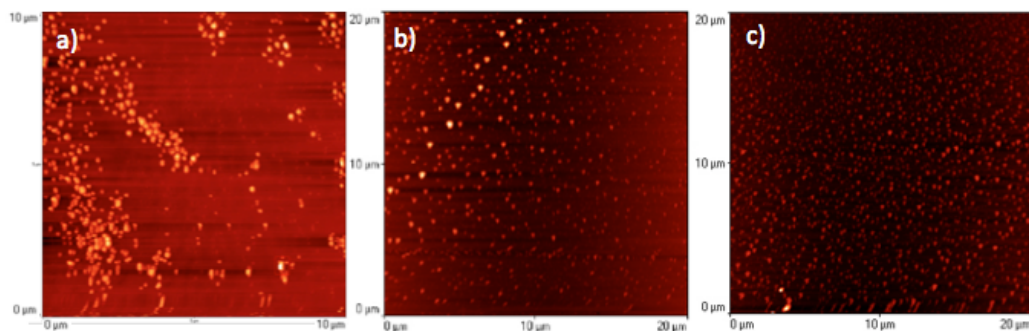


**Figure 50:** Images of sample 1, to which 0.15mg of nanoparticles were added, while suspended in solution, to the silicon wafer, which was spun at 1000rpm for 30 seconds. The AFM images are all  $20\mu\text{m}\times 20\mu\text{m}$  in size, for the exception of a) which is  $10\mu\text{m}\times 10\mu\text{m}$  in size.

In the figure above, patches (a), or 2-dimensional arrays (b) and (c), of nanoparticles are noticeable. In all the images above, there is evidence of multilayer formation. Particles are fairly close together and appear fairly monodispersed.

The following figures (51-53), are a series of histograms generated from the analysis of the images above.

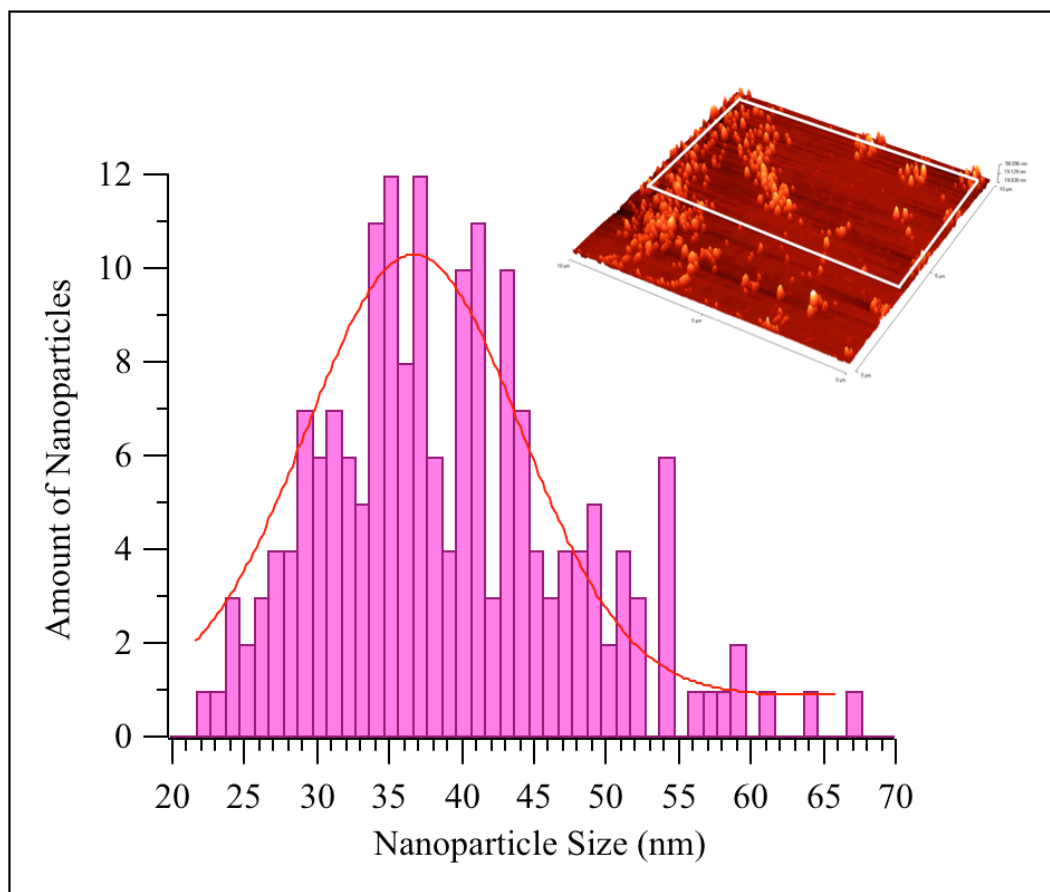


**Figure 51:** The histogram of the AFM image in Figure 29 a). The solid line shows the Gaussian distribution. The most frequently occurring average nanoparticle size (mode) is  $37 \pm 5$  nm. The average nanoparticle size is  $39 \pm 9$  nm. There is a large particle size distribution in this sample.

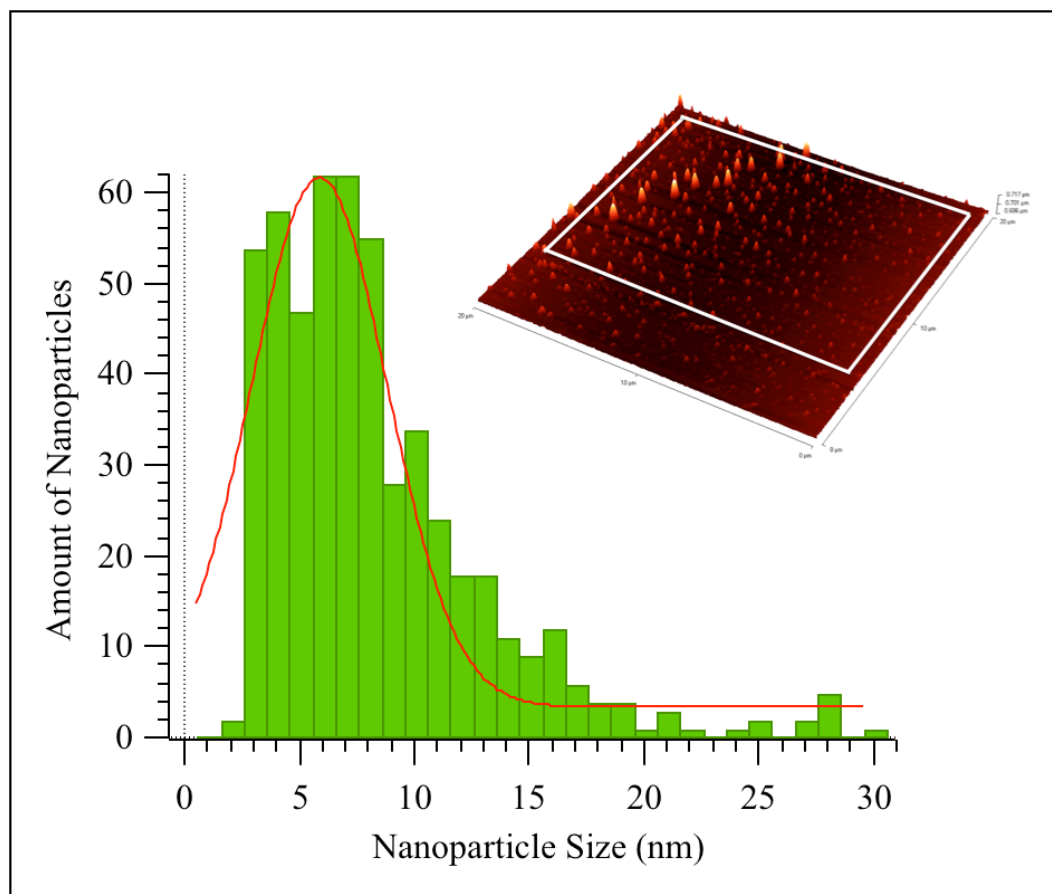


**Figure 52:** The histogram of the AFM image in Figure 29 b). The solid line shows the Gaussian distribution. The most frequently occurring average nanoparticle size (mode) is  $6 \pm 2$  nm, with a fairly narrow size distribution. The average nanoparticle size is  $8 \pm 5$  nm.

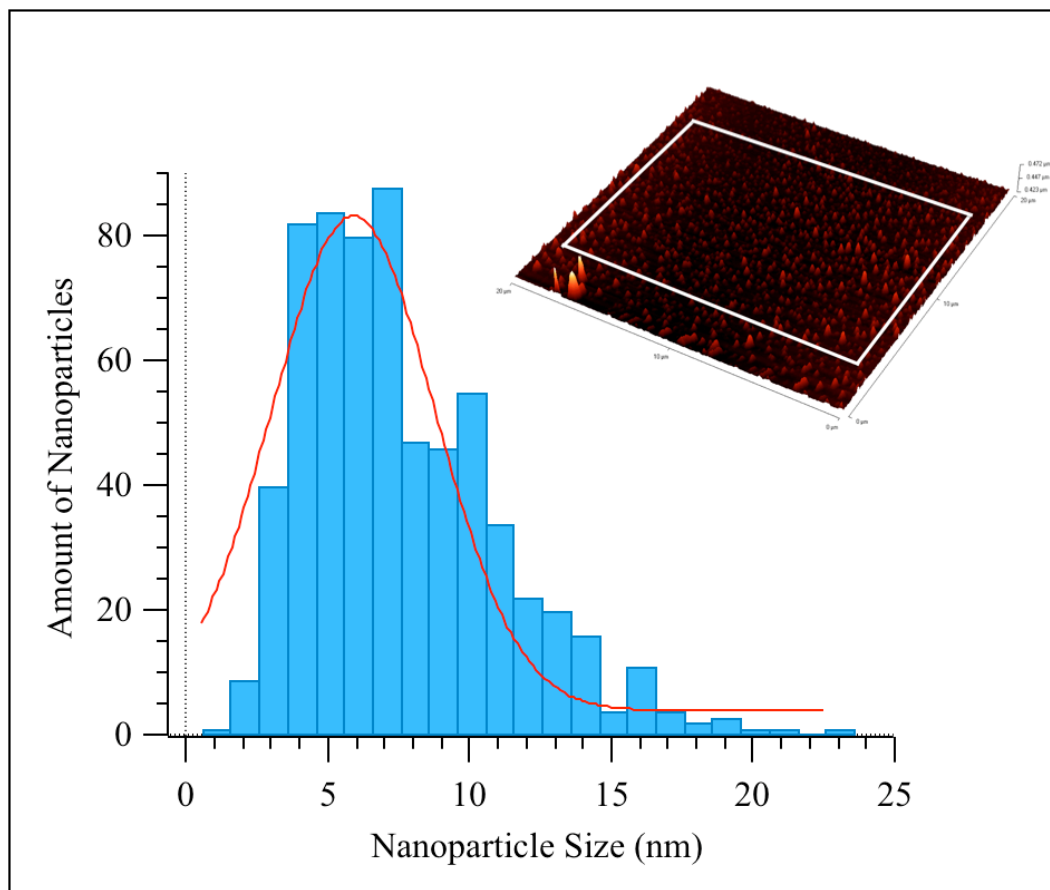


**Figure 53:** The histogram of the AFM image in Figure 29 c), It was fitted with a Gaussian curve. The most frequently occurring average nanoparticle size (mode) is  $6 \pm 2$  nm, with a narrow size distribution. The average nanoparticle size is  $7 \pm 4$  nm.

With evidence of the histograms above, it is clear that a lower speed of 1000rpm gave rise to a larger distribution of nanoparticle sizes (Figures 25-27). There appear to be multilayers of particles which could have increased the width of the histogram and caused the data to appear more polydispersed. However it is clear that the particles are fairly close together: close enough to measure the spacing between them with SEM. It is also observed that desired 2-dimensional

assembly can be obtained by using lower concentration of nanoparticles (0.29mg/ml) and lower spin casting speeds. The results prove that spin casting with the right speed can be used to push larger aggregates away, leaving fairly monodispersed nanoparticles at the center of the substrate.

#### 4.7 SEM Analysis

SEM was used to analyze the surface features of samples from the previous AFM analysis. High-resolution images of surface features captured the assembly of nanoparticles on the surface, as well as the spacing in between them. However one problem that hindered efficient data collection, was contamination. Due to the presence of the octanoic acid surfactants and possibly a minute amount of solvent residues of octane on the surface, carbon-based material quickly began to deposit on the surface. This caused blurry images and gave the appearance of lower resolutions. This also made it impossible to capture any 2-dimensional assemblies directly on the surface of the silicon wafer. (From the AFM sample, Figure 28.1, 2-dimensional assemblies on the surface of the silicon wafer was evident.) However, aggregates could be seen with detailed surface features. Within aggregates,  $\gamma\text{-Fe}_2\text{O}_3$  nanoparticles are densely packed. Hence the spacing measured between the nanoparticles in this state should closely correspond to

~2nm, the expected value from literature, calculations and Gaussian. The spacing was measured using two different methods, Figure 34.

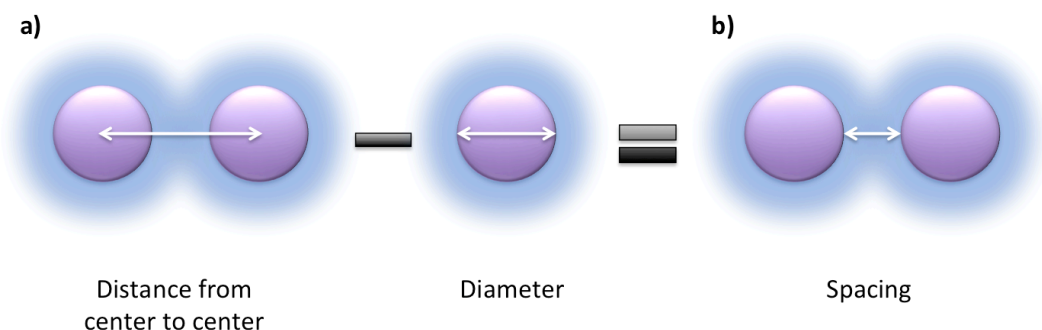


**Figure 54:**  $\gamma$ -Fe<sub>2</sub>O<sub>3</sub> nanoparticles, in purple, are surrounded by a ‘cloud’ of surfactants (octanoic acid), blue, that are anchored to the surface of the nanoparticle. The two different methods used to measure the spacing between two nanoparticles: a) by subtracting the measured diameter of individual nanoparticles from the measured distance between the center of one nanoparticle and the center of the other b) by directly measuring the spacing between the two nanoparticles. Ideally, both methods should give similar results.

Figures 55, 56 and 57 below show three images that best represent the surface of aggregates, in increasing resolution. The two methods described in Figure 34 were used to calculate the spacing between particles.

In Figure 55, the presence of nanoparticles can be seen at the surface. The surface appears cloudy because of the presence of octanoic acid surfactants: they influence the deposition of a carbon-based film. The carbon-based film results from the bombardment of the organics with the electron beam.<sup>31</sup>

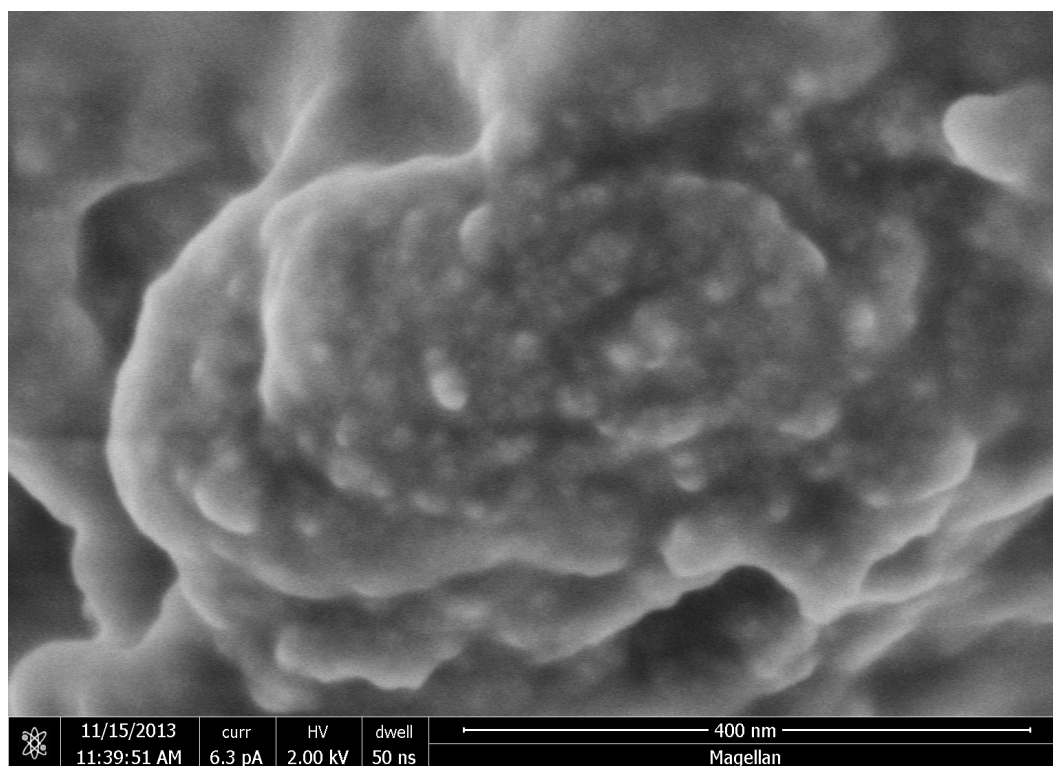


**Figure 55:** SEM image of a section of single aggregate of  $\gamma$ -Fe<sub>2</sub>O<sub>3</sub> nanoparticles.

In the figure, the edges of the nanoparticles are not sharp. The spacing was calculated using the two methods. For the first and more indirect, method, the average center-to-center distance measured was  $20 \pm 4$  nm, the average diameter measured was  $15 \pm 3$  nm. Hence the average spacing between particles, using the method, is  $4 \pm 5$  nm. As expected for a blurry image of a less monodispersed group of nanoparticles, the standard deviation is large. It is likely that an overestimation of the spacing was made. However, the average spacing measured was  $2.0 \pm 0.4$  nm. However the discrepancy between the two methods in this cases raises the question of precision and reliability. If the resolution of the image

is higher and the area of the sample has more monodispersed nanoparticles, then the spacing calculated and the error should decrease. This is noticed for Figure 56 below.

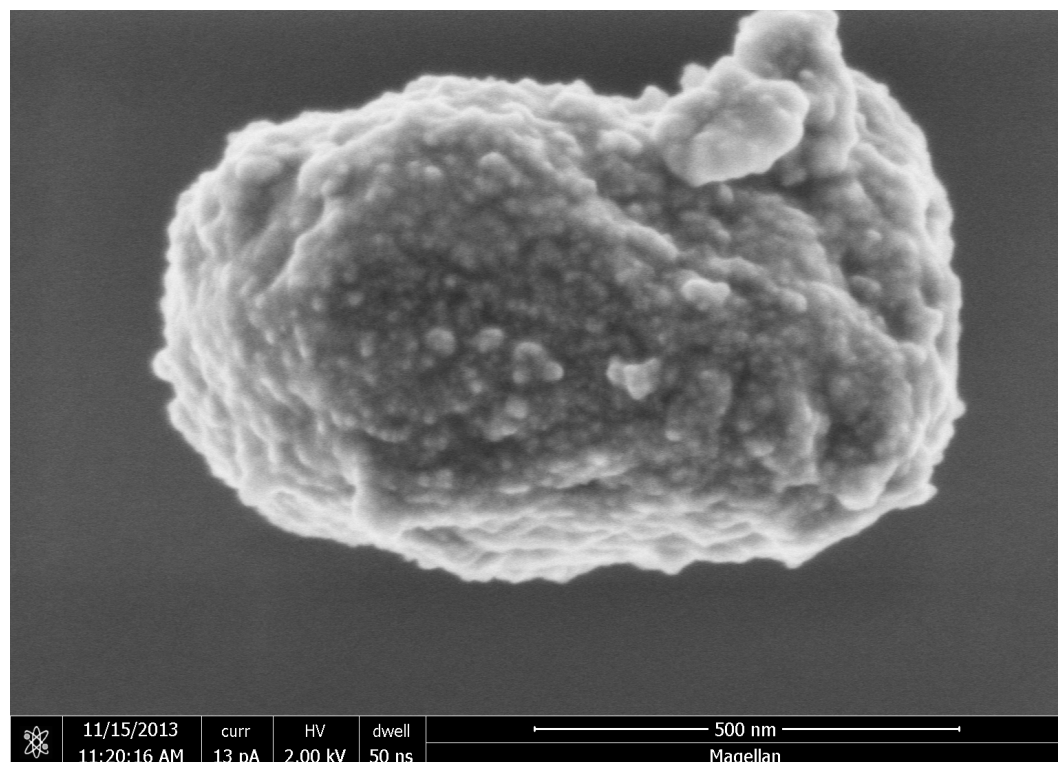


**Figure 56:** SEM image of a single aggregate of  $\gamma\text{-Fe}_2\text{O}_3$  nanoparticles.

In Figure 36, the resolution is higher and the particles appear more monodispersed. For the first and more indirect, method, the average center-to-center distance measured was  $16 \pm 3$  nm, the average diameter measured was  $13 \pm 3$  nm. Hence the average spacing between particles, using the method, is  $3 \pm 4$  nm. As expected for a sharper image of a more monodispersed group of nanoparticles,

the standard deviation is smaller, but still quite large. However, the average spacing measured was  $2.4 \pm 0.7$  nm. Even though the standard deviation is large for the previous value, the two values for the spacing are closer. However, if the resolution of the image is even higher and the area of the sample has even more monodispersed nanoparticles, then the spacing calculated and the error should decrease. This is noticed for Figure 57 below.

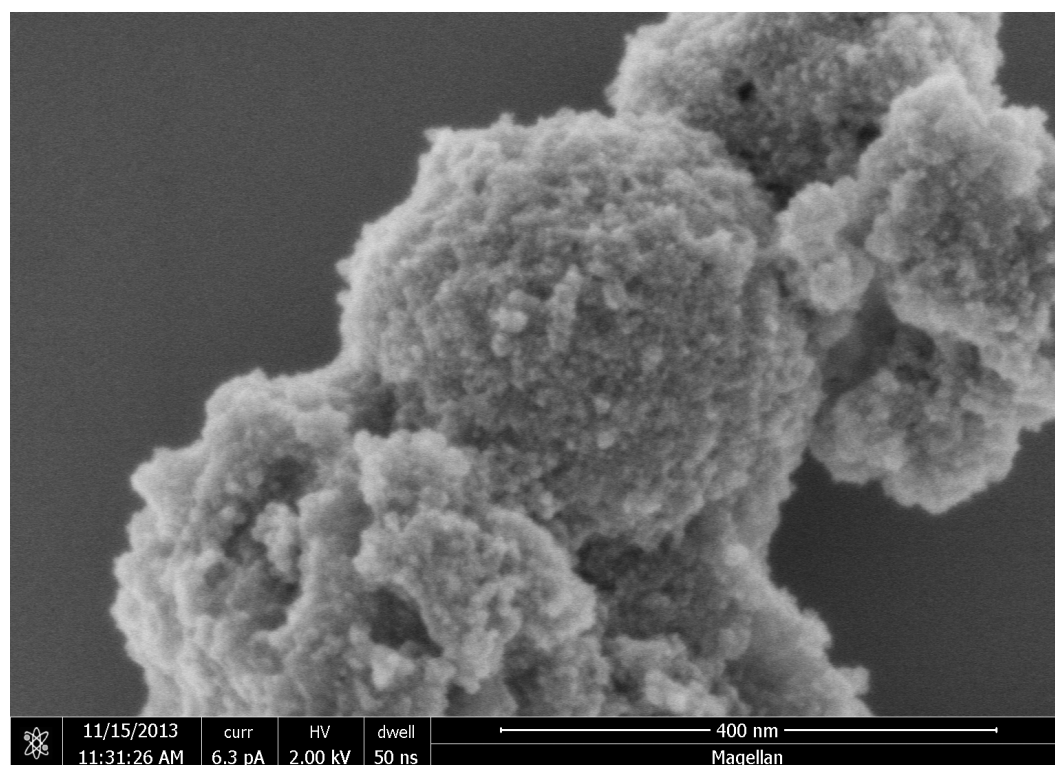


**Figure 57:** SEM image of an aggregate of  $\gamma$ -Fe<sub>2</sub>O<sub>3</sub> nanoparticles.

In Figure 57, the resolution is higher and the particles appear more monodispersed. For the first and more indirect, method, the average center-to-

center distance measured was  $8 \pm 2$  nm, the average diameter measured was  $6 \pm 1$  nm. Hence the average spacing between particles, using the method, is  $2 \pm 2$  nm. As expected for a sharper image of a more monodispersed group of nanoparticles, the standard deviation is smaller. The average spacing measured was  $2 \pm 0.4$  nm. The values for the highest resolution image had the smallest spacings and the smallest error of the three images analyzed. The spacing from literature for  $\gamma$ - $\text{Fe}_2\text{O}_3$  nanoparticles capped with octanoic acid was  $\sim 2$  nm and the average size of nanoparticles was 6 nm.<sup>12</sup>

From all the SEM images above, it is evident that a distance, the spacing, separates most, if not all of the nanoparticles even when they aggregate. This not only shows the evidence of successful capping during synthesis, but also how effective is it as keeping the nanoparticles separated and hence more magnetically stable. This becomes important for the data storage applications. The surfactants aid against agglomeration after assembly, and effectively each nanoparticle should be able to hold its own magnetization, without being affected by another.

## 5. CONCLUSIONS AND FUTURE WORK

Three characterization techniques, AFM, UV-Vis and FT-IR verified the successful synthesis of octanoic acid capped  $\gamma$ -Fe<sub>2</sub>O<sub>3</sub> nanoparticles. AFM further gave information on size distribution of  $\gamma$ -Fe<sub>2</sub>O<sub>3</sub> nanoparticles. The presence of Fe<sup>3+</sup> was confirmed using UV-Vis spectrophotometry, with a peak of  $\sim$ 330nm. The presence of octanoic acid was confirmed with FT-IR, with a peak of 1615cm<sup>-1</sup>, in the C=O region, and peaks 2853cm<sup>-1</sup>, 2920cm<sup>-1</sup> and 2957cm<sup>-1</sup>, in the CH vibrational region of the spectrum. Samples that contained the smallest (below 10nm) and most monodispersed distribution of  $\gamma$ -Fe<sub>2</sub>O<sub>3</sub> nanoparticles were presumably the most favorable. Sonication was used as an agitation method to redisperse aggregated nanoparticles, however most of the samples prepared in this way failed to give monodispersed assembly of particles. Vortex mixing proved to be the more efficient agitation method. It was effective at breaking up aggregates and any remaining solvent residues. This method is more convenient to use as it consumes less time to agitate. Per contra, vortex mixing produced more monodispersed nanoparticles from octane and toluene. As solvents, octane and toluene showed more favorable results than hexane. Both, not only re-dispersed particles well, which was indicated by smaller average sizes and less aggregates, but also produced more monodispersed nanoparticles, which was indicated by a small standard deviation relative to the samples made using hexane as the solvent. In terms of casting methods, spin casting proved to be more effective and more flexible than drop casting. Spin casting speeds of 1000rpm and 3000rpm were

effective, but the assembly was also largely dependent on the concentration of the samples. Concentrations of 6.25mg/ml (spun at 3000rpm) and 0.29mg/ml (spun at 1000rpm) produced the more monodispersed and better assembly of nanoparticles. Most representative average nanoparticle sizes for these samples, as expected, were  $7 \pm 4$  nm and  $8 \pm 5$  nm. SEM was used to measure the size of nanoparticles and the spacing, through Image J. Using the direct method, average spacing between two nanoparticles was found to be  $2.0 \pm 0.4$  nm.

The effects of spin casting and concentration on the assembly of  $\gamma\text{-Fe}_2\text{O}_3$  nanoparticles will be further investigated. Since spin casting was able to remove solvent droplets at faster speeds, further experimentation will be done with varying the concentration at speeds ranging from 3000 to 6100rpm. Measuring the spacing between particles with SEM gave expected values, but the error was fairly large. Therefore, rather than solely using AFM and SEM to image nanoparticles, Transmission Electron Microscopy (TEM) will also be used. TEM should be able to generate images with the best resolution of the three techniques: high resolution will lead to more accurate spacing measurements. Similar syntheses and analyses will be performed with butyric acid, lauric acid, oleic acid, and erucic acid surfactants as capping molecules: the spacing between the nanoparticles will also be measured experimentally to consider their feasibility at spacers.

### References Cited

1. (a) Drexler, K. E., *Engines of Creation: The Coming Era of Nanotechnology*. Doubleday: 1986; p 320; (b) Drexler, K. E. *Nanosystems: Molecular Machinery, Manufacturing, and Computation*. Massachusetts Institute of Technology, 1991.
2. Stone, V.; Johnston, H.; Clift, M. J., Air pollution, ultrafine and nanoparticle toxicology: cellular and molecular interactions. *IEEE transactions on nanobioscience* **2007**, 6 (4), 331-40.
3. (a) Zanker, H.; Schierz, A., Engineered nanoparticles and their identification among natural nanoparticles. *Annual review of analytical chemistry* **2012**, 5, 107-32; (b) Saini, R.; Saini, S.; Sharma, S., Nanotechnology: the future medicine. *Journal of cutaneous and aesthetic surgery* **2010**, 3 (1), 32-3.
4. Barnes, J., *The Presocratic Philosophers (Arguments of the Philosophers)*. Revised edition ed.; Routledge: 1983; p 728.
5. Binns, C., Size Matters. In *Introduction to Nanoscience and Nanotechnology*, John Wiley & Sons, Inc.: 2010; pp 11-32.
6. Lu, A. H.; Salabas, E. L.; Schuth, F., Magnetic nanoparticles: synthesis, protection, functionalization, and application. *Angewandte Chemie* **2007**, 46 (8), 1222-44.
7. Hyeon, T., Chemical synthesis of magnetic nanoparticles. *Chemical communications* **2003**, (8), 927-34.
8. Patnaik, P., *Dean's Analytical Chemistry Handbook*. 2nd edition ed.; McGraw-Hill Professional: 2004; p 1280.
9. Stanislaw Slomkowski, J. V. A., Robert G. Gilbert, Michael Hess, Kazuyuki Horie, Richard G. Jones, Przemyslaw Kubisa, Ingrid Meisel, Werner Mormann, Stanislaw Penczek, and Robert F. T. Stepto, Terminology of polymers and polymerization processes in dispersed systems (IUPAC Recommendations 2011). *Pure and Applied Chemistry* **2011**, 83 (12), 2229-59.

10. Wang, X.; Zhuang, J.; Peng, Q.; Li, Y., A general strategy for nanocrystal synthesis. *Nature* **2005**, *437* (7055), 121-4.
11. Kim, B. H.; Shin, K.; Kwon, S. G.; Jang, Y.; Lee, H. S.; Lee, H.; Jun, S. W.; Lee, J.; Han, S. Y.; Yim, Y. H.; Kim, D. H.; Hyeon, T., Sizing by weighing: characterizing sizes of ultrasmall-sized iron oxide nanocrystals using MALDI-TOF mass spectrometry. *Journal of the American Chemical Society* **2013**, *135* (7), 2407-10.
12. Yin, M.; Willis, A.; Redl, F.; Turro, N. J.; O'Brien, S. P., Influence of capping groups on the synthesis of  $\gamma$ -Fe<sub>2</sub>O<sub>3</sub> nanocrystals. *Journal of Materials Research* **2004**, *19* (4), 1208-15.
13. Hyeon, T.; Lee, S. S.; Park, J.; Chung, Y.; Na, H. B., Synthesis of highly crystalline and monodisperse maghemite nanocrystallites without a size-selection process. *Journal of the American Chemical Society* **2001**, *123* (51), 12798-801.
14. Nikhil R. Jana, Y. C., and Xiaogang Peng, Size- and Shape-Controlled Magnetic (Cr, Mn, Fe, Co, Ni) Oxide Nanocrystals via a Simple and General Approach. *Chemistry of Materials* **2004**, *16* (20), 3931-5.
15. Gaussian 98 (Revision A.7), M. J. F., G. W. Trucks, H. B. Schlegel, G. E. Scuseria, M. A. Robb, J. R. Cheeseman, V. G. Zakrzewski, J. A. Montgomery, R. E. Stratmann, J. C. Burant, S. Dapprich, J. M. Millam, A. D. Daniels, K. N. Kudin, M. C. Strain, O. Farkas, J. Tomasi, V. Barone, M. Cossi, R. Cammi, B. Mennucci, C. Pomelli, C. Adamo, S. Clifford, J. Ochterski, G. A. Petersson, P. Y. Ayala, Q. Cui, K. Morokuma, D. K. Malick, A. D. Rabuck, K. Raghavachari, J. B. Foresman, J. Cioslowski, J. V. Ortiz, B. B. Stefanov, G. Liu, A. Liashenko, P. Piskorz, I. Komaromi, R. Gomperts, R. L. Martin, D. J. Fox, T. Keith, M. A. Al-Laham, C. Y. Peng, A. Nanayakkara, C. Gonzalez, M. Challacombe, P. M. W. Gill, B. G. Johnson, W. Chen, M. W. Wong, J. L. Andres, M. Head-Gordon, E. S. Replogle and J. A. Pople, Gaussian, Inc., Pittsburgh PA, 1998.
16. Gogotsi, Y., *Nanotubes and nanofibers*. CRC Taylor & Francis: Boca Raton, FL, 2006.

17. Binns, C., The Nanotechnology Toolkit. In *Introduction to Nanoscience and Nanotechnology*, John Wiley & Sons, Inc.: 2010; pp 96-175.
18. Nanotechnology, L. C. f. Scanning Probes. <http://www.london-nano.com/research-and-facilities/themes/techniques/scanning-probes>.
19. Zhong, Q.; Inniss, D.; Kjoller, K.; Elings, V. B., Fractured polymer/silica fiber surface studied by tapping mode atomic force microscopy. *Surface Science Letters* **1993**, *290* (1-2), L688-L692.
20. Geisse, N. A., AFM and combined optical techniques. *Materials Today* **2009**, *12* (7-8), 40-45.
21. Joseph I. Goldstein, D. E. N., Patrick Echlin, David C. Joy, Charles Fiori, Eric Lifshin, *Scanning Electron Microscopy and X-Ray Microanalysis: A Text for Biologists, Materials Scientists, and Geologists*. 1st edition ed.; Springer: 1981; p 686.
22. Steff; ARTE Schema MEB (en).  
[http://en.wikipedia.org/wiki/File:Schema\\_MEB\\_\(en\).svg](http://en.wikipedia.org/wiki/File:Schema_MEB_(en).svg) (accessed November 21, 2013).
23. Douglas A. Skoog, F. J. H., Stanley R. Crouch, *Principles of Instrumental Analysis*. 6th edition ed.; Cengage Learning: 2007; p 1056.
24. Mehta, A. Ultraviolet-Visible (UV-Vis) Spectroscopy – Principle.  
<http://pharmaxchange.info/press/2011/12/ultraviolet-visible-uv-vis-spectroscopy-principle/>.
25. Sobarwiki Schematic of UV- visible spectrophotometer.  
[http://en.wikipedia.org/wiki/File:Schematic\\_of\\_UV-visible\\_spectrophotometer.png](http://en.wikipedia.org/wiki/File:Schematic_of_UV-visible_spectrophotometer.png).
26. Peter R. Griffiths, J. A. D. H., *Fourier Transform Infrared Spectrometry*. Second Edition ed.; Wiley-Interscience 2007; p 560.
27. Sanchonx FTIR Interferometer.  
[http://en.wikipedia.org/wiki/File:FTIR\\_Interferometer.png](http://en.wikipedia.org/wiki/File:FTIR_Interferometer.png).

28. Benitez, M. J.; Mishra, D.; Szary, P.; Badini Confalonieri, G. A.; Feyen, M.; Lu, A. H.; Agudo, L.; Eggeler, G.; Petravic, O.; Zabel, H., Structural and magnetic characterization of self-assembled iron oxide nanoparticle arrays. *Journal of physics. Condensed matter : an Institute of Physics journal* **2011**, *23* (12), 126003.
29. Socrates, G., *Infrared and Raman Characteristic Group Frequencies: Tables and Charts*. 3rd edition ed.; John Wiley & Sons: 2004; p 366.
30. Bordenyuk, A. N., C. Weeraman, A. Yatawara, H.D. Jayathilake, I. Stiopkin, Y. Liu, and A.V. Benderskii, Vibrational Sum Frequency Generation Spectroscopy of Dodecanethiol on Metal Nanoparticles. *Journal of Physical Chemistry* **2007**, *111* (25), 8925-33.
31. Charles Soong, P. W., and David Hoyle, Contamination Cleaning of TEM/SEM Samples with the ZONE Cleaner. *Microscopy Today* November 2012, 2012, pp 6-9.